Sensor Orientation Effects on
UXO Geophysical Target Discrimination

Project No. MM-1310

Shaw Environmental, Inc.

Sky Research, Inc.

Lead Principle Investigator: Dr. Jack Foley

December 2006

Final v. 1.0

Report Documentation Page	*Form Approved* *OMB No. 0704-0188*

Public reporting burden for the collection of information is estimated to average 1 hour per response, including the time for reviewing instructions, searching existing data sources, gathering and maintaining the data needed, and completing and reviewing the collection of information. Send comments regarding this burden estimate or any other aspect of this collection of information, including suggestions for reducing this burden, to Washington Headquarters Services, Directorate for Information Operations and Reports, 1215 Jefferson Davis Highway, Suite 1204, Arlington VA 22202-4302. Respondents should be aware that notwithstanding any other provision of law, no person shall be subject to a penalty for failing to comply with a collection of information if it does not display a currently valid OMB control number.

1. REPORT DATE **25 DEC 2006**	2. REPORT TYPE **Final**	3. DATES COVERED **-**

4. TITLE AND SUBTITLE **Sensor Orientation Effects on UXO Geophysical Target Discrimination**	5a. CONTRACT NUMBER
	5b. GRANT NUMBER
	5c. PROGRAM ELEMENT NUMBER
6. AUTHOR(S) **Foley, Jack**	5d. PROJECT NUMBER **MM-1310**
	5e. TASK NUMBER
	5f. WORK UNIT NUMBER

7. PERFORMING ORGANIZATION NAME(S) AND ADDRESS(ES) **Shaw Environmental, Inc. Sky Research, Inc. 445 Dead Indian Memorial Rd. Ashland, OR 97520**	8. PERFORMING ORGANIZATION REPORT NUMBER

9. SPONSORING/MONITORING AGENCY NAME(S) AND ADDRESS(ES) **Strategic Environmental Research and Development Program 901 North Stuart Street, Suite 303 Arlington, VA 22203**	10. SPONSOR/MONITOR'S ACRONYM(S) **SERDP**
	11. SPONSOR/MONITOR'S REPORT NUMBER(S)

12. DISTRIBUTION/AVAILABILITY STATEMENT
Approved for public release, distribution unlimited

13. SUPPLEMENTARY NOTES
The original document contains color images.

14. ABSTRACT

15. SUBJECT TERMS

16. SECURITY CLASSIFICATION OF:			17. LIMITATION OF ABSTRACT	18. NUMBER OF PAGES	19a. NAME OF RESPONSIBLE PERSON
a. REPORT **unclassified**	b. ABSTRACT **unclassified**	c. THIS PAGE **unclassified**	**UU**	**104**	

TABLE OF CONTENTS

LIST OF FIGURES

LIST OF TABLES

ACRONYMS

AHRS	Attitude-Heading Reference System
BRAC	Base Realignment and Closure
DAS	Data Acquisition System
DGPS	Differential Global Positioning System
DoD	Department of Defense
EM	Electromagnetic
EMI	Electromagnetic Induction
ESTCP	Environmental Security Technology Certification Program
FLBGR	Former Lowry Bombing and Gunnery Range
FUDS	Formerly Used Defense Sites
GDC	Geophysical Data Center
GPO	Geophysical Prove-Out
GPS	Global Positioning System
GUI	Graphical User Interface
HIP	Handheld Interface Pod
Hz	Hertz
IMU	Inertial Measurement Unit
JDR	Jeep Demo Range
JPG	Jefferson Proving Ground
LSBP	Lake Success Business Park
MEMS	Micro Electro-Mechanical Sensors
MTADS	Multi-Sensor Towed Array Detection System
MTBF	Mean-time-between-failure
NRL	Naval Research Laboratory
PIG	K941 shipping container
RDTSC	Read Time-Stamp Counter
RMS	Root Mean Square
RTK GPS	Real-time Kinematic Global Positioning System
RTS	Robotic Total Station
SERDP	Strategic Environmental Research and Development Program
TEM	Time Domain EM
USACE	US Army Corps of Engineers
UXO	Unexploded Ordnance
YPG	Yuma Proving Ground

Acknowledgements

Executive Summary

Use of electromagnetic (EM) methods to discriminate frag and geology from unexploded ordnance (UXO) has shown steady improvement over time as demonstrated by test site results. Performance of off-the-shelf and customized EM sensors have increased both in terms of UXO probability of detection and false alarm rate. Parallel with the increase in capabilities of UXO detection and discrimination is the increasing use of digital geophysical techniques on live sites. However, a significant gap exists in capabilities for UXO detection and discrimination between prove-out / test sites and actual UXO contaminated sites. In addition, the future deployment of more sophisticated sensors with discrimination capabilities is limited by the requirement for greater data fidelity for wide application on most sites.

One issue of importance for improving data quality is the need for improved spatial representation of the geophysical signature of subsurface UXO. Presently, survey data are inadequately spatially quantified with simple XY sensor locations and an assumed constant Z elevation. To accurately represent the geophysical signature of subsurface UXO, more complete and accurate information is required, including sensor elevation information, orientation data (yaw, pitch and roll), and sensor velocity and acceleration data. Therefore, Strategic Environmental Research and Development Program (SERDP) Project UX-1310 "Sensor Orientation Effects on UXO Geophysical Target Discrimination" was designed to research how the response of geophysical sensors is affected by variations in sensor orientation and motion, to develop an approach to measure these effects in the field, and to develop modeling and analysis techniques to mitigate the effects of sensor orientation and motion.

The research design for this project addressed data fidelity issues with respect to positioning in increasingly complex testing sites to define, develop and refine new data collection, processing and analysis capabilities to meet the needs encountered in typical survey environments. In addressing these needs, this project has met the following objectives: definition of the effects of dynamic motion on target signature data; definition of the range of sensor orientations that produce data sufficient for application of existing target characterization and discrimination modeling techniques; investigation of an auxiliary sensor package required to measure sensor dynamics during data recording; development of a mechanical solution to mitigate the sensor orientation problems; and development of modified data modeling techniques that remove the effects of dynamic data collection.

The technical approach to achieve these objectives included the following: quantification of sensor orientation effects; investigation of the use of inertial measurement units (IMUs); development of a gimbaled sensor configuration incorporating advanced positioning and data acquisition system (DAS) technologies; tests of this system in a variety of controlled and live site scenarios; and modeling of the sensor orientation effects to determine the impact of improved positioning on the ability to make target parameter estimates.

Tests conducted to evaluate the effects of sensor orientation showed that variation in EMI sensor orientation causes significant changes in EMI signatures. For example, a cylinder target at a depth of 0.5 m depth showed a 7-8% reduction in peak amplitude per cm due to sensor – target offset. When orientation is separated from offset, the peak amplitude changed between 0.5% and 2% per degree. Roll angles were found to be more significant then pitch, which were in turn more significant than yaw. Changes in EMI signatures, if unmeasured and not incorporated into the inverse modeling, make EMI data inadequate for UXO modeling in realistic conditions.

This project demonstrated that yaw, pitch and roll data can be effectively collected using IMUs to accurately measure sensor orientation during EMI data collection. Advances in Micro Electro-Mechanical Sensors (MEMS) technology have resulted in low-cost ($5-10K), commercially available IMUs; this project utilized the Crossbow Solid State IMU known as an Attitude-Heading Reference System (AHRS). The AHRS uses a 3-axis accelerometer and a 3-axis rate sensor to make a complete measurement of the dynamics of the sensor system. One issue with commercial IMU instruments is that they can be corrupted by the primary magnetic field of the EM sensor and can also influence sensor measurements. Therefore, this project developed a proto-type low metal IMU using commercially available integrated accelerometer circuits comprised of an integrated circuit board containing the Analog Device ADXL311 accelerometer and housed in a plastic case with no substantial metallic components. Testing of the proto-type IMU demonstrated that while the IMU worked well under most bench-top conditions, it failed to provide reliable measurements during survey tests. Subsequent additional improvements of the proto-type IMU device failed to reduce noise levels and increase reliability. Therefore, further development of a low metal IMU was not pursued by this project and subsequent data collection was conducted using the Crossbow IMU.

The development of a gimbaled sensor configuration provided a mechanical solution to allow the sensor to rotate in the pitch and roll axis. The platform is a lightweight, non-metallic pushcart consisting of a wheel/axle, frame, a yoke, and EM61 sensor assembly. All the components were constructed from non-conductive materials to eliminate EM signature effects. The EM61 remains aligned with the gravity vector regardless of the orientation of the mounting frame and deployment platform. The frame allows for the mounting of GPS electronics and EM electronics on the handlebars. The unit was designed for shipping and fits into a standard bicycle plastic shipping container. After the construction of the gimbaled cart system, a number of controlled and "real-world" tests were performed from 2004 to 2006 to measure the effectiveness of the design. These tests varied from controlled conditions to less controlled conditions, deployment to a live site, and a test site.

Controlled tests were conducted in 2004 and included tests conducted on a level parking lot, relatively flat test plot and an inclined and rutted test plot. A visual comparison of the gimbal-augmented cart data showed small increases in the data quality and decrease in noise over the stiff cart data (Foley, 2004). The

reduction in noise increased some anomaly amplitudes and reduced amplitudes in others. In addition, positional error associated with orientation were found to be significantly reduced using the gimbaled cart system. During the Ashland parking lot tests, 15 and 28 percent of the data had positional errors greater than 4 cm for the pitch and roll orientations, respectively. When using the gimbaled cart, the errors reduced to < 1 and 2 percent for roll and pitch, respectively. At the Former Lowry Bombing and Gunnery Range (FLBGR), testing of the gimbal cart system in a rutted geophysical prove-out test plot showed that the data collected by the gimbaled cart had a higher signal-to-noise ratio and improvements in the spatial accuracy.

In 2004, the system was also tested at DuPont's Lake Success Business Park (LSBP) in Connecticut as part of the Environmental Security Technology Certification Program (ESTCP) live-site demonstration project. Comparison of a standard survey configuration and the gimbaled cart configuration showed that the gimbaled cart position data surpassed the quality from the standard surveys. With a shorter prism pole and the gimbal arms countering the bumps and ruts, position data had fewer zigs and zags, thus mitigating positional errors and improving geophysical data quality (Foley, 2004). At LSBP, 40 percent of the data had roll-induced positional errors of greater than 10 cm, and nearly 10 percent of that data had errors over 20 cm when the stiff cart was used. When using the gimbaled cart, only 4 percent of the data had positional errors that exceeded 5 cm.

In 2005, additional complexity was added to the testing of the gimbaled cart system. At the Ashland Test Plot site in Ashland, Oregon, the ground surface was modified with ruts, small ramps and stick mats to mimic field conditions found on typical live sites to introduce additional positional errors to the EM data. The objective of subsequent field tests was to quantify the ability of gimbaled cart system to mitigate the effects of these features. Modification of the test plot was comprised of creation of ruts 15 cm deep and 30 to 45 cm long adjacent to targets in the test plot. To simulate the conditions at wooded sites where deadfall typically litters the ground, 9 ramps were placed adjacent to 9 emplaced subsurface targets. Ramps were constructed 10 to 15 cm in height and 30 to 45 cm in length. Last, a set of stick mats were used to simulate high frequency micro-topographic variations. These tests demonstrated how improvements in sensor positioning and orientation improve the fidelity of target parameters (the βs) estimated by inverting EM61 data collected in field surveys.

Final testing of the system was conducted in 2006 at the Blossom Point Test Site in Maryland and conducted to further test and evaluate improvements in the data collection platform developed by this project and sensor positioning information and analysis methods. Data at the Blossom Point test site were collected by using the gimbaled EM61 cart and two different positioning systems, a GPS system and an ArcSecond laser positioning system in several configurations with gimbals both fixed and free. The data generally showed that the residual geolocation error appears to be smaller and the dipole fit quality generally better when the gimbals are free and also when using the ArcSecond positioning rather than with GPS positioning. However, target depth estimates for the survey data sets were not very accurate. Although on average estimated depths were within a few centimeters of actual target depths, the scatter in the estimated depths (RMS depth error) amounted to about 1/3 of the average target/coil separation. The scatter was slightly less for the ArcSecond fits (21.7 cm) than for the GPS fits (27.7 cm). Even for relatively high quality fits, the depth estimates were not very accurate, and we suspect that the data density may not have been adequate to support reliable inversion for many of the targets. Given the

lackluster performance for target depth estimates, target size estimates were surprisingly robust. On average, the size metric $(\Sigma\beta)^{1/3}$ was found to vary in direct proportion with the size of UXO and UXO-like targets. The scatter in the estimates amounted to about 25% of the mean values. As with depth estimates, substantial differences in the accuracy of the size estimates for the various survey modes were not observed. Target shape classification based on the dipole fits using standard processing was a failure. No clear clustering of different target types in different regions of β_1/β_2 *vs.* β_2/β_3 space for any of the surveys with standard processing were found. However, the results for dynamic model inversions were encouraging, resulting in reasonable shape estimates for those targets where SNR and data density do not appear to be limiting performance. The analysis suggests that a higher data density (closer survey line spacing) than that used here would be required to secure significant performance improvements.

Sensor orientation information was utilized during the forward and inverse modeling process to account for signature variations caused by non-horizontal sensor orientation during data collection. As part of this project, the EM modeling process for sensor orientation information was developed that included full simulation of 3D orientation of EMI sensors; multi-time gate EMI response; and a beta classification technique. An EMI dipole response model was tested to facilitate modeling of EM data in conjunction with concurrently collection orientation information and incorporated into the beta inversion model used for target parameter estimation.

1.   INTRODUCTION

1.1.   Background

Use of electromagnetic (EM) methods to discriminate frag and geology from unexploded ordnance (UXO) has shown steady improvement over time as demonstrated by test site results. Performance of off-the-shelf and customized EM sensors have increased both in terms of UXO probability of detection and false alarm rate. Parallel with the increase in capabilities of UXO detection and discrimination, government contractors have increased the use of digital geophysical techniques on live sites. Unfortunately, the capabilities demonstrated at test sites have not been readily achieved under typical field conditions. In fact, even under relatively hospitable field conditions (e.g. Southwest PG, AR; Rocky Mountain Arsenal, CO; and Fort Ord, CA), data quality was found to be insufficient for implementation of modern analytical methods (Asch & Staes, 2001, Barrow & Nelson, 2001, and Mason et al., 2001). Thus, a significant gap in capabilities for UXO detection and discrimination exists between prove-out/ test sites and actual UXO contaminated sites. In addition, future deployment of more sophisticated sensors (e.g., EM63, Geophex GEM-3) offering significant potential to increase UXO discrimination capabilities but is limited by the requirement for greater data fidelity for wide application of these advanced EM techniques on most sites.

One issue of importance for improving data quality is the need for improved spatial representation of the geophysical signature of subsurface UXO. Controlled tests of EM data via Multi-sensor Towed Array Detection System (MTADS), analyzed, and published by AETC (Barrow & Nelson, 2001) have documented degradation of UXO discrimination results due to motion-induced signature complexities. Presently, survey data are inadequately spatially quantified with simple XY sensor locations and an assumed constant Z elevation. To accurately represent the geophysical signature of subsurface UXO, more complete and accurate information is required, including sensor elevation information, orientation data (yaw, pitch, and roll), and sensor velocity and acceleration data. Strategic Environmental Research and Development Program (SERDP) Project UX-1310 "Sensor Orientation Effects on UXO Geophysical Target Discrimination" was designed to research how the response of geophysical sensors to targets such as UXO is affected by variations in orientation and motion of the sensors and to develop an approach to measure and model sensor orientation and motion.

Augmentation of EM data with sensor orientation measurements is required to compensate for both orientation effects and varying levels of magnetic flux that pass through EM sensor coils and alter target signatures. With augmentation of EM data with orientation information and modification of

discrimination methods for dynamic sensor recording conditions, the important benefits of UXO discrimination may be realized by the Department of Defense (DoD).

1.2. Research Objectives

The goal of this project was to develop the required technologies for broad application of existing, emerging, and future UXO discrimination methods in typical field environments. Presently, because of sensor orientation effects, advanced UXO discrimination methods are limited to test areas and "prove-out" sites with unrealistic field conditions.
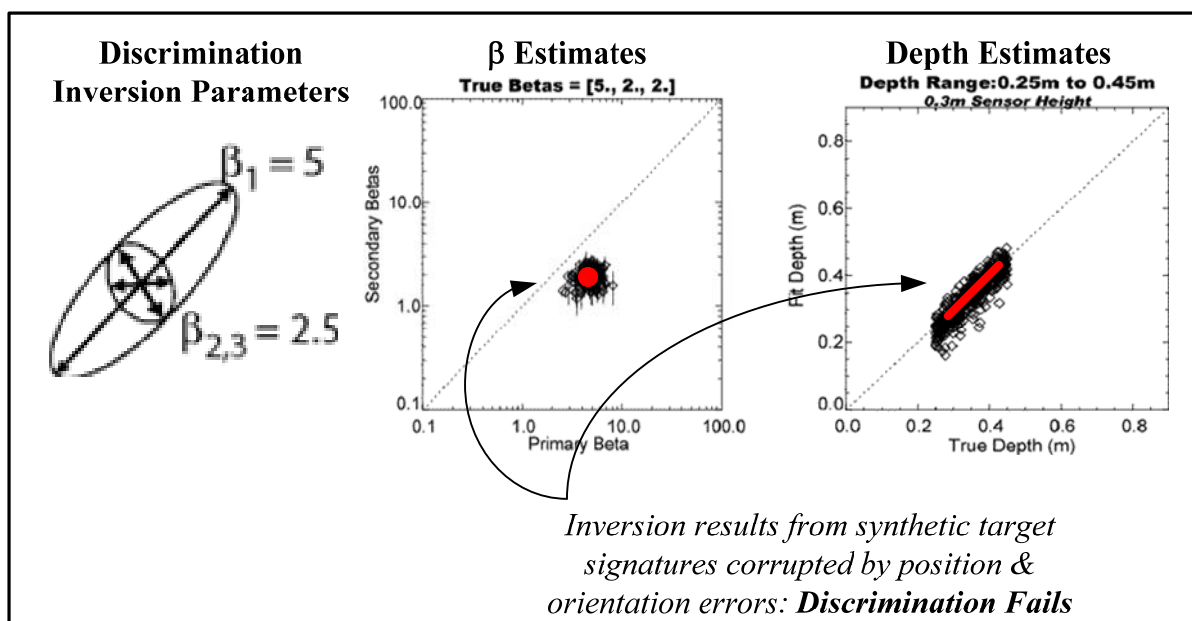
Figure 1. Sensor positioning accuracy controls data fidelity and UXO detection/discrimination capabilities.

For several years, most geophysicists experienced with UXO target detection and characterization have known that data collected on prove-out test plots have significantly higher levels of signature fidelity than data collected from the rest of a UXO site. Consequently, it is also commonly known that sophisticated data analysis techniques useful on prove-out sites are mainly inappropriate for UXO production work due to complexities seen in the field data. Therefore, this project addressed the following four questions:

- What are the capabilities of EM inverse modeling techniques for detection, location, and discrimination of UXO in unconstrained physical environments?

- What phenomenological effects influence the collection of EM data from EM61 induction sensors and more sophisticated EM instruments?

- What additional processing and analysis elements are needed for data reduction and modeling techniques to robustly and accurately discriminate UXO from non-UXO targets under unconstrained physical environments?

- What auxiliary sensors should be used to collect sufficient data to quantify the physical state of the sensors under unconstrained physical environments?

DoD has a clear need for data analysis methods to reduce unnecessary excavations at UXO sites (often quoted as accounting for 70% of the expense of UXO operations) that can be developed quickly for deployment on Formerly Used Defense Sites (FUDS) and Base Realignment and Closure (BRAC) sites with UXO clearance requirements. While progress towards this objective is evident from successive Jefferson Proving Ground (JPG) tests, the ultimate progression of this technology and routine application on live sites has been slow in coming due to complications associated with data collected off the prove-out test plots under moderate and difficult field conditions. This research and development program addresses the need to examine the complication and degradation of data fidelity as more difficult conditions are encountered, and to refine and/or develop new data processing and analysis capabilities to meet the needs of typical survey environments.

To achieve the goal of providing UXO discrimination technologies beyond the prove-out test plot for routine use on actual survey grids, the following subordinate objectives have been defined:

- Define the range of sensor orientations that produce data sufficient for application of existing target characterization and discrimination modeling techniques.

- Define the effects of dynamic motion on target signature data and relate these effects to field conditions.

- Define an auxiliary sensor package required to measure sensor dynamics during data recording.

- Develop mechanical solutions that mitigate the sensor orientation problem by allowing EM sensors to be deployed in rough terrain without misorientation of the sensors.

- Develop modifications to existing data modeling techniques that remove the effects of dynamic data collection.

1.3. Technical Approach

The technical approach to meeting our research objectives can be summarized as follows:

1. *Quantify the effects of sensor orientation.*

   To do this, we systematically collected data in a 4-step process:

   Laboratory Test Data. Under this step a series of controlled tests were executed to evaluate the data acquisition system (DAS), placement of the gyro electronics relative to the EM coil, and evaluate the maneuverability/ ergonomics of a modified EM61 pushcart.

   Platform Data. Data were collected from a platform constructed of non-metal material to make precision measurements of standard UXO items under controlled conditions. This process allowed quantification of the specific effect of various components of sensor orientation.

   Pseudo Survey Data. EM data integrated with the gyro and laser navigation positioning system were gathered in a series of controlled surveys over test items to define the operating performance of the integrated system.

   Test Plot Data. EM data integrated with the gyro and laser navigation positioning system were collected from test plots seeded with several different types of UXO and non-UXO items. These data were collected to allow systematic review of the effects of sensor orientation under simple field conditions.

2. *Develop a low metal inertial measurement unit (IMU) instrument that can measure the orientation of the sensors as they are deployed.*

   Mitigation of all sensor orientation variability may be not be readily achievable using commercial off the shelf IMUs, as they can be corrupted by the EM coils transmission of a primacy magnetic field and are made of metal and therefore influence the EM sensor measurement. Therefore, one of the objectives of this project was to develop and test a prototype low metal IMU sensor for measurement of pitch, roll, and 3-axis acceleration.

3. *Mitigate and measure sensor orientation effects during deployment through the development of a gimbaled sensor configuration incorporating IMU, advanced positioning technology and DAS improvements.*

   This mechanical solution allows the EM coils to "float" over potholes and topographical anomalies that normally tilt the sensors to remove sensor variability during deployment.

Incorporated into the gimbal sensor configuration is improved positioning technology achieved by integrating more sophisticated robotic total station (RTS) technology for more precise positioning and by establishing more rigorous time stamping of RTS positional solutions and EM sensor data through data acquisition improvements.

4. *Conduct testing of the mechanical system, IMU, RTS positioning technology, and the improved DAS.*

   Testing was conducted in both controlled and live site surveys to develop a clear understanding of the potential and limitations of these technologies.

5. *Analyze and model sensor orientation effects as they impact the ability to make estimates of target parameters.*

   As the level of sophistication of EM sensors and associated discrimination methods increases, requirements for data fidelity will also increase. This project worked to understand and document the complexities of EM data and associated modeling techniques in heterogeneous conditions to successfully migrate discrimination capabilities from prove-out plots to actual contaminated sites.

We concentrated our research and development efforts on the EM61-MKII sensor. This sensor was chosen as the focus of our efforts because significant data and working knowledge exists for this device; in addition, it is the primary sensor presently used for digital geographic mapping at UXO sites. Lessons learned from the EM61 can be readily transferred to other sensors. We also concentrated our mechanical solution efforts on a man-portable pushcart device. Because the focus of the project was to understand and address sensor orientation problems in general, the lessons learned using the pushcart can be applied to vehicle-towed and hand held systems.

2. EFFECTS OF SENSOR ORIENTATIONS

To measure the effects of sensor orientations, we first reviewed existing data collected by the Naval Research Laboratory (NRL) GEMTADS demonstrations. These data were used in the assessment of the effects of beta-fit parameters. Data were then collected in a laboratory setting to measure the affects of an IMU and the EM61-MKII. Using the IMU and the EM61, we then collected data at a platform constructed at the Former Lowry Bombing and Gunnery Range (FLBGR) in Colorado, measured the actual platform position and orientation data, and used it to simulate the effects on the inversion of targets. Last, a series of tests were conducted under controlled conditions, referred to as "pseudo-surveys," to capture the motion of the sensor and define the effects of orientation under idealized conditions.

2.1. Review of Previous Data

The NRL collected data relevant to this project in the fall of 2003 when the MTADS vehicle was deployed to the Standardized UXO Technology Demonstration Sites at Aberdeen Test Center and Yuma Proving Ground (YPG) Test Centers as part of the NRL GEMTADS Demonstrations. All sensors (EMI, global positioning system [GPS], and motion) were mounted on a rigid 2 meter (m) x 2 m board in order to moderate trailer vibrations and flexing (Figure 2).
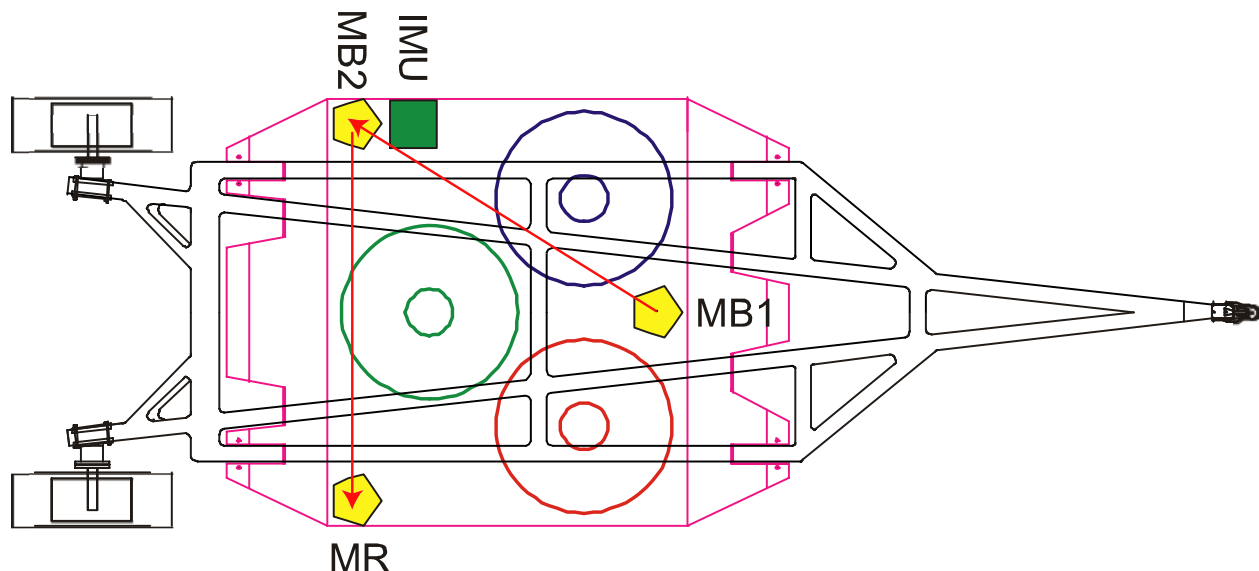
Figure 2.   Initial MTADS GEM array with full motion sensors. Three antenna GPS measures x, y, z position, heading, pitch and roll of platform. IMU measures angular rates to derive integrated roll and pitch angles.

Figure 3 shows an example of data from YPG; the graphs are z (vertical), pitch and roll motions as a function of along-track distance in meters. Again, the black lines were derived from the GPS data and the red lines from the IMU. These data were collected on two tracks (traversed back and forth) in a region of moderate slopes (as shown in the z graph) and moderate bumps. There is a significant amount of pitch and roll of the trailer.
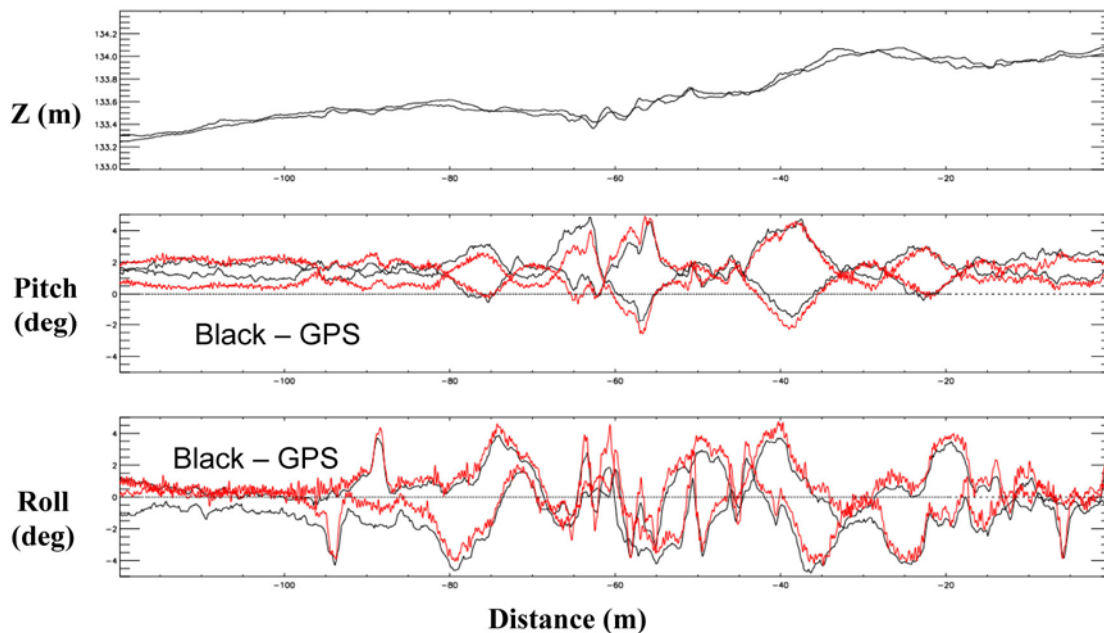
Figure 3.   Platform motion measured by MTADS GEM array at YPG Test Site. Two passes across field.

Figure 4 shows the power spectral densities of the time traces of the previous figure. The top graph shows the spectra (in units of g2/Hz, in the body frame of the trailer) of the vertical (black), along-track (red) and cross-track (green) accelerations. The lower graph shows the spectra (in units of deg2/Hz) of the roll (black) and pitch (red) angles of the trailer. It is believed that the motions shown here are mostly flex of the trailer A-frame and vibration (mostly up and down motion of the 2m x 2m board), which are on the order of centimeters.

Review of all the NRL data show that orientation changes are both short- and long-wavelength. Short duration effects are from trailer response to obstacles, such as ruts. Longer duration effects are due to changes in the slope of the ground being traversed. In conclusion, we found that a 10 degree change in orientation causes a 20% change in the primary field at 1 m distance.
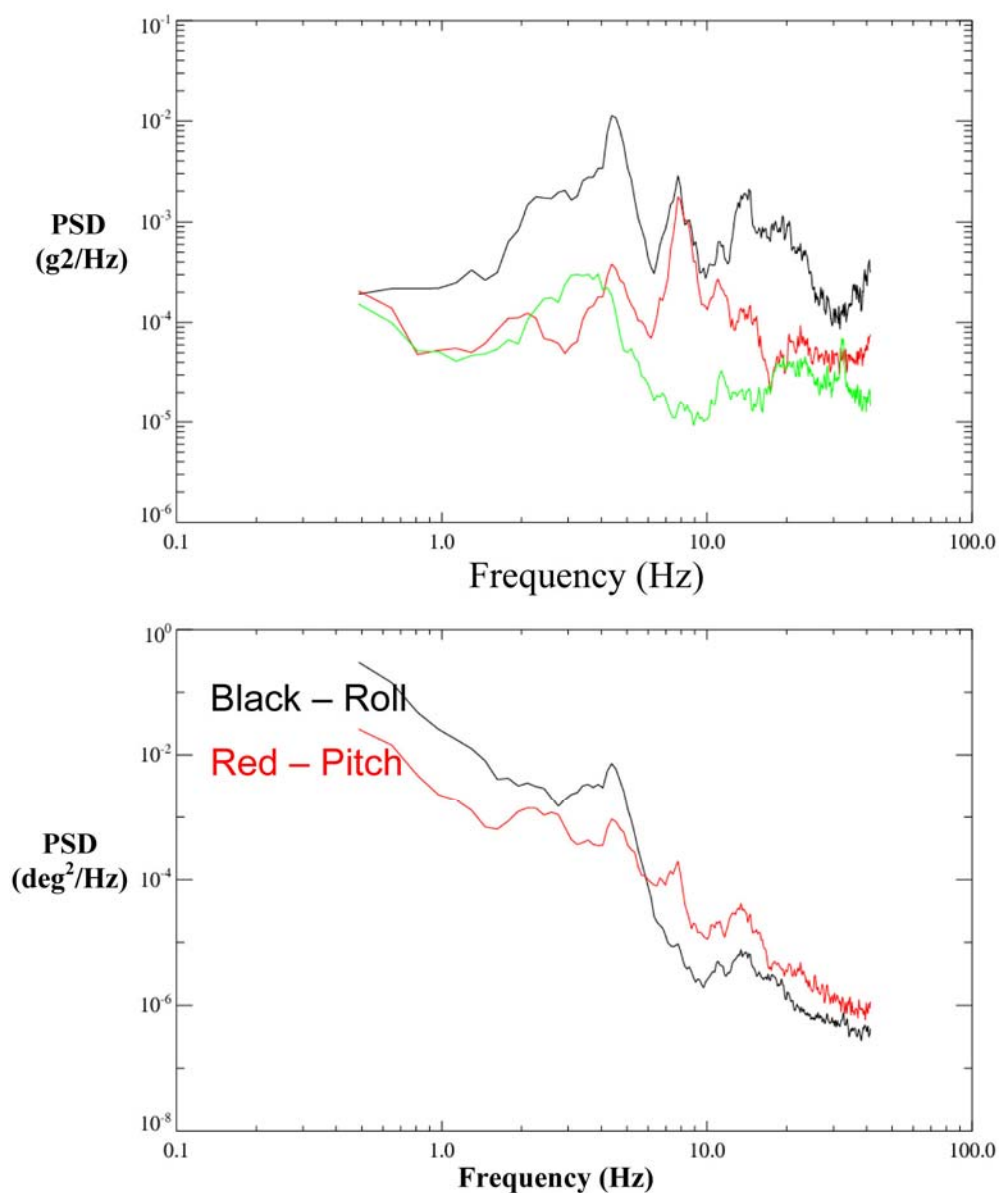
Figure 4.   Power spectra of platform motion measured by MTADS GEM array at YPG Test Site.

2.2.   Measuring Sensor Orientation

The orientation of geophysical sensors is measured through deployment of solid-state IMUs deployed concurrently on a test platform. New IMU technology provides a significant cost and performance advantage from traditional mechanical gyros. Solid-state IMUs assist in positioning and navigation of airborne and ground-based platforms and include altitude/height indicators and directional gyros. Platforms also typically have a compass, and in some cases a flux valve connected to the directional gyro to cancel long term drift.

Mechanical IMU instruments (height indicator and directional gyros) are driven by a spinning wheel (mass) that obeys simple physical laws. The mass is spun up either electrically (electric gyros) or via airflow (vacuum gyros) to high rotational speeds and a high angular momentum. The spinning wheel is mechanically isolated from the casing of the instrument thru a series of gimbals. Due to the conservation of angular momentum, the spinning wheel will try to maintain its orientation, via the gimbals, as the outer casing moves. The gimbals, move by the amount the platform has rolled, pitched, or changed heading, and in some cases directly connect to the display.

While mechanical IMUs have been used in aircraft for many years, there are a number of issues that make them problematic, especially for ground-based platforms. The foremost problem is long-term reliability because mechanical IMUs are constructed with many moving parts with close tolerances; they break easily. As the ball bearings that support the high-speed wheel and the gimbals begin to wear, they contribute to precession errors. Compounding the issue with vacuum gyros, is that dirt and dust in the vacuum line that destroys the bearings. A second class of problems is the limited accuracy and resolution of most mechanical gyros, which results in limited accuracy and resolution, especially in dynamic maneuvers.

The ring laser IMU is a highly accurate way to measure changes in angular position without the use of spinning mechanisms. An angular rate sensor, however, does not directly measure attitude like a gimbaled mechanical gyro; instead it measures the rate at which an object rotates in degrees per second. Deployment of three ring laser gyros on the XYZ axes of a platform allows for continuous calculation of a level reference and the change in roll, pitch, and heading. The ring laser IMU systems, with their "strapdown" construction are an alternative to mechanical gyro systems in many applications. The constraint of ring laser gyro navigation systems is high instrument cost (>$100K) due to required glass machined cavities, precision mirrors, high voltages (> 1kV), lasers, and inert gases.

A significant breakthrough occurred when techniques in silicon fabrication technology allowed for the creation of accurate inertial sensors in silicon. This technology is known as Micro Electro-Mechanical Sensors (MEMS), and is in high volume production today. Low-cost ($5-10K) solid-state gyro MEMS technology has been used in the commercial, industrial, and aerospace markets since 1999 to make platform roll, pitch, and heading measurements. For our initial measurements of sensor orientation effects, we used the Crossbow Solid State IMU, known as an Attitude-Heading Reference System (AHRS). The AHRS uses a 3-axis accelerometer and a 3-axis rate sensor to make a complete measurement of the dynamics of the sensor system. The addition of a 3-axis magnetometer inside the

AHRS allows it to make a true measurement of magnetic heading without an external flux valve. The AHRS is a solid-state equivalent of a vertical gyro/artificial horizon display combined with a directional gyro and flux valve. The AHRS unit is low power (< 0.3A), reliable (> 20,000 hr mean-time-between-failure [MTBF]) and accurate (better than 2 degrees in roll and pitch). The AHRS has a digital computer compatible output (RS-232). Packets of digital information containing roll angle, pitch angle, and heading angle are sent out in standard serial format up to 70 times per second. This makes it straightforward to integrate with digital displays – like those in MTADS trackguidance systems, and to incorporate with the RIS Handheld Interface Pod (HIP box) DAS.

For initial performance analysis of this technology, we utilized software displayed on standard laptop computers. "GyroView" runs on Windows-based laptops and Windows CE based handhelds (Figure 5). The AHRS must be securely fastened to the sensor platform, and installed on a level surface with the connector facing aft. Because the magnetometer is built into the instrument, installing near large amounts of magnetic material, or moving magnetic objects needs to be avoided. Testing was required to determine if the primary transmit field of the electromagnetic induction (EMI) sensors affect the magnetic heading readings. A composite-material cart system is well-suited for mounting and use of this product. The unit is powered by 8-30 VDC and uses about 0.3 A.

Once installed, a heading calibration is required to compensate for any magnetic field created by the platform. This calibration consists of operating the unit in calibration mode, and rotating the platform in a circle. Unlike some other heading systems, there is no need to position the platform in any specific direction provided at least one complete circle of calibration data is collected.
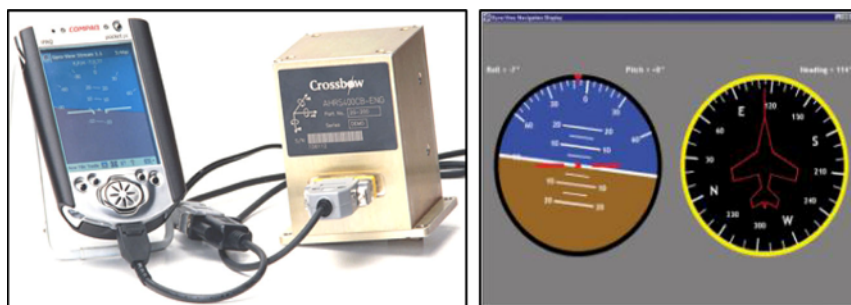
Figure 5.   Crossbow IMU running with software on handheld (left) and laptop computers (right).

The Crossbow IMU was used in a series of tests to evaluate the effects of sensor orientations. These tests were conducted in the laboratory, at a constructed test platform, under controlled conditions (referred to

as "pseudo-surveys") to capture the motion of the sensor and define the effects of orientation under idealized conditions, and at a seeded test plot at the FLBGR site in Colorado.

For these initial tests to analyze sensor orientations, a cart system was utilized to allow the placement of various geophysical sensors and the positioning devices (Figure 6). In addition to the positioning system, a supplemental IMU was used to capture platform orientation data. The DAS integrated the geophysical, navigation, and orientation streaming data using a HIP box and ruggedized portable computer. The Geonics EM61-MKII sensor collected the geophysical data. The EM61-MKII is a time-domain EM metal detector that generates a pulsed EM field then records the decaying induced secondary field at 4 time intervals. A Leica TPS1100, dual-laser robotic total station, collected positioning data at ~3 Hertz (Hz) with an accuracy of ±2mm + 2 PPM in all three directions (X, Y, Z).

Figure 6.   The Leica TPS 1100 Robotic Total Station (right) tracks a prism mounted on the deployment system at 3 Hz with and accuracy of ± 2 mm + 2 PPM in all three directions (X, Y, Z).

2.3.   Laboratory Data

Laboratory tests were conducted to measure the affects of the IMU and the EM61-MKII. Although it was already known that the primary field of the EM61-MKII distorts the heading measurements of the IMU, it was unknown as to whether the EM61-MKII primary field would affect the roll and pitch measurements. In addition, we tested whether the proximity of the metal case of the Crossbow IMU metal case to the coil could cause a response in the EM61-MKII secondary field measurements.

To understand these potential effects, a simple test was conducted in which the IMU was placed at several heights above the EM61-MKII coil while the IMU and EM61-MKII recorded measurements. The mount holding the IMU platform maintained the sensor level during each test. With the platform level, only the EM61-MKII could affect the IMU measurements.

As suspected, the EM61-MKII affected the heading (yaw) measurement of the IMU but had no affect on the acceleration or angle measurements. The IMU affected the response of the EM61-MKII as the IMU's metal case approached the EM61-MKII's primary coil. It was determined that placing the IMU within 38 cm of the coil contributes very little to the noise of the EM61-MKII.

Since the primary field of the EM61-MKII overpowered the yaw axis measurements, measurements were not used in determining sensor position; the yaw angle was instead calculated from the positioning equipment. The 38 cm offset allowed us to minimize the lever arm between the axes of pitch and roll rotations and the IMU that measured the angles and accelerations. The IMU uses the acceleration measurements to stabilize the angular measurements for the roll and pitch, therefore minimizing the acceleration improves the angular measurements.

2.4. Platform Data Collection

Signatures from various UXO and non-UXO items collected from a test platform were used to document the change in target signatures due to orientation variation in the recording sensors. This project leveraged the ongoing work at FLBGR where the US Army Corps of Engineers (USACE), Omaha District, had generously made available a test platform constructed in January 2003 from non-metal components for analysis (Figure 7).

Figure 7. The platform was constructed to allow items to be geophysically characterized at sensor offset of up to 8 feet. Below the wooded platform floor was a jig used to house the test items at measured offsets and orientations. Signatures were collected from various UXO, non-UXO, and calibration items.

The as-built platform was 8 feet in height, using an array of posts set in concrete (the concrete aggregate was tested for magnetic and EM responses prior to pouring), had an open deck area of 20 ft by 20 ft with side rails, and stairway access. Also, a wooden jig was fabricated to hold any of the selected munitions and non-munitions items to be measured in a complete range of static positions – that is, "depths," azimuths, and inclinations – appropriate for testing.

As discussed below, a series of measurements were made on the test platform to support the analysis of signatures from various EMI and magnetic field sensors, including Geometrics G858 total field magnetometers, Geonics EM61-MKII, Geonics EM63, Geophex GEM-3, and Zonge TEM (Time Domain EM). Signatures were collected from various UXO, non-UXO, and calibration items.

High resolution, high fidelity geophysical data were collected by Shaw on the platform to define the object signatures by all sensors, except the TEM data, which was directly collected by Zonge. The free-air test platform survey data (Figure 8) were collected across an area with dimensions of approximately 16-ft by 16-ft, that is, large enough to collect data from background through peak anomalous readings back to background. Positional markers were marked on the platform on 1-foot centers (1 by 1 foot interval grid system). The platform grid was oriented in the north-south direction corrected for magnetic north declination, which for this area is approximately 11.5 degrees east.

Figure 8.   A non-metal platform was constructed at the FLBGR, in Denver Colorado. This platform was used to measure various geophysical signatures from UXO and non- UXO items.

Data were captured at precise 1-foot intervals over a foot square grid on the top of the platform in a static mode. Below, the test items were placed in a cradle with configurable heights. The primary focus of the data collection was a K941 shipping container (referred to as a PIG). Additionally incendiary bombs, SCAR rockets, and other non-UXO were tested. The PIG was positioned 14.5-inches (38.83 centimeters [cm]) below the top of the platform. A PIG is a cylindrical steel container measuring 40-inches in length, 6.625-inches in diameter, and 0.145-inches thick. The PIG has one open end, which is capped with a 9.25-inch flange blank by eight bolts and a 0.125-inch thick lead gasket. The approximate weight is 80 lbs. Prior to placement of the PIG, a background survey was conducted with the coil sitting on the deck.

These static datasets furnished high-resolution values across a well-defined anomaly surface for further discrimination activities. The PIG was oriented at six azimuth orientations and at nine dip angles for the magnetic test data. For the magnetometer data, the azimuths consisted of 0°, 16°, 45°, 90°, and 315°. For the EM data, the azimuth consisted of 0°. The magnetic and EM dip angles consisted of 0°, 15°, 30°, 66°,

and 90°. All data were obtained at three different depths, 0.5 feet, 2 feet, and 4 feet below ground surface. This approach provided high-resolution signatures of the target in a controlled environment. In addition, data were collected without a PIG in the jig below the platform to document the target-free platform background readings.
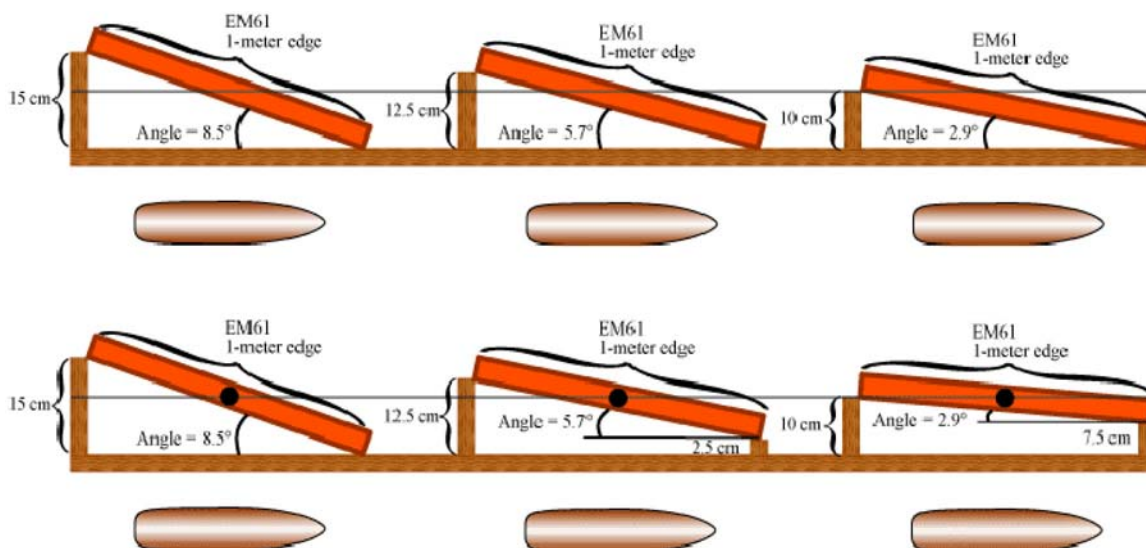
Figure 9. Platform sensor orientation tests were conducted in two modes. First (top) the sensors were simply tilted at measured angles to quantify the effects of pitch and roll. Since this tilting changes the sensor- target offset distance, a second set of tests were conducted (bottom) where the offset was unchanged.

Subsequent analysis for this effort focused on the PIG data collected with Geonics EM61-MKII sensor. Two sets of sensor orientation tests were conducted. In the first test (Figure 9, top), the EM61-MKII was tilted on edge by simply elevating one side of the sensor. While this provides information regarding sensor orientation, the tilt of the sensor changes the distance from the sensor coil center and the target below. Consequently, a second set of tests were executed where the effects of each rotation axis orientation was surveyed independently. Under these tests, the tilted sensor maintains a constant sensor-target offset (Figure 9, bottom). This provided sensor responses capturing each orientation parameter separately (yaw, pitch, roll, and elevation). Yaw tests were conducted by rotating the sensor 2.5 degrees clockwise and counterclockwise from a north/south orientation (Figure 10).

Initial tests where the sensor was tilted from one edge quantified the variability often seen in EM61 MK-II field data. The results show that the elevation of the sensor above the target plays a critical role in contamination of the recorded signal (Figure 11). The elevation of the sensor causes a root mean square (RMS) change in the target signature about 10 times more significant than the associated RMS change

due to the sensor angle. For example, if the EM61 is "rolled" by 11.5 degrees, then the center of the sensor is elevated by about 10 cm. An RMS change in the recorded signature of 11% is caused by the change in sensor height (relative to the target), while the RMS change purely due to the sensor angle is only about 1%.
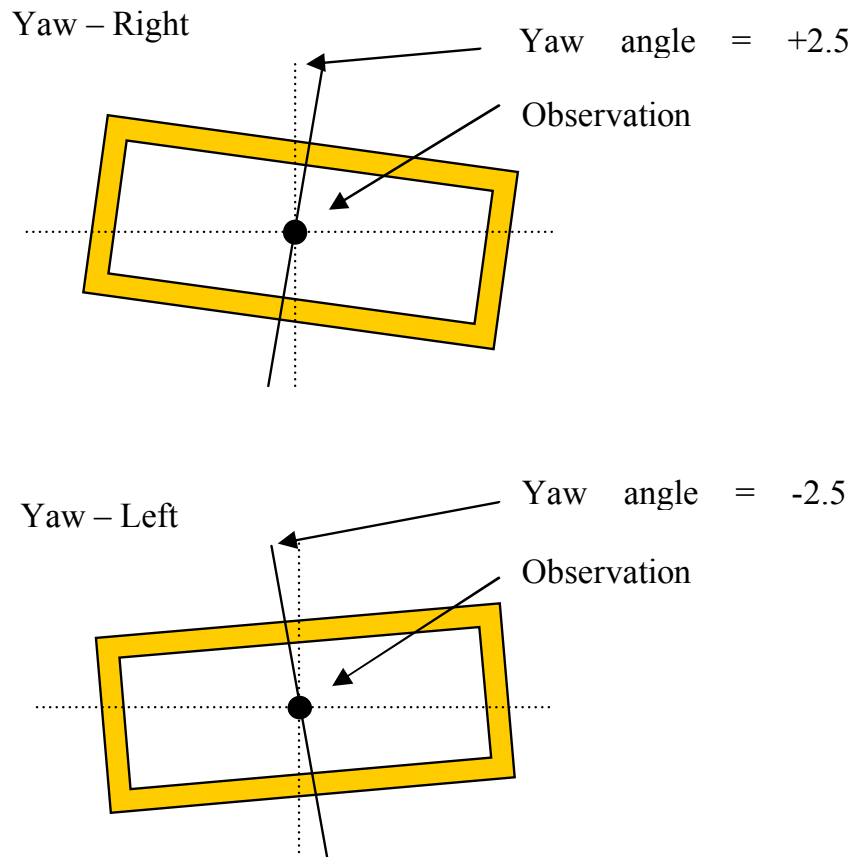
Figure 10. Orientation schematic for platform yaw tests. The EM61-MKII was placed flat of the platform deck with the sensor oriented 2.5 degrees clockwise and counterclockwise from north.
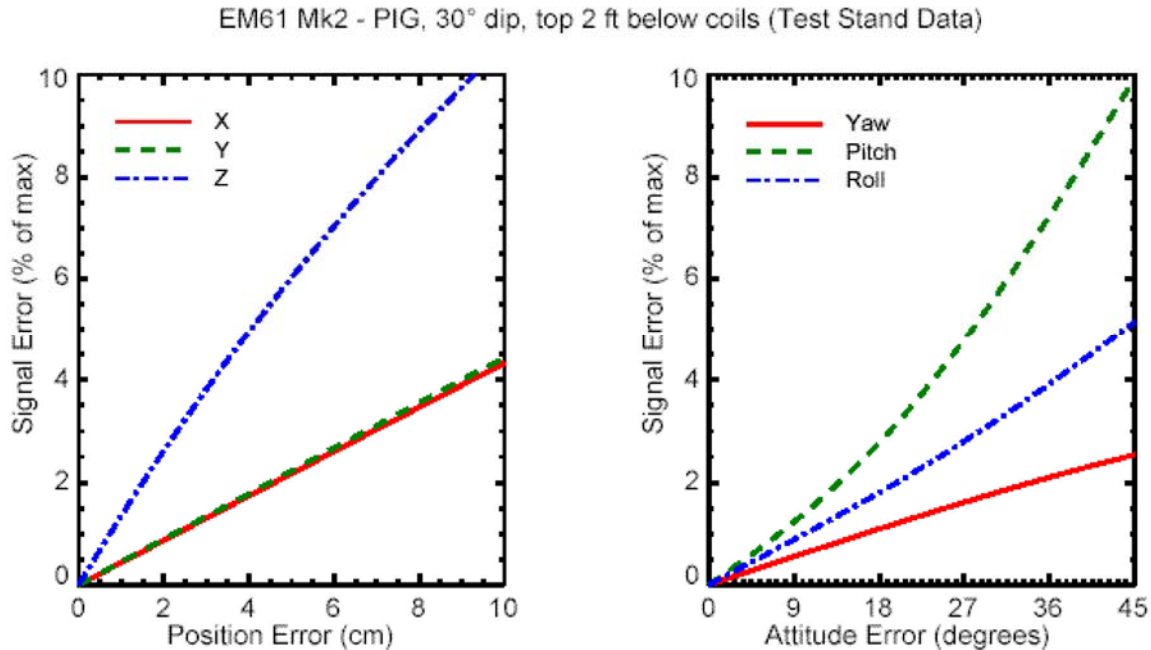
Figure 11. Analysis results showing sources of RMS error associated with geophysical signatures collected from a Geonics EM61-MKII instrument.

The tilt (roll) of EM sensors causes significant changes in the recorded signatures. We saw a 30% reduction of the peak amplitude when the sensor was tilted by 5.5 degrees (relative to data when the sensor was flat). However, our modeling results indicate that these changes are mainly due to the change in distance between the coil and the target, and not primarily caused by angle-induced changes in the target EM response.

The effect of yaw and pitch angles is also provided in Figure 11. As anticipated, yaw (twisting) has a smaller effect than pitch and roll. The pitch of the sensor (forward and back) has the strongest effect due to the asymmetric 1.0 x 0.5 m coils configuration of the EM61-MKII. In terms of position, the vertical distance between the target and the sensor is about 3 times more important in terms of RMS signature than the XY location.

The second tests defined the effects of yaw and pitch by rotating the EM61-MKII about the center of the coil. The results show a very strong variability in EMI signatures from all four parameters controlling sensor orientation (yaw, pitch, roll, and elevations). For the PIG target 2 feet below the platform, elevation shows the strongest effect with a change in response of between 264 mV to 288 mV/cm offset change, or between 7.4% and 8.0% change of the peak amplitude per cm change in height. Signatures

collected when only the roll angle was changed showed a 27.1 to 72.7 mV/degree variability in amplitude, a range of between 1.0% and 2.5% change of the peak amplitude per degree of roll. Pitch results were similar, and showed a 19.3 to 41.8 mV/degree variability in amplitude, a range of between 0.53% and 1.15% change of the peak amplitude per degree of pitch. Yaw results were also similar, and showed a 7.6 to 34.0 mV/degree variability in amplitude, a range of between 0.17% and 0.74% change of the peak amplitude per degree yaw. Typical results are shown in Figure 12.
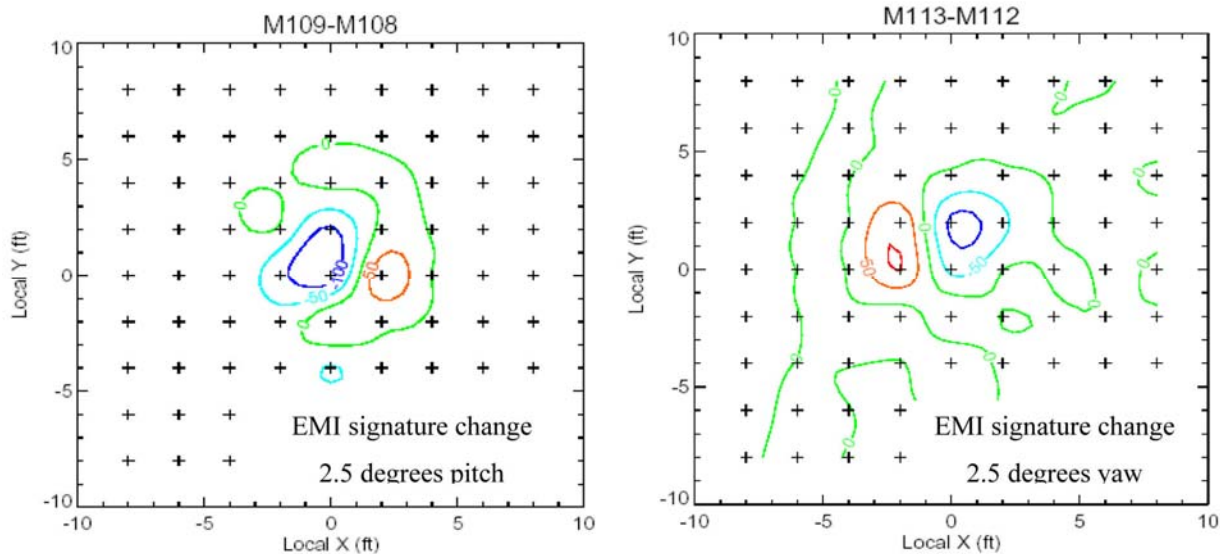
Figure 12. Variation is the sensor yaw (left) of the EMI responses from a pitch angle of 2.5 degrees with the center of the coil changing elevation. Variation of the EMI responses from a pitch angle of 2.5 degrees (right) without the center of the coil changing elevation.

In conclusion, the platform test results can be summarized as follows:

- Noise levels of 1-3 mVolts are approximately 0.03% of maximum signal;

- Target height causes strong variation in signature responses; for example, 6% amplitude change per cm offset was seen;

- The sensor angle causes strong variation in response, causing an increase in the complexity of signatures.

2.5.   Evaluation of Pseudo-Survey Data

To systematically increase the complexity of the tests conducted to evaluate sensor orientation effects, a series of tests were conducted under controlled conditions, referred to as "pseudo-surveys," to capture the

motion of the sensor and define the effects of orientation under idealized conditions. Specifically, these tests were conducted to demonstrate dynamic versus sensor orientation effects; to evaluate controlled sensor orientations with respect to yaw, pitch, and roll; to evaluate the effect of vibration; and to evaluate system integration and precision using precise laser navigation and IMU technology.

The deployed DAS utilized the RTS laser navigation, Crossbow IMU, and the EM61-MKII sensor (Figure 13). A test lane was established with 11 2-inch trailer hitch balls located 10 feet apart. Initially, a background survey was conducted by moving the cart system along a 100-foot line. Subsequently, a series of roll tests were performed by rolling one wheel over a wooden ramp (Figure 13). A digital video camera was placed along the test lane to record the roll angles.

Figure 13. Controlled surveys were carried out to define the ability of the data acquisition to collect sufficient orientation and positioning data. Eleven trailer-hitch balls were placed 10 feet apart (left) along a test lane. Ramps were used (right) to subject the system to specific roll angles.

Positioning data were corrected for roll and pitch using their respective angles measured by the IMU (Figure 13). Controlled surveys were carried out to define the ability of the data acquisition to collect sufficient orientation and positioning data. Eleven trailer-hitch balls were placed 10 feet apart (left) along a test lane. Ramps were used (right) to subject the system to specific roll angles.

Next, several pitch tests were executed by moving the cart system in an undulating motion about the lateral axis (Figure 14). Plastic pin flags were cut to length and attached to the front and rear of the EM61 primary coil to control the pitching angles.

Figure 14 (bottom) shows an example of the amplitudes decreases and spatial inaccuracies introduced from pitch variability. An increase in amplitude of between 10% - 20% was seen based on the direction of the pitch of the sensor as it passes over the target. The position varied up to 2.5 feet based on pitch angles of approximately +/- 20 degrees.
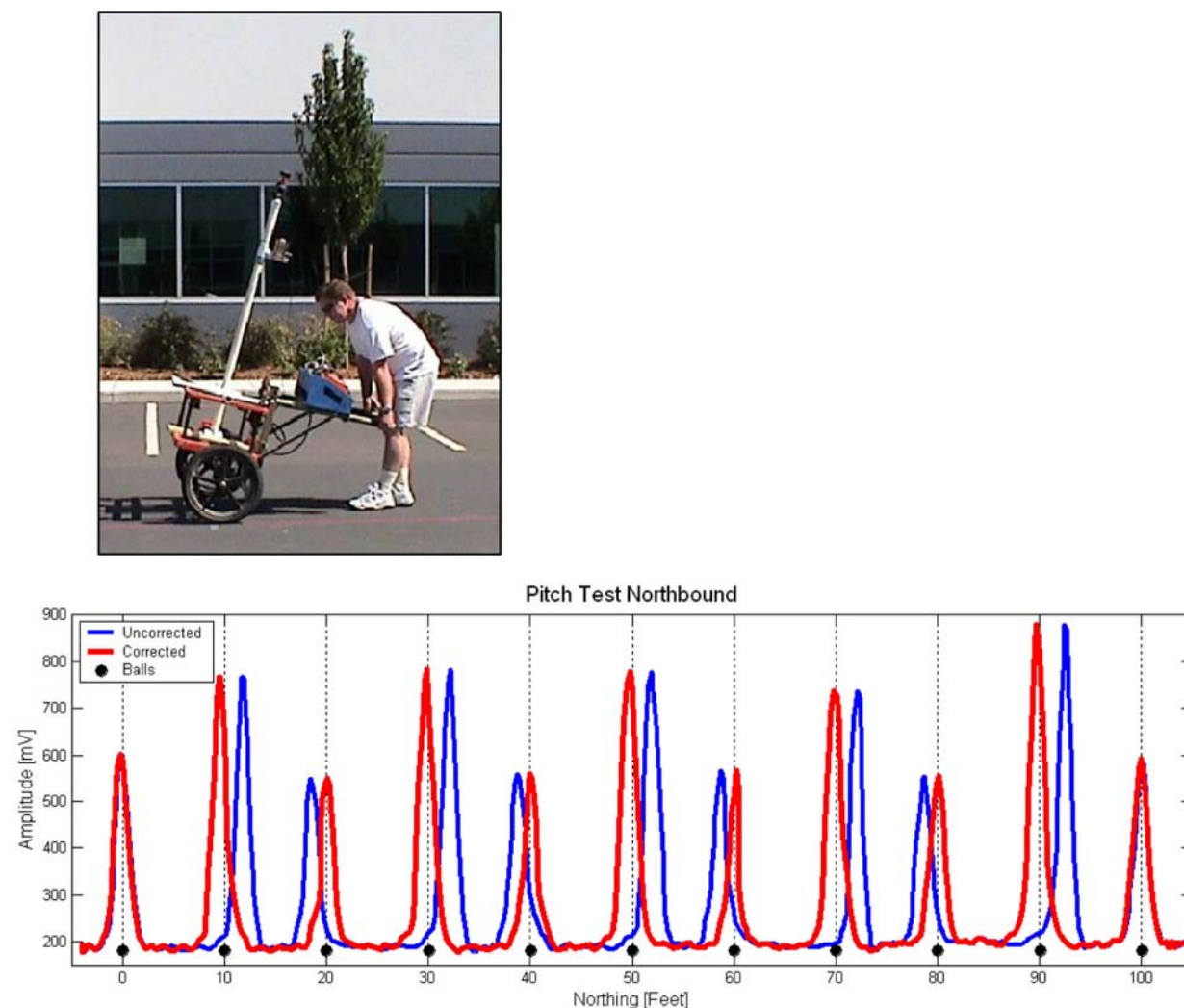
Figure 14. Controlled pitch tests were executed to define the effect of sensor pitch on the amplitude and location of small spherical targets. Uncorrected data (blue) compared with gyro-corrected data (red). The X-axis is position and the Y-axis is geophysical response in millivolts. The black circles represent anomaly locations.

In summary, strong effects were seen from modest controlled sensor motion; sensor roll and pitch clearly create variations in the positioning of the sensor. We also found that hardware improvements were necessary for required orientation definition; these improvements include modification of the IMU to

replace the metal casing for co-location with sensor coils; increase in cart system rigidity; and increase in timing of the RTS/sensor/IMU timing to 10 ms.

2.6.   Conclusions on the Effects of Sensor Orientations

Our tests show that variation in EMI sensor orientation causes significant changes in EMI signatures. In general, for a cylinder target at a depth of 0.5 m depth, a 7-8% reduction in peak amplitude per cm was seen due to sensor – target offset. For the item analyzed, when orientation is separated from offset, peak amplitude changes between 0.5% and 2% per degree. Roll angles are more significant then pitch, which are in turn more significant than yaw.

Changes in EMI signatures, if unmeasured and not incorporated into the inverse modeling, make EMI data inadequate for UXO modeling in realistic conditions. Without compensation for orientation effects in EMI data, EMI sensors cannot be used with reliability for UXO discrimination.

Last, yaw, pitch, and roll data can be collected using IMUs to accurately measure sensor orientation during EMI data collection. Data collection hardware improvements are needed for required orientation definition. With respect to the platform, reducing sensor orientation may be achieved by using gimbaled coils to minimize motion and a coiled suspension to minimize shock. For positioning, the RTS technology has been shown to offer precise measurements that can be synchronized with IMU measurements. A commercial off-the-shelf was used for these tests, however, it was found to be susceptible to corruption by the EM coils magnetic field. Additionally, commercial IMU devices are made of metal and influence the EM sensor measurement. Although problematic, the IMU data can still be used to allow for the correction of sensor orientation effects on positioning to properly spatially register the geophysical data.

3. PROTOTYPE LOW METAL IMU

Recognizing that mitigation of all sensor orientation variability may be not be readily achievable, in Year 2 we undertook the development of an instrument to measure the orientation of the sensors as they are deployed. The sensor orientation Year 1 tasks demonstrated that off-the-shelf IMUs may not be adequate to make these measurements, as measurements from commercial IMU devices are corrupted by the EM coils transmission of a primacy magnetic field. Additionally, commercial IMU devices are made of metal and influence the EM sensor measurement.

3.1. IMU Prototype Development

During 2003, RIS Corporation investigated commercially available integrated accelerometer circuits that may be of interest for pitch and roll sensing. Accelerometers such as these could be used in portable survey equipment to provide additional positional information for correlation of measurement data with the incline of the survey equipment with respect to the landscape and target objects.

For pitch and roll measurements, the ability to measure inclines of +/- 90 degrees with 0.1 degree accuracy is desirable. The Analog Device ADXL311 was identified as a suitable accelerometer, and samples of this device were obtained. The ADXL311 provides dual axis measurement of up to ± 2g dynamic or static acceleration. The device, based on third generation technology, can survive shocks of 3500 g which makes it less susceptible to damage which could occur during fabrication. The dual axis feature allows one device to measure both pitch and roll in a portable platform. The noise floor for the device is low enough to allow measurement of 0.1 degree with a 10 Hz bandwidth. In addition, the device measures only 5 mm x 5 mm x 2 mm and requires less than 1 mA from a 3 Volt power supply, so it is well suited for low power portable operation.

One ADXL311 was used on a prototype board to verify its operation. It provided voltage changes from each axis as the board containing the device was tilted through various angles. The measured voltage could be correlated to the pitch or roll angle through the formula:

$$\text{Pitch or Roll in degrees} = \text{ASIN}(A),$$

where A is the voltage measured from the axis of interest divided by a scale factor of approximately 167 mV/g.

RIS Corporation designed and fabricated an integrated circuit board containing the ADXL311 chip housed in a plastic case (Figure 15). The circuit board also contained an EM sensor to interleave the orientation measurements between the EM61 magnetic pulses. Unlike with commercially available IMU devices, the plastic case and lack of substantial metallic components allows the IMU to be placed very near the sensor.
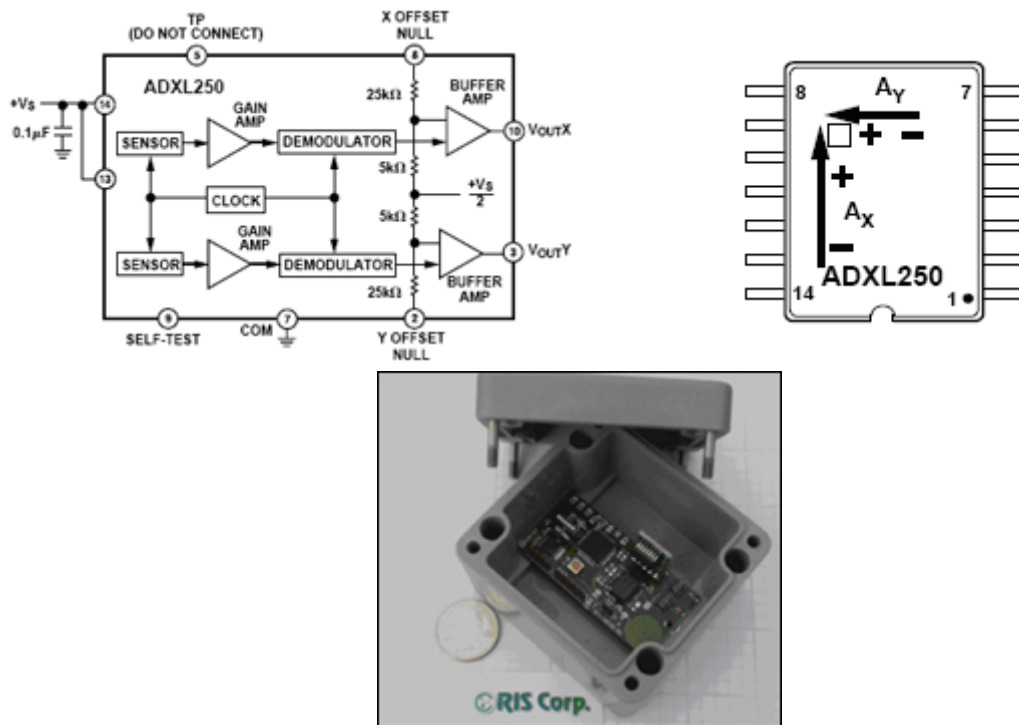
Figure 15.   Simple block diagram of the ADXL250 chip (top left), orientation and pin layout of ADXL250 chip (top right), and integrated circuit board with plastic housing of the low metal IMU (bottom).

The system was designed for integration with RIS Corporation's HIP box, which time stamps and concatenates asynchronous serial data streams into one serial output stream. The HIP box interfaces with various instrument platforms and provides flexibility to the IMU. The HIP box is configurable using software on a tablet or notebook PC, which also act as data logging and visualization software.

3.2.   IMU Prototype Testing

The IMU response to angular variations was measured using a tilting platform with stops at known angles. The first test measured the static response and drift; the results are shown in (Figure 16). Tests were conducted to measure the static and dynamic response. Figure 17 shows the response of the roll

measurements between 2 angles, 5° and 15°. A high rate of angular change was used to simulate field conditions.
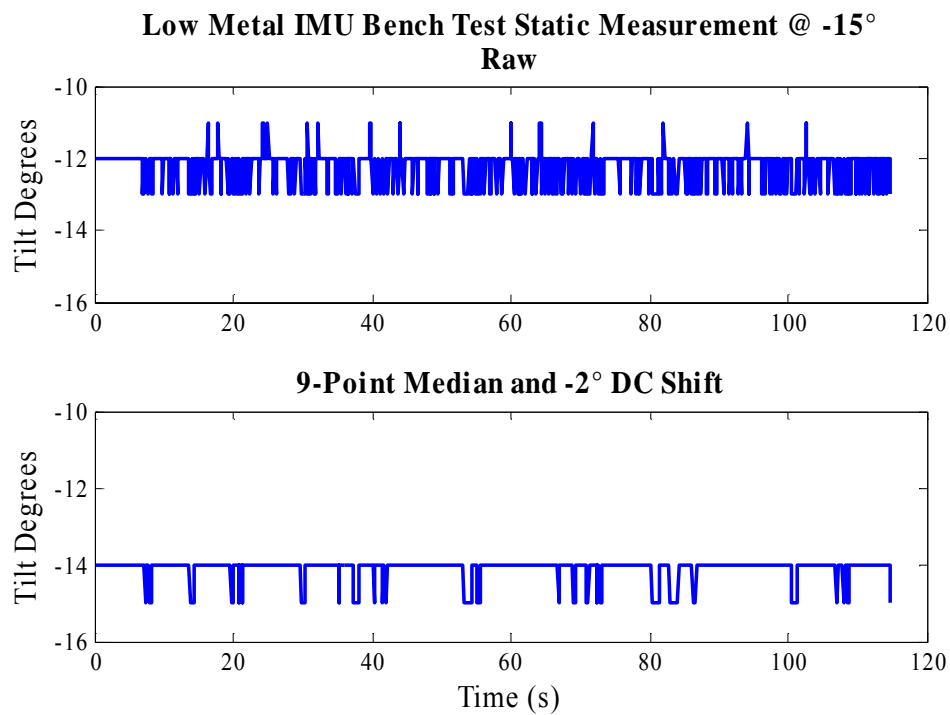
Figure 16. The static measurement of the low metal IMU at 15°. The data required filtering using a 9-point median filter and a static -2° DC shift to smooth the response.

Low Metal IMU Bench Test Dynamic Measurement Between -5° and -15°
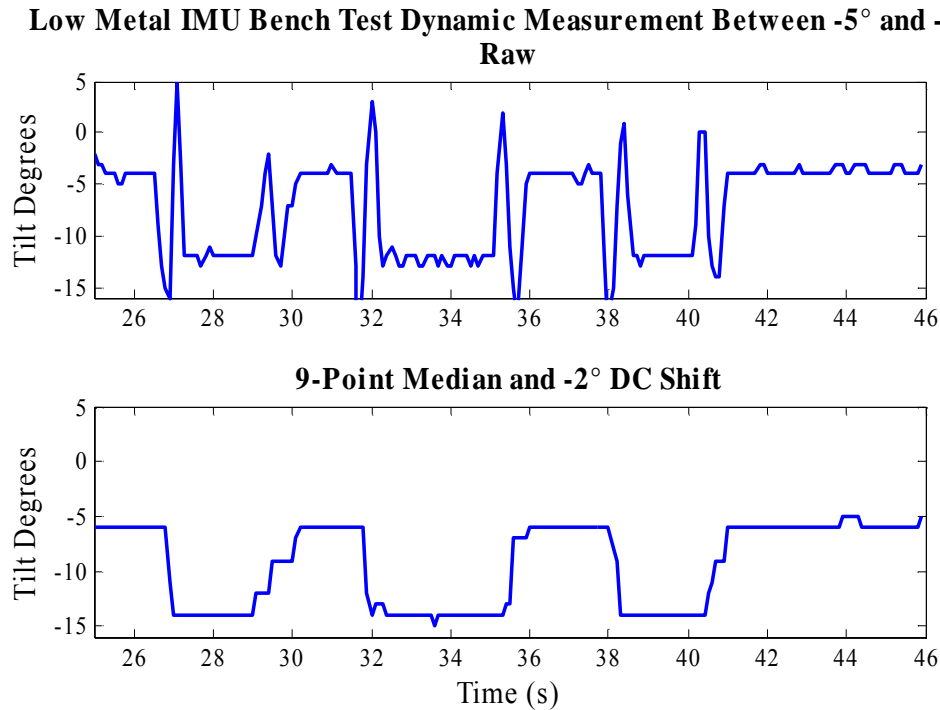
Figure 17. The measured dynamic IMU roll response while the sensor is rolled between 5° and 15° very quickly. The data required filtering using a 9-point median and a -2° DC shift to smooth the response.

3.3. IMU Prototype Conclusions

In tests of the prototype IMU, we found that while the prototype IMU worked well under most bench-top conditions, the unit failed to provide reliable measurements during many survey tests. The low-metal IMU appeared to generate accurate pitches and roll angles when the system is not experiencing high angular accelerations. During times of high accelerations, the IMU data requires the application of a significant filter to smooth the readings. Therefore, in Year 3 we undertook improvements of the IMU device to mitigate the need to apply filters to remove high frequency noise.

IMU improvements in Year 3 included faster polling of the Analog Devices ADXL311 accelerometer and measurement stacking. Increasing the sampling rate from 10 to 20 Hz facilitated measurement stacking which removed some of the spikes in the measured values of roll and pitch angles. The averaging also stabilized IMU readings during accelerations, but only modestly. However, the IMU remained unreliable after several firmware reconfigurations and tests conducted during data collection in 2005. Consequently, the low metal IMU was determined inadequate for further data collection efforts the commercially available Crossbow AHRS-400 IMU was used for subsequent field data collection in 2006.

4.   GIMBAL SENSOR SYSTEM

Sensor orientation effects were found to be a major impediment to improved discrimination capabilities. To address this issue, we pursued to paths concurrently, hardware technology development and EM data modeling technology (discussed in Section 6).   The primary hardware technology development task undertaken for this project consisted of the development and testing of an improved data collection platform consisting of a gimbaled cart system, EM sensors, RTS navigation, IMU, and a DAS.

4.1.   Gimbal Cart

4.1.1.   Design

Tom Glenn, UTC, designed a gimbaled mounting system with the following characteristics: zero metal construction; gimbaled sensor system such that the EM61 sensor is free to rotate in the pitch and roll axis when deployed; and single or dual EM coil configurations.

The platform is a lightweight, non-metallic pushcart.   The use of non-metallic components results in a negligible EM signature.   The system consists of a wheel/axle assembly, a frame assembly, a yoke assembly, and the EM61 sensor assembly.   In this configuration, the wheel and axles are fixed.   All the wheel/axle components were constructed from non-conductive materials to eliminate EM signature effects (Figure 18).   The EM61 remains aligned with the gravity vector regardless of the orientation of the mounting frame and deployment platform.

Figure 18.   Gimbaled cart after construction and ready for testing. Counterweights (white blocks) were used to offset the non-symmetric EM61 primary coil.

The frame assembly is used to support the yoke assembly with the gimbal system, the EM61 assembly, and the wheel and axles. It was also made from non-conductive materials to reduce EM signature effects. The frame allows for the mounting of GPS electronics and EM electronics on the handlebars. The frame was made from standard extruded fiberglass; the components are fabricated from stock materials and assembled using standard non-metallic fasteners. Solid fiberglass inserts reinforced the joints to improve strength, stiffness, and durability. Some components were joined using fasteners; permanent connections are bonded using adhesive suitable for use with fiberglass in outdoor environments.   The unit was designed for shipping and fits into a standard bicycle plastic shipping container.

The yoke assembly contains four shafts that, along with four non-metallic bearings, make up the gimbals. The gimbals consist of the fiberglass shaft turning on a low friction non-metallic, self-lubricating bushing. The yoke assembly was also constructed from extruded members as well as fiberglass plate gussets. The joints are connected using fiberglass bolts. Small spacers were used to mate the gusset flat surfaces to the round tubes. The use of the yoke assembly internal to the perimeter of the EM coils creates a very compact unit that assists deployment and shipping. Pivot bars containing pivot adjustment holes were connected to the EM assembly and to the frame assembly.   These bars are removable to allow the insertion of the yoke assembly into the EM assembly. The pivot bars contain the pivot bearings, which were slid over the shafts projecting from the yoke assembly.

Figure 19 shows the rotation around the pitch axis of the EM assembly (pitch being defined as rotational movement in the direction of translation or along track). For large excursions, the sensor will contact the frame depending upon the pivot point.
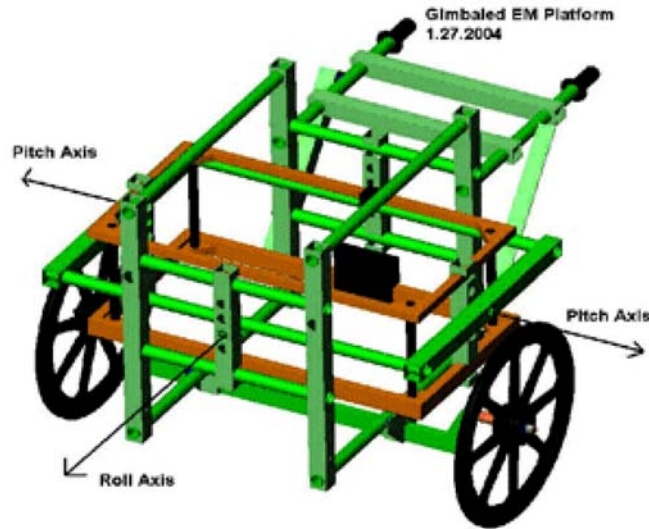
Figure 19.   Model design of the gimbaled cart and the axes of motion.

4.1.2.   Dynamic Motion and Damping Analysis

Another area of investigation besides geometry is the dynamic action of the EM sensor when disturbed. The dynamic action of the sensor is governed by mass, inertia, damping, and pivot location. If no damping exists, the EM sensor will oscillate for long periods when disturbed. This damping factor is made up of two parts: a damping due to friction in the bearings and a damping due to a rotary damper installed on the axis of rotation.

We found that the amount of friction in the bearings exerted enough force to damp the oscillations, and the rotary dampers were not installed. As shown, the unit oscillations will decay to approximately zero in around 3 seconds when disturbed to an excursion of 30 degrees, which represents the maximum specified excursion (this specification is subject to change as desired).

The simulation shows that without some damping of one form or another, the EM sensor will require a significant amount of time to reach dynamic equilibrium (Figure 20). If one imagines that the gimbaled EM platform is pushed at a rate of around 1 mph or approximately 1.5' per second, then a multiple second decay time results in significant ground covered before dynamic equilibrium is reached.
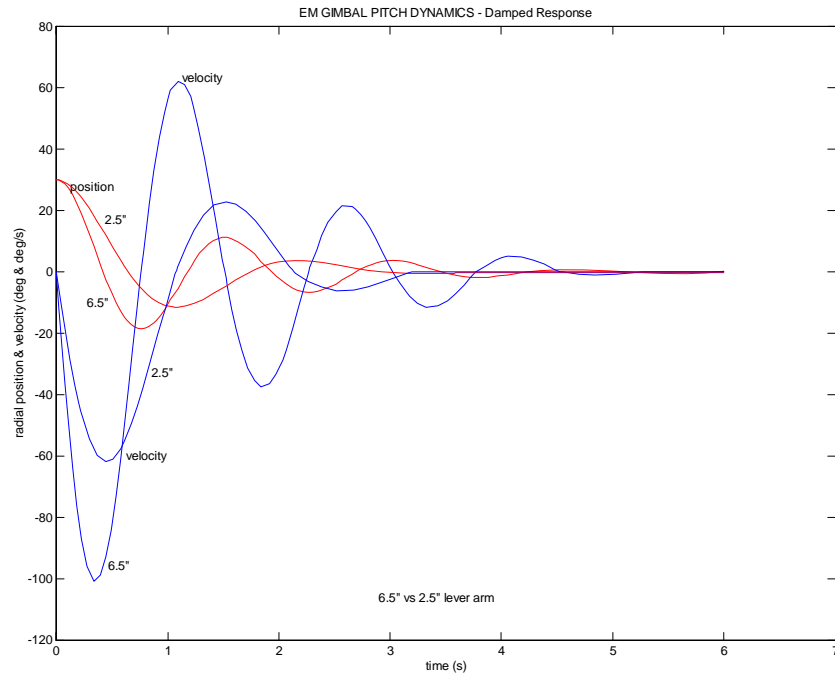
Figure 20. Results from modeling the damping motion of the gimbal system. This shows the velocity and positions as a function of time as the gimbals are deflected 2.5" or 6.5".

4.1.3.   2005 Gimbal Cart Design Improvements

The gimbaled sensor system developed as described above was tested in 2004 (in controlled tests and field tests at the Ashland Test Plot, FLBGR, and Lake Success Business Park as described in Section 5) and shown to mitigate sensor roll and pitch inherit in surveying with a wheeled platform. As documented in the 2004 Annual Report (Foley 2004), the developed system was able to significantly reduce variability of sensor orientation due to effects of topography and irregular surface conditions. However, additional improvements were identified to improve the orientation variability mitigation for the final survey planned for early 2006. Therefore, improvements were made in 2005 to the system that included:

- Improved and redesigned coil mounting;
- New pivot operations to improve response of gimbal by replacing old bearing system with nylon ball bearings;
- Improved mounting of IMU to locate device at sufficient distance from the sensor coil to eliminative all sensor interference;
- Improved instrument electronics location to redistribute weight for improved operator ergonomics; and
- Redesigned and counter-weight to offset the weights added and re-distributed by system changes.

4.2. Geophysical Sensors

The standard Geonics EM61 – MKII unit was used with the gimbal cart for all data collection conducted as part of this project and described in Section 5. This unit has 1.0×0.5 m coils.

4.3. IMU

As described previously, a prototype low metal IMU was developed in Year 2 of this project and was intended to replace the Crossbow IMU used previously. During field testing for this project in Year 3, the prototype low metal IMU was determined to be inadequate for the data collection surveys based on failed attempts to reduce noise levels and increase reliability. Data collection for this project after the 2004 field tests were conducted using the Crossbow IMU.

4.4. Positioning

In early 2004, Leica Geosystems released a new RTS, the TPS 1200 (Figure 21), which had a number of improvements over the older TPS1100 model used in the initial measurements of sensor orientation effects. The beneficial upgrades to the RTS were a faster update rate (from 3 to 8 Hz), a reduction in slew between the angle and distance measurements, improvements to system firmware and operating software, a Power Search function, and a configurable output serial stream.

Figure 21. Data collected with the gimbal cart system were positioned with the Leica RTS TPS1200. This device was set up in open area and tracked the system as it was deployed in the trees.

Sky Research conducted a test to compare the dynamic accuracies of the TPS 1100 and 1200. The test consisted of moving the prism by hand up and down two perpendicular lines with locations marked off at 1.5 m intervals. The prism followed the same line for both tests, and the total stations were mounted to the same tripod. There is a 12 cm deviation in the measurements from the TPS 1100 RTS, whereas the

TPS 1200 RTS only has a 3 cm error (Figure 22). The operator's hand motion can account for some of the error in motion while conducting the test. However, the fact cannot be denied that the TPS 1200 RTS has a reduced angle-to-distance slew value, thus eliminating the errors present in the older model.

Power Search is a function that quickly enables the operator to reestablish prism lock after lock is lost. The RTS sprays a vertically wide fan of laser light, rotates about the vertical axis, and looks for return from the prism. Once the prism has been located in the radial plane, the RTS fine-tunes the location by searching the vertical plane. This feature is extremely useful on wooded sites.
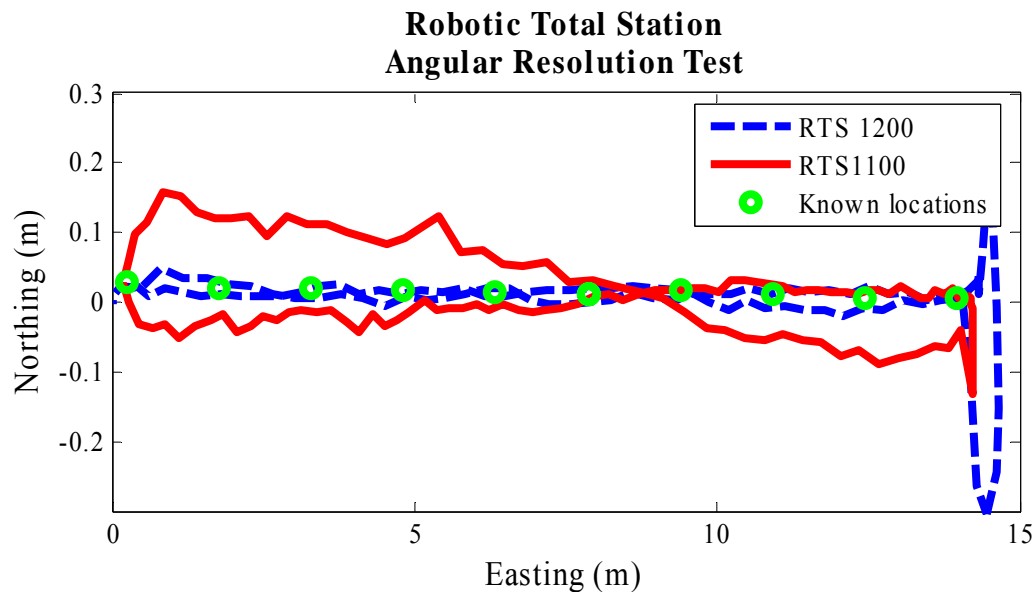
Figure 22. Angular resolution analysis of the TPS 1100 and TPS 1200 robotic total stations. The reduction in angle/distance measurements reduces the error recorded in earlier models.

Additional improvements over the TPS1100 model include improved reliability of the TPS 1200 operating system and underlying firmware. A new graphical user interface (GUI) improves configuration and setup time. A customizable serial output allows the operator to control the type of data the RTS is writing to the serial port. The new remote handheld unit is larger than the pervious versions but the alphanumeric keyboard makes data entry very simple. In addition, the hand-held unit's screen is touch-screen enabled and has on-screen mapping capabilities (Figure 23).
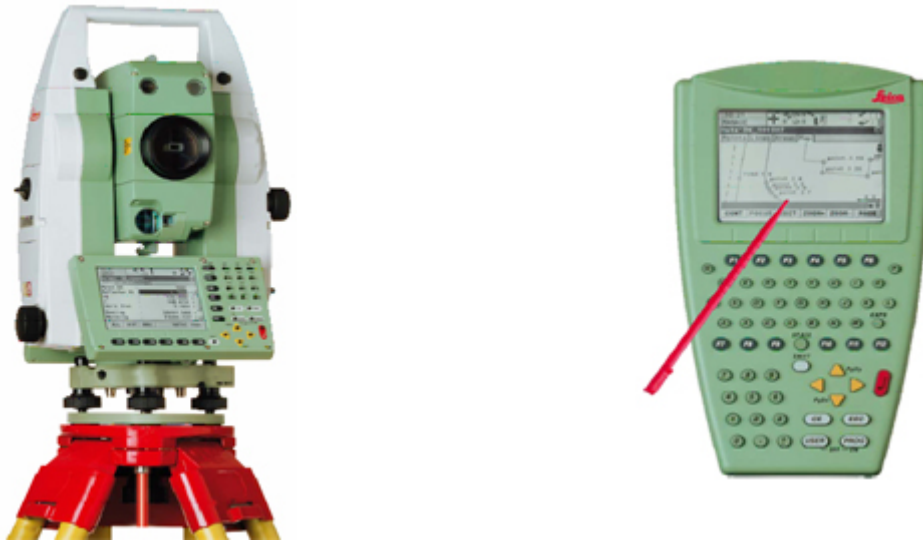
Figure 23.   The Leica TPS 1200 (left) and remote controller unit (right). The remote controller unit can be controlled using a stylus.

The serial output is only configured to one baud setting; unless the device receiving the data stream can accept the baud rate, real-time data streaming will not be possible. Sky Research recognized this problem and quickly developed a Pocket PC application that reads the streaming data at one baud rate and changes the rate so the stream can be accepted by other devices (e.g. HIP). In addition to changing the baud rate, the Pocket PC application also converted the native RTS data stream to a NMEA GGA stream; "pseudo-NMEA" is the name of the stream. The pseudo-NMEA stream allows many devices to accept RTS data as if it were a GPS device.

The RTS prism was mounted directly above the center of the EM61 coils. Two different prism-mounting strategies were used. First, a short pole was established that placed the prism approximately 20 cm above the top EM61 coil. The short-pole has the advantage of creating a smaller lever-arm on the gimbaled EM coils, limiting the sway of System 2. For System 1, without the gimbal, the short pole minimizes the geometrical error introduced into the XY coordinates of the data due to system tilting. The short-pole has the disadvantage of limiting line-of-sight needed by the laser, due to operator obstruction. As such, the short-pole option was used only when a "broadside" survey was possible, where the back-and-forth survey lines did not place the operator in an obstructing position.

A long-pole configuration was also used, where the prism height was established above the operators head, thus avoiding line-of-sight issues.   This configuration is less desirable, as it exacerbates the

pendulum motion of the gimbaled EM coils and creates larger geometrical errors associated with the non-gimbal configuration.

4.5.   Data Acquisition System (DAS)

For the tests conducted to evaluate the gimbal cart system, Sky Research used a custom-built DAS which uses Bluetooth technology to wirelessly stream data from instruments to a tablet PC for recording and processing. The DAS recorded the EM61 MKII signals and TPS1200 RTS positional data.

In 2005, improvements were made to the DAS to improve the flow of information from multiple sensors. These improvements relate to the following data acquisition and management functions: time stamping accuracy, RTS position measurements relative to the IMU orientation, and data management system.

Because of the importance of accurate time stamping of incoming data to DAS performance, DAS improvements focused on utilizing computer operating system functions to increase the time resolution during data stamping. The first avenue explored for increasing DAS performance in this respect was an investigation of the **Read Time-Stamp Counter** (RDTSC) functionality. The RDTSC provides a set of instructions to allow programmers to read the number of CPU cycles on a Pentium® computer that pass from the last RDTSC query call at a resolution of 10 milliseconds. However, it was discovered that Pentium® Mobility chips have variable CPU cycles to reduce power consumption; therefore, a second approach to improving time stamping capabilities was investigated. The second avenue investigated to improve time stamping involved the QueryPerformanceCounter, a high-resolution performance counter provided by Microsoft for their Windows® operating system. The 10 ms heartbeat of the operating system, when polled correctly through the QueryPerformanceCounter function, provides an accurate time stamp for the sample rates and survey speeds used during data collection.   Therefore, the QueryPerformanceCounter was incorporated into the functionality of the DAS before data collection was conducted.

Another improvement to the DAS was the implementation of a standardization test focused at determining the measurement latencies between the RTS positions and the Crossbow IMU orientation measurements. A wizard interface prompts the operator to start the test and plots the results to a window for operator to QC. When the operator accepts the result, the DAS writes the result to an XML file. At the end of the survey, the DAS loads the XML file to the database storing the values for use in subsequent data processing.

In addition to the DAS improvements, the Geophysical Data Center (GDC) relational database that stores, manages, and archives geophysical data for this project was modified. The GDC was updated to improve the system's capabilities for importing, storing, and exporting the new orientation metadata. These improvements required modification of the GDC schema and the data reporting and access tools.

5. DATA COLLECTION SURVEYS AND RESULTS

After the construction of the gimbaled cart system, a number of controlled and "real-world" tests were performed from 2004 to 2006 to measure the effectiveness of the design. These tests varied from controlled conditions to less controlled conditions, deployment to a live site, and a test site.

5.1. 2004 Tests

Controlled tests were conducted in 2004 and included tests conducted on a level parking lot, relatively flat test plot, and an inclined and rutted test plot. Data collection and results from each survey are documented in the following sub-sections.

5.1.1. Parking Lot Test

The first of the series of gimbaled cart tests was conducted on a level parking lot in 2004. The parking lot test provided a clean, level, and easily controllable surface to measure the gimbal's response to pitch and roll tilt changes and the EM61's response to these orientations. To measure the roll response, the cart rolled across a 30 m strip of pavement and over four wooden ramps spaced 6-m apart. To measure the pitch response, the cart rolled across the same strip of pavement and tilted a set number of degrees. Copper rings measuring 0.10 m (4-in) in diameter acted as anomalies and were place at set intervals along the survey line (Figure 24).

Figure 24.   0.10 m wire loops used during the testing.

The parking lot test consisted of six separate tests with each test containing three runs. The tests conducted were two background surveys (starting and ending), two roll surveys (stiff and gimbaled), and two pitch surveys (stiff and gimbaled). The runs provided a measure of the repeatability of the system and the tests. A back and forth survey is considered one run. The survey strip measured 30-m in length with the wire loops positioned at 6-m intervals with one loop stationed at the midpoint.

The roll test consisted of using a series of alternating wooden ramps spaced 6 m apart to roll the cart a fixed number of positive and negative degrees (Figure 25). Ramps constructed from 0.10 ×0.15 ×3 m wooden posts with a bevel cut at each end facilitated the rolling motion. Ramps were positioned adjacent to loops at (0, 6), (0, 12), (0, 18), and (0, 24). The wire loop at (0, 15) did not have an associated ramp; this position acted as a standard for the test. Repeating the test three times provided a measure of the consistency and repeatability of the system. Gimbaled and stiff modes were the two configurations tested, and pinning the gimbal arms maintained the locked position for the stiff mode survey. Using the same platform prevented erroneous readings from height inconsistencies between different platforms.

Figure 25. Gimbaled cart during the roll test. The unit was moved down a pre-defined line over standardized target. Ramps were constructed that tilted the system during deployment.

The pitch test was conducted in the same matter as the roll test without the use of ramps. Controlling the pitch angle was performed less scientifically; points on the operator's body were used as controls for the pitching angle (Figure 26). Performance of the pitching motion occurred at positions (0, 6), (0, 12), (0, 18), and (0, 24), whereas a level data collection happened over loop (0, 15) for the same reasons as the roll test. The pitch test included gimbaled and stiff modes.

Figure 26. Gimbaled cart during the pitch test. During deployment the system was pitched forward and back to simulate the typical motion of the device during actual surveys.

The initial testing of the gimbaled cart provided insight into the performance of the gimbal arms and their ability to compensate for orientation obstacles. The gimbaled cart performed well during the tests and recorded spatially accurate positions without the use of post processed IMU corrected positions. However, the gimbaled cart does not mitigate the elevations changes relative to orientation changes as we had hoped.

The purpose of the roll test was to verify that the IMU was functioning properly and to measure the gimbaled cart responses to changes in roll orientations. Positions from the stiff cart were post-processed corrected using the IMU and sensor geometry. Post processing positions with IMU data works well in correcting the positions of the data (Figure 27). The gimbaled cart data requires no such correction. The IMU data needed additional processing to remove the noisy outliers. An example of the types of outliers present in the data are shown in Figure 27.
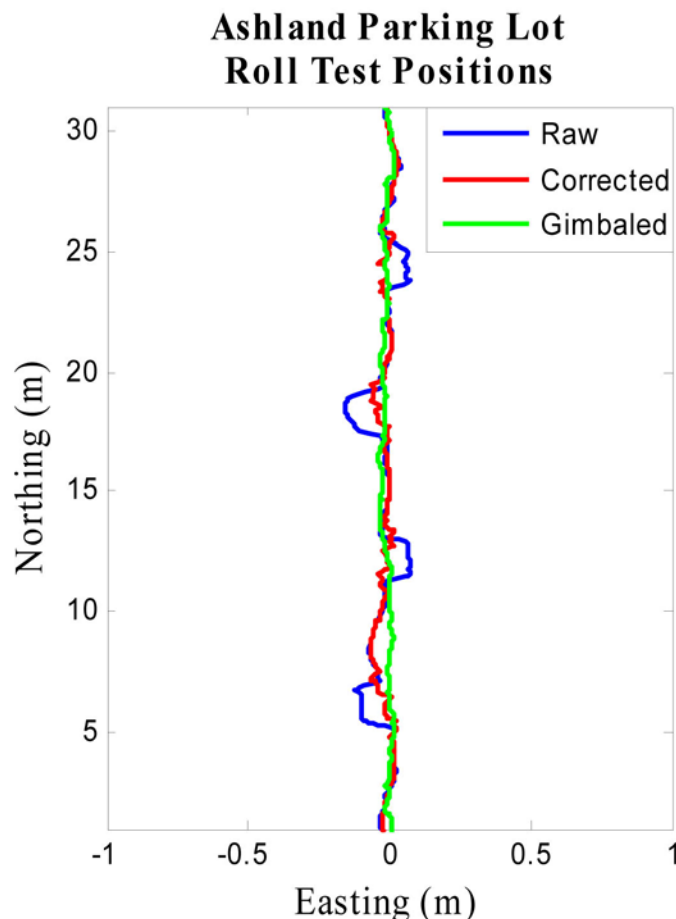
Figure 27. Results from the roll test performed in Ashland. The gimbaled system has much better positioning than the stiff cart and the stiff cart with IMU corrections applied.

Comparing the recorded positions of the stiff cart and gimbaled cart, the gimbaled cart simply outperforms the stiff version. The same cannot be said for the anomaly amplitude response; the two systems performed equally. The coil's center moved vertically to changes in pitch and roll. As described in Section 2 of this report, changes in sensor elevation have the largest effect on measured amplitude response relative to changes in roll, pitch, and yaw. Figure 28 shows a plot of the recorded voltages from time gate 3 (660 μs) of the EM61 MK2; diamonds represent the flat survey with no ramps or pitching motion, squares represent the stiff survey, and the circles represent the gimbaled cart values. At position (0, 0) and (0, 30), the amplitude readings cluster around each other. One-inch trailer hitch balls used at these positions acted as control measures. For the other positions, the sensor response for the stiff and gimbaled carts cluster around each other, and the flat survey results are considerably higher. The change in amplitudes between the flat survey and tilted surveys is caused by the elevation change of the coil's center location as it ramped or tilted.
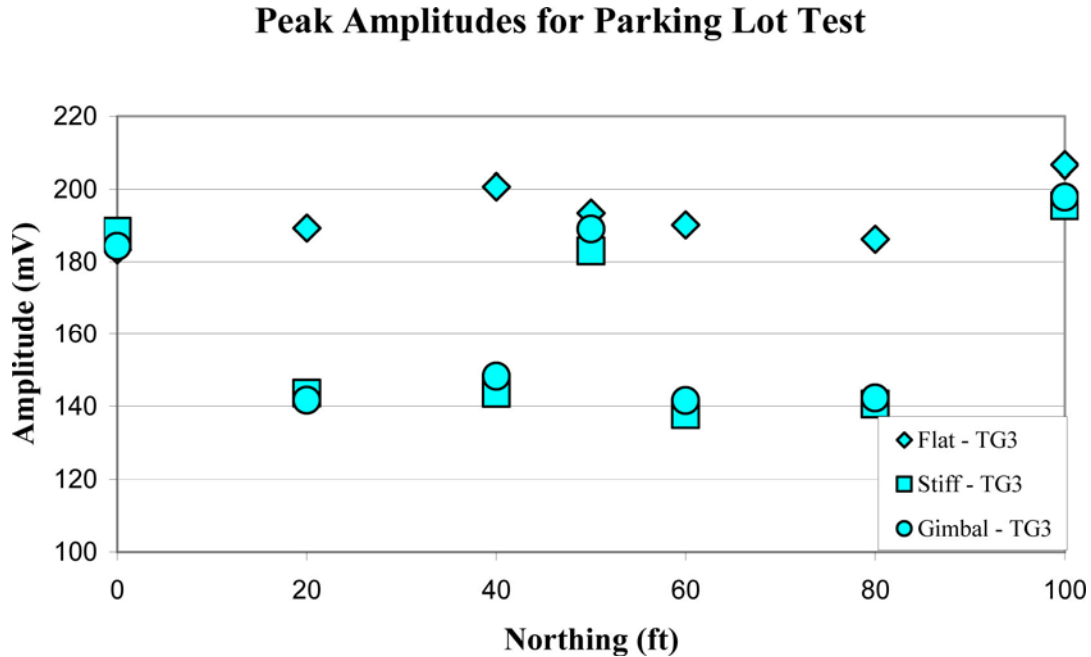
Figure 28. Peak amplitude response over loops during the roll test. The amplitudes displayed are from time gate 3 (660μs). This shows that the elevation effects have not been reduced by the gimbaled system.

The purpose of the pitch test was to measure the gimbaled cart response to changes in pitch orientations. As is shown in Figure 29, positions from the stiff cart remained unprocessed with IMU data; no significant conclusion would be drawn from further processing. Though not shown, the same amplitude analysis as conducted for the roll test yielded the same conclusions. Amplitude changes were less significant in this test because the lever arm acting on the pitch gimbal yoke is smaller than the lever arm for roll yoke.
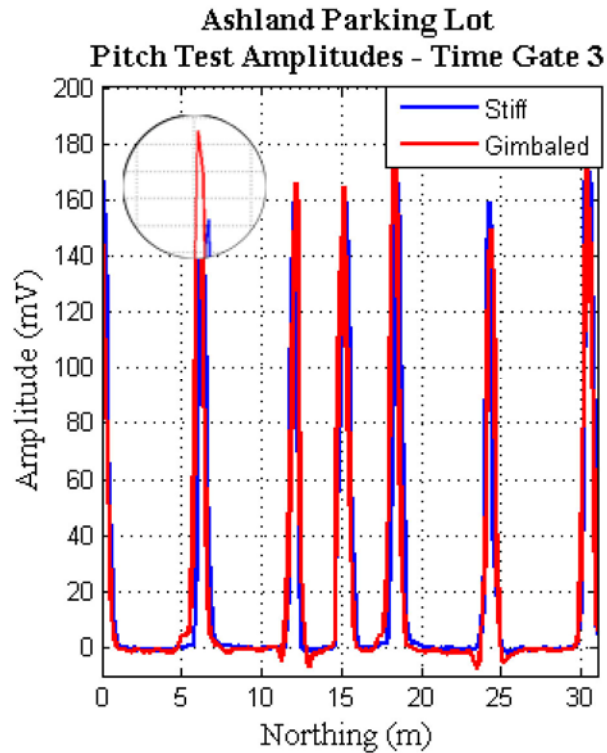
Figure 29. Amplitude and positions results from the pitch test performed at the Ashland Airport. The pitching effect has an effect in both position and response amplitude.

5.1.2.   Ashland Test Plot

The first field test of the gimbaled cart was conducted at the test plot located at the Sky Research facility in Ashland, Oregon, in 2004. The objective of the Ashland test plot test was to test the effectiveness of the gimbal cart in countering the orientation-induced sensor noise. The Ashland test plot is a 60 m × 10 m parcel with 40 cells containing 155 mm projectiles to small frag. Stiff and gimbaled data were collected over the site utilizing the same cart platform. Stiff mode pinned the gimbals so they were locked in the neutral position. The burial process created bumps, ruts, and craters; these features helped to assess data quality and test the dynamic response and damping of the gimbal arms.

A visual comparison of the gimbal-augmented cart data shows small increases in the data quality over the stiff cart data (Foley, 2004). Noises induced from the motion of the cart platform over the physical features of the site were diminished between the two systems. The reduction in noise increased some anomaly amplitudes and reduced amplitudes in others. In addition, positional error associated with orientation can be significantly reduced using the gimbaled cart system. During the Ashland parking lot tests, 15 and 28 percent of the data had positional errors greater than 4 cm for the pitch and roll

orientations, respectively. When using the gimbaled cart, the errors reduce to < 1 and 2 percent for roll and pitch, respectively (Figures 30 and 31). These represent quite significant improvements in positional data quality. This improvement helps detection and provides crisper data for inversion-driven discrimination processes.
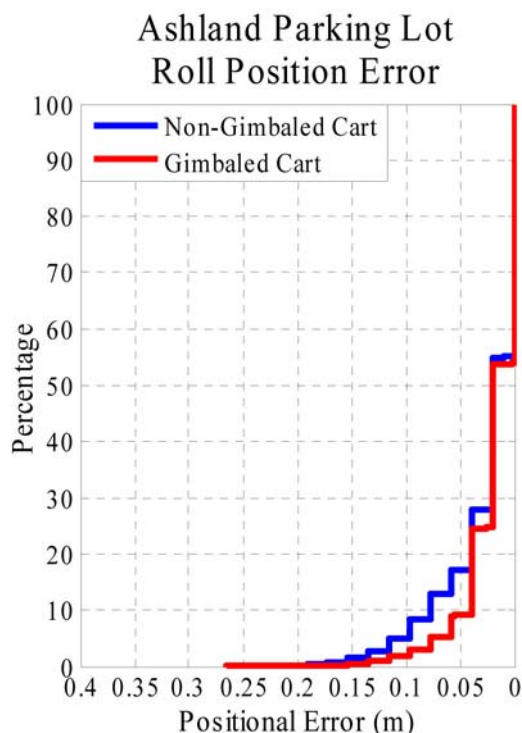
Figure 30. This cumulative error distribution plot displays the amount of error associated to position due to the influence of roll angles. The blue line indicates the stiff or non-gimbaled cart, whereas the red line indicates the gimbaled cart.

The gimbaled cart can minimize the effect of pitch and roll events, but the associated changes in sensor elevation are not avoidable (Figure 32). When a roll event occurs, the sensor changes its height above the ground. The change in height is

$$\Delta z = \frac{x_{wheel} \sin \theta}{2},$$

where Δz is the change in sensor elevation, x_{wheel} is the wheel track distance and θ is the roll angle. Using the RTS as the position-measuring instrument, we are able to measure these small changes in elevation.

The use of the low metal IMU prototype proved acceptable under the controlled conditions exhibited during the parking lot tests.
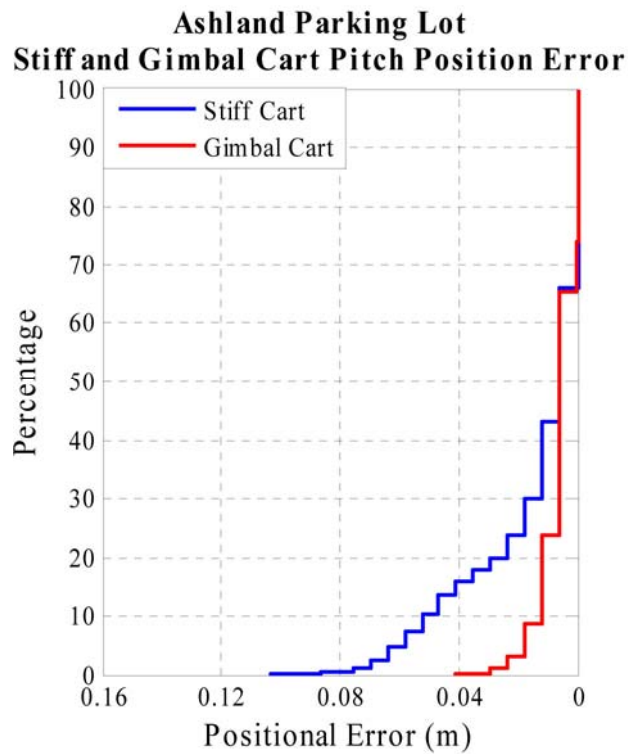
Figure 31. This cumulative error distribution plot displays the amount of error associated to position due to the influence of roll angles. The blue line indicates the stiff or non-gimbaled cart, whereas the red line indicates the gimbaled cart.
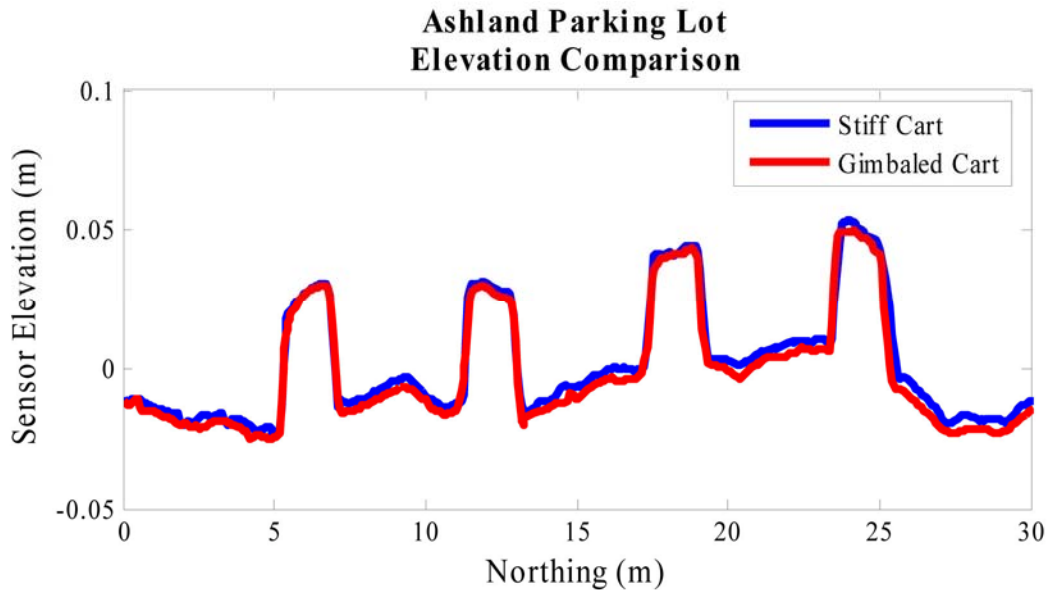
Figure 32. Sensor elevation comparison plot between the stiff and gimbaled systems. The elevation change is consistent between both carts because the gimbaled system does not account for elevation changes.

5.1.3.   Former Lowry Bombing & Gunnery Range Test Plot

As part of the on-going surveying conducted by Sky Research at FLBGR in Colorado, stiff and gimbaled surveys were conducted over the geophysical prove-out (GPO) site located adjacent to the Jeep Demo Range (JDR) and the Aurora Reservoir and Recreation Area in 2004 (Figure 33). The GPO site is comprised of 70 6 × 6 m cells with a region 60 × 24 m of targets randomly buried. Buried items range in size from 50 lb K941 shipping containers to M50 fuzes. The elevation of the site increases in a gentle fashion from south to north, and the site was surveyed in a north-south direction. Surveying up and down hill allowed the pitch gimbal arm to compensate for the slope of the hill.

Figure 33.   The gimbaled cart system was deployed over a test plot at the FLBGR GPO site.

A comparative analysis performed on the FLBGR GPO data revealed some promising results (Foley, 2004). First, upon initial review, the amount of background noise decreased. The site had recently been excavated to allow the placement of other items for the GPO. Many of the bumps and ruts still existed from the lack of site activity. The gimbaled system smoothed the noise from the ruts as seen in previous surveys. Second, smaller-sized targets such as in cells 57, 58 and 67, appeared more prevalent as can be seen in Figures 34 and 35. Data collected by the gimbaled cart has a higher signal-to-noise ratio, which improves target detection and ultimately target discrimination. Finally, the spatial accuracy of the data improves with the use of the gimbaled system on a hillside because there is no constant sensor offset typically seen in stiff cart surveys.
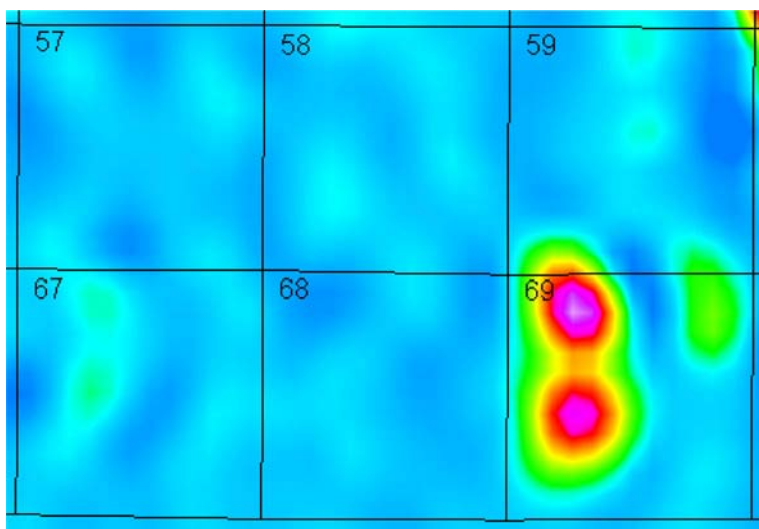
Figure 34.   A snippet of standard EM61 MK2 cart data from FLBGR GPO site, each cell is 6- × 6-m. These data were collected in an East/West directions.
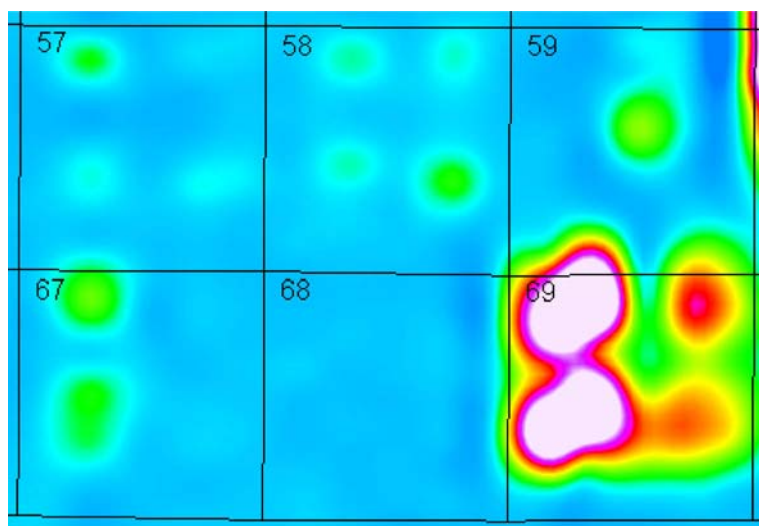
Figure 35.   A snippet of gimbaled EM61 MK2 cart data from FLBGR GPO site, each cell is 6- × 6-m. These data were collected in a North/South direction.

5.1.4.   Lake Success Business Park Live Site

In 2004, the system was also tested at DuPont's Lake Success Business Park (LSBP) in Connecticut as part of the Environmental Security Technology Certification Program (ESTCP) live-site demonstration project.   The LSBP site is a 422-acre underdeveloped industrial property located in Bridgeport and Stratford, Connecticut. The site, formerly know as Remington Park or Remington Woods, was renamed

Lake Success Business Park and is presently undergoing an aggressive remediation program. The 70-acre parcel of land is contingent with the LSBP facility but is located in Stratford instead of Bridgeport. DuPont, the current site owner, has received approval from the regulatory agencies to proceed with redevelopment of this parcel. During remediation of areas of environmental concern at other locations on LSBP, both small and large caliber munitions were found in places where they were not expected. As an added precaution prior to releasing this portion of the site for redevelopment, DuPont wanted to conduct a UXO survey utilizing current state-of-the-art detection and mapping technologies and field verification to determine if UXO are present.

The data collection plan associated with this project for the LSBP geophysical surveys included surveys conducted using EM61 sensors over areas with seeded UXO targets and unknown targets where excavations will take place after the survey is completed. Sky Research deployed EM61 systems over approximately 3 acres of the LSBP site. The EM61 was deployed using two separate pushcart form-factors; one using the standard wheel/coil configuration provided by Geonics (Figure 36), and one with the coils mounted in a self-righting gimbal configuration (Figure 37). Both EM configurations were deployed in both push and pull modes as conditions dictated. The magnetic and EM data were position-stamped with data collected from the Leica 1200 RTS. The orientation of the sensors during collection was measured using a low-metal IMU providing pitch, roll, and 3-axis acceleration measurements. Additionally, a GPS was used, as appropriate, to collect position data concurrent with the RTS data for subsequent analysis.
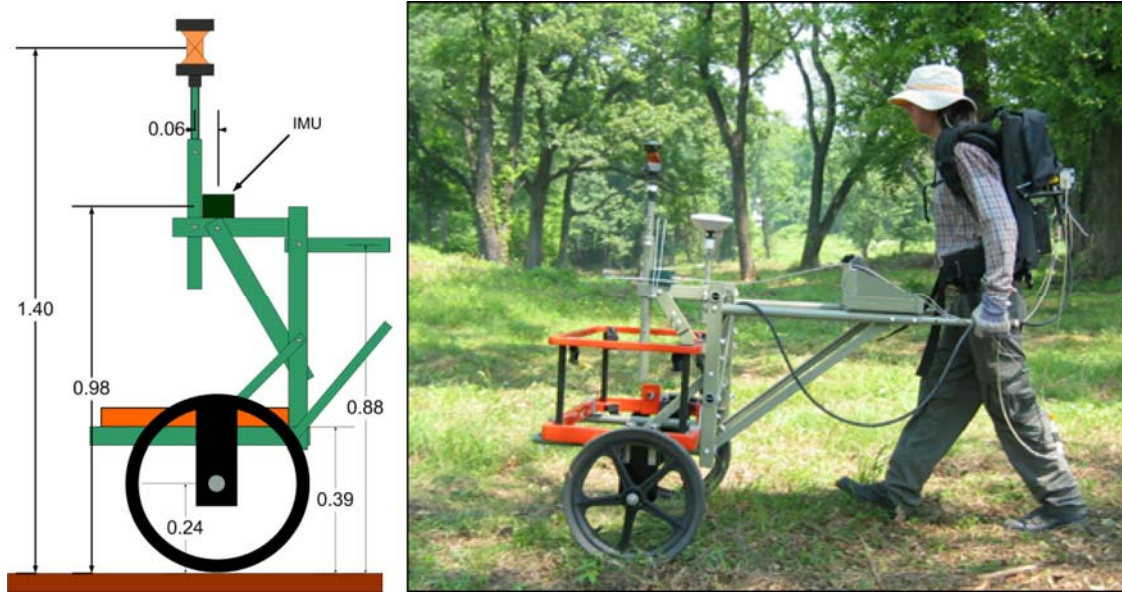
Figure 36. System 1 included the Leica RTS TPS1200 and GPS positioning systems, the IMU orientation sensor, and the EM61 sensor deployed over the site using the non-gimbal cart system.

Figure 37. Gimbaled cart keeps the sensor level while surveying the Lake Success Business Park calibration site. The gimbal arms help to stabilize the EM61 sensor in uneven terrain.

Several issues regarding field conditions at the LSBP site made the collection of data difficult, reducing the usefulness of the results to the SERDP 1310 project. These conditions affected the quality of the data

collected as well as the amount of area covered during the survey, thus compromising the ESTCP component of the deployment. First, the site had insufficient vegetation removal performed prior to the geophysical survey, limiting deployment of the system and causing problems with the laser positioning system. Second, large and deep ruts (up to 50 cm wide and 40 cm deep) were created over large parts of the site by heavy machinery that was used to clear brush, hindering cart-based deployment.

A standard EM survey was conducted using the EM61 sensor deployed over the site using the non-gimbal cart system, Leica TPS1200 and GPS positioning systems, and the prototype low metal IMU orientation sensor (Figure 36). In open areas where an unobstructed view of the sky was present, real-time kinematic (RTK) GPS data were collected to supplement the RTS positioning data. While it was anticipated that between one and two areas would have coverage, the GPS proved useful only in very limited areas and was not utilized further by the SERDP 1310 project in Year 2. In wooded areas, the RTS base-station was set up in strategic locations to optimize the use of the RTS prism tracking features that allow tracking in areas where obstructions are present (i.e. trees).

The area was covered by pushing or pulling the system back-and-forth over the site. To meet data density requirements, a line spacing of approximately 30 cm (1 foot) was used whenever possible. This tight line spacing was generally accomplished through use of marking flags planted behind the cart by a crewmember as the survey proceeded. Coverage of the site was limited to areas clean and safe enough to conduct geophysical surveying.

System 2 (Figure 37) included the RTS positioning systems, the IMU orientation sensor, and the EM61 sensor. This equipment was mounted on the mechanical gimbal that allowed for even deployment of the equipment over the terrain. The area surveyed with this system was selected to include areas where System 1 was deployed, and where the gimbaled cart could traverse unimpeded and include the calibration area and a section in the northern open area. RTS technology tracked the system during surveying, and GPS was not utilized. Results show that the gimbaled cart position data surpassed the quality from the standard surveys. With a shorter prism pole and the gimbal arms countering the bumps and ruts, position data had fewer zigs and zags, thus mitigating positional errors and improving geophysical data quality (Foley, 2004).

The deployment of the EM sensors in the standard mode generates a high degree of system pitch and roll that adds to geophysical data noise and positional inaccuracies, which are mitigated by the gimbal system. At LSBP, 40 percent of the data had roll-induced positional errors of greater than 10 cm, and nearly 10

percent of that data had errors over 20 cm when the stiff cart was used. When using the gimbaled cart, only 4 percent of the data had positional errors that exceeded 5 cm. Figures 38 – 41 show the results from positional analysis performed on data from the LSBP live site test. This improvement in the spatial registration of geophysical data supports the data objectives necessary for applied discrimination activities.

Correcting the positions using an IMU proved acceptable under certain conditions. Applying corrections to the parking lot test data proved useful, but when the corrections were used on the LBSP live site, undesirable position artifacts were created in the positions records. The low-metal IMU, which was used for both tests, appears to generate accurate pitches and roll angles when the system is not experiencing high angular accelerations. During times of high accelerations, the IMU data requires the During times of high accelerations, the IMU data requires the application of a significant filter to smooth the readings (Figure 42).
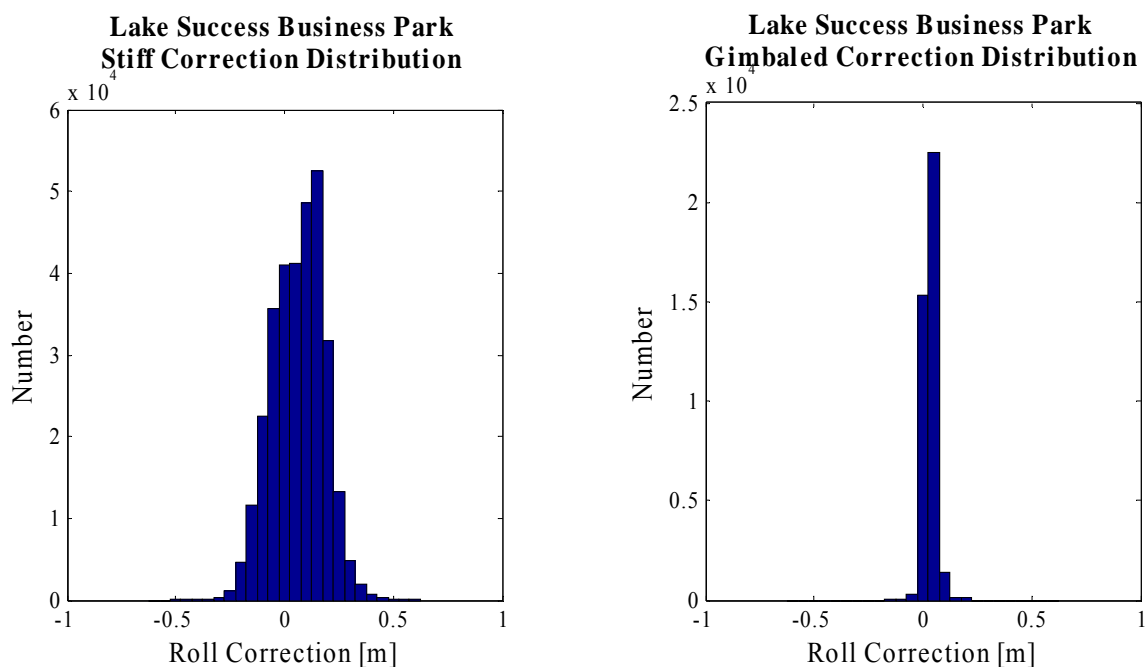
Figure 38. Histogram XY of positional errors associated with the tilt of the EM systems. Left: standard EM61 deployment causes significant sensor errors due to the tilt of the sensors. Right: the gimbal unit removes most of the positional errors by minimizing sensor tilt.
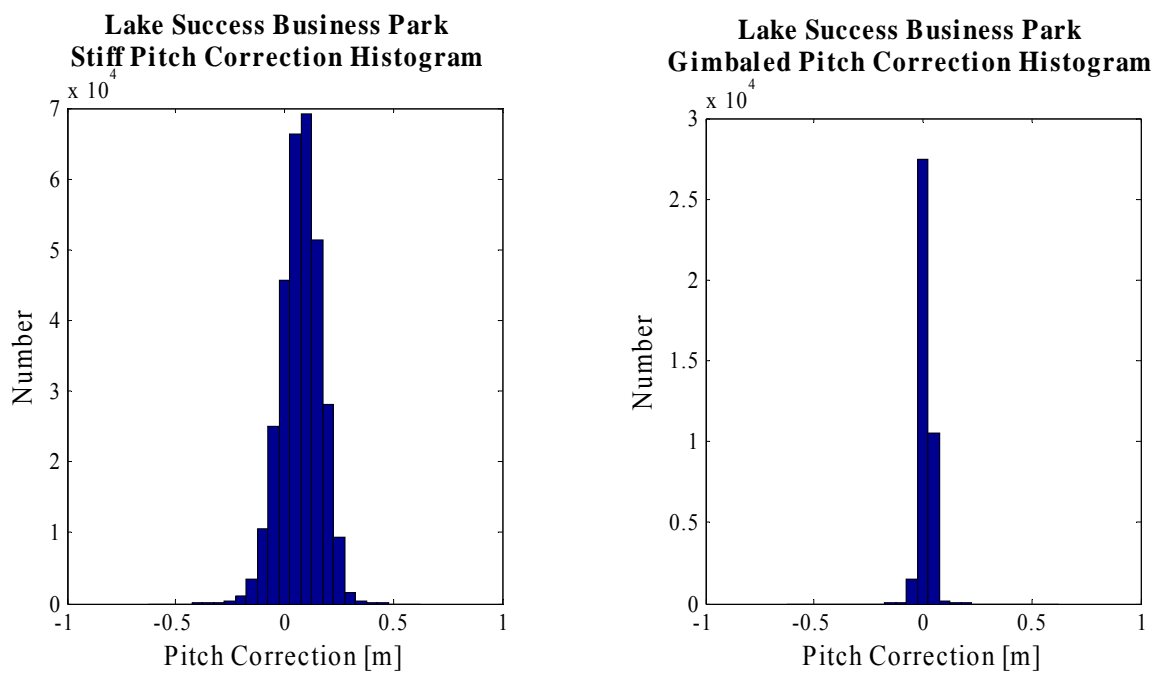
Figure 39. Histogram XY of positional errors associated with the pitch tilt of the EM systems. Left: standard EM61 deployment causes significant sensor errors due to the tilt of the sensors. Right: the gimbal unit removes most of the positional errors by minimizing sensor pitch.
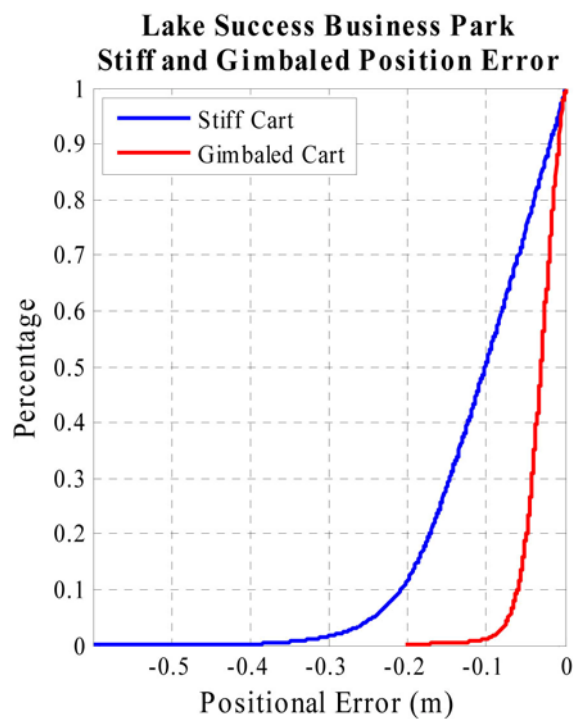
Figure 40. Cumulative distribution plots of positional errors associated with the roll tilt of the EM systems for standard EM61 stiff and gimbal system.
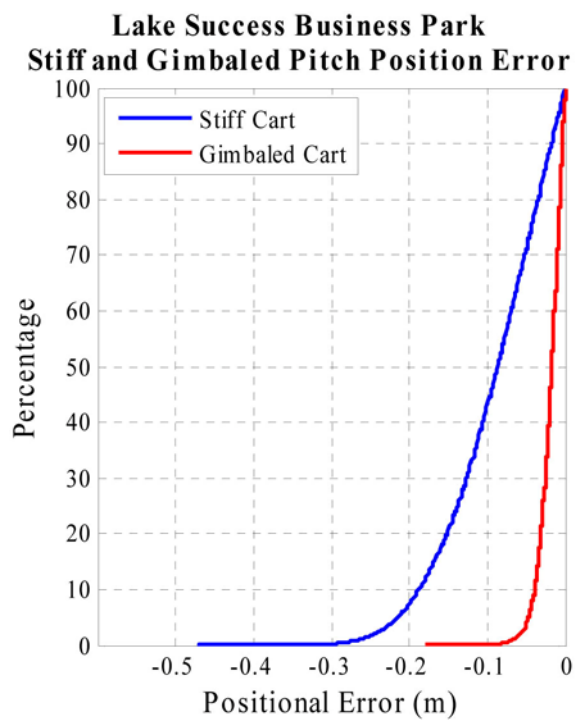
Figure 41. Cumulative distribution plots of positional errors associated with the pitch tilt of the EM systems for standard EM61 stiff and gimbal system.
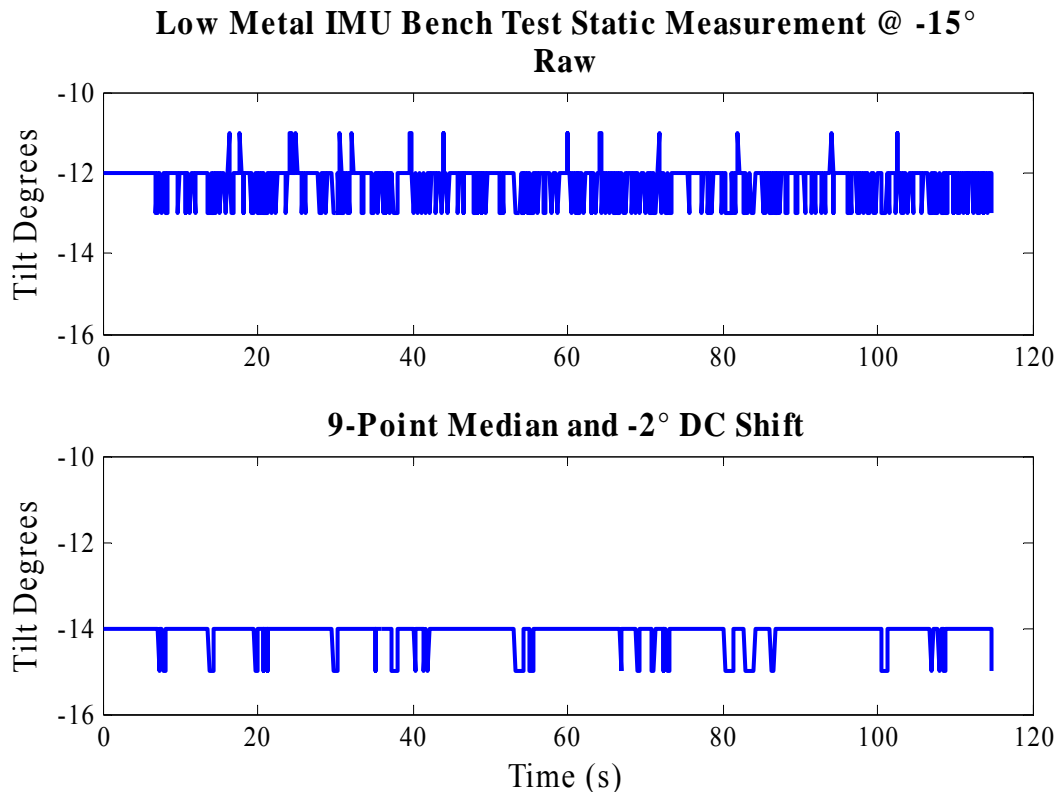
Figure 42. The static measurement of the low metal IMU at 15°. The data required filtering using a 9-point median filter and a static -2° DC shift to smooth the response.

5.2.   2005 Tests

5.2.1.   Ashland Test Plot

As part of Year 3 system testing, the ground surface around certain buried targets at the Ashland Test Plot was modified with ruts, small ramps, and stick mats to mimic field conditions found on typical live sites. These test plot features introduced additional positional errors to the collected EM data. The objective of subsequent field tests was to quantify the ability of gimbaled cart system to mitigate the effects of these features. Analysis of the results were conducted based on the modeling developed as part of this project and documented in Section 6 of this report.

Modification of the test plot was comprised of creation of ruts 15 cm deep and 30 to 45 cm long adjacent to targets in the test plot (Figure 43). While ruts can be much deeper than 15 cm, this depth prevented the gimbaled cart from bottoming out while traversing the hole. To simulate the conditions at wooded sites where deadfall typically litters the ground, 9 ramps were placed adjacent to 9 emplaced subsurface targets. Ramps were constructed 10 to 15 cm in height and 30 to 45 cm in length. Last, in order to

simulate high frequency micro-topographic variations, a set of stick mats were developed (Figure 43). Stick mats were 1-meter square wooden sheets with variable-diameter PVC piping cut in half and securely fastened at different angles. Four mats were placed over four different targets in various orientations.

Figure 43. Ruts and stick mats used to simulate high micro-topographic changes on the Ashland Test Plot.

Baseline data were collected over the Ashland Test Plot before the site was modified using the RTS for positioning. The baseline survey was conducted in both static and dynamic modes. In the static mode, the gimbal cart was locked down and static data collected at 0.5 m intervals, using both the low metal and crossbow IMUs. In dynamic mode, data was collected varying the IMU type and gimbal status (Table 1, datasets 1-4). After site modification, four data sets were collected (Table 1, data sets 5-8; Figure 44).

Figure 44.   2005 data collection at the Ashland Test Plot.

Table 1.   Dynamic Baseline Data Collected at Ashland Test Plot

Data Set	IMU Sample Rate	IMU Type	Gimbal Status	Test Plot Status
1	10 Hz	Low Metal	Locked	Unmodified
2	10 Hz	Low Metal	Free	Unmodified
3	12 Hz	Crossbow	Locked	Unmodified
4	12 Hz	Crossbow	Free	Unmodified
5	10 Hz	Low Metal	Locked	Modified
6	10 Hz	Low Metal	Free	Modified
7	12 Hz	Crossbow	Locked	Modified
8	12 Hz	Crossbow	Free	Modified

AETC processed the data collected for this project at the Ashland Test Plot (Foley, 2005). The tests demonstrated how improvements in sensor positioning and orientation improve the fidelity of target parameters (the βs) estimated by inverting EM61 data collected in field surveys. If the locations $\mathbf{r}_i$ of the sensor readings S_i used to estimate the target parameters are in error, then the model cannot reproduce the data (See Section 6 for discussion on modeling). Furthermore, if the model can reproduce the data, it will do so using incorrect target parameters. Therefore, the dipole fit error was used to evaluate performance. The fit error was calculated from the squared correlation (R^2) between the best model fit and the data.

Statistically speaking, the quantity $1-R^2$ is the portion of the signal variance that is not accounted for by the model, so the fit error is defined as

$$\varepsilon = \sqrt{1 - R^2} \, .$$

$$(7)$$

The major factors limiting performance in the field are positioning errors and background signal variations due to sensor noise and small metal fragments that frequently litter ordnance impact areas. Both of these factors contribute noise to the inversion process. Since the simultaneous equations (Equation 6) are linear in the polarizability elements, errors in estimates of the polarizability matrix will be proportional to the errors in the S_i, (and hence ε) with the constant of proportionality determined by details of the coil sensitivity functions $\mathbf{C}_R$ and $\mathbf{C}_T$.

Figure 45 shows the relationship between errors in target parameter estimates (βs) and the dipole fit error based on Monte-Carlo simulations. The beta error is defined as

$$\beta_{ERR} = \sqrt{\frac{1}{3} \sum_{i=1}^{3} \left(\frac{\beta_i - \beta_{0,i}}{\beta_{0,i}} \right)^2}$$

$$(8)$$

where the β_i are βs calculated using noisy data and $\beta_{0,i}$ are the true βs.
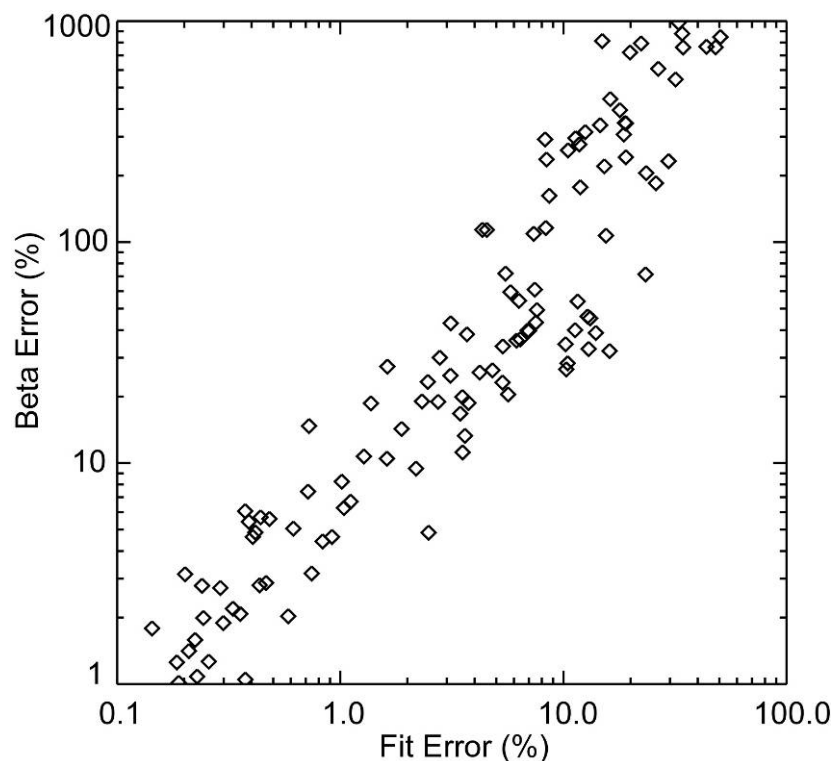
Figure 45.   Beta error vs. Dipole Fit Error from Monte Carlo simulations.

Figure 46 compares fit errors for a standard survey (Test09, rigid cart, no corrections for sensor orientation) with those for a survey conducted using the gimbaled cart with orientation corrections (Test14c). Note that as a practical matter, the yaw correction for the data collected at the Ashland Test Plot does not affect fit quality. Fits were repeated using yaw determined from the recorded (X, Y) track and from the nominal track (constant Y lines); the results showed no difference in the fit error. With the exception of two points, the fits using corrected data from the gimbaled cart showed significant improvement over the standard survey.
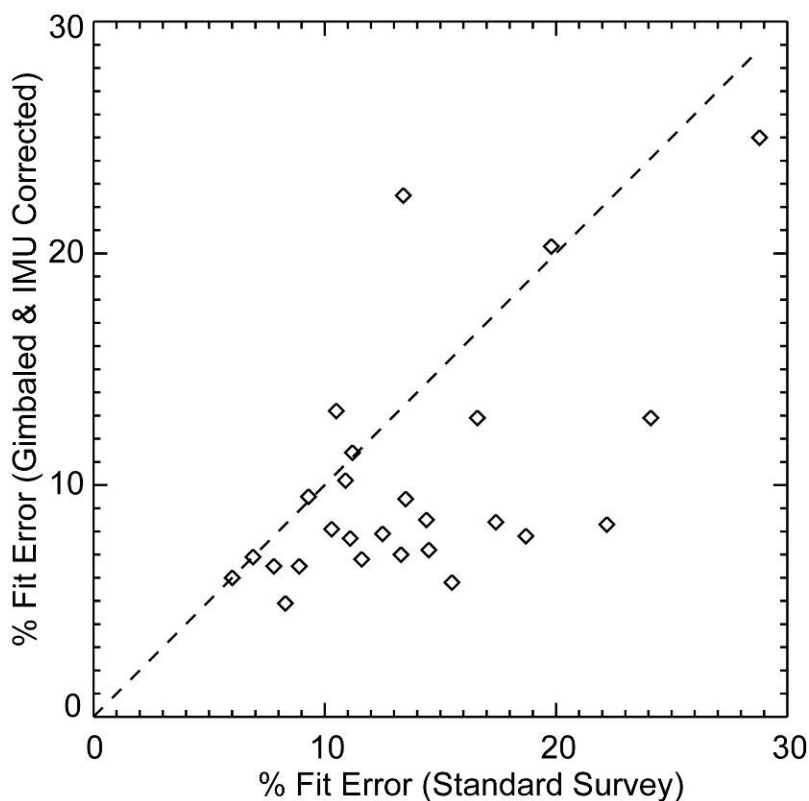
Figure 46.   Comparison of dipole fit errors for standard survey and survey with gimbaled cart.

Fit error vs. target signal to noise ratio (SNR) is shown in Figure 47. SNR (in dB) is defined as

$$SNR = 10\log\left(\frac{\frac{1}{2}S_{max}^2}{\mathrm{var}(N)}\right). \tag{9}$$

where S_{max} is the maximum signal and var(N) is the background noise variance (~4mV^2). The data are for Test 11c (rigid cart with IMU corrections) and Test 14c (gimbals free, IMU corrected). Fit quality generally improved with the gimbaled system. The solid curve in Figure 47 shows the expected behavior if background noise is the factor affecting fit quality.
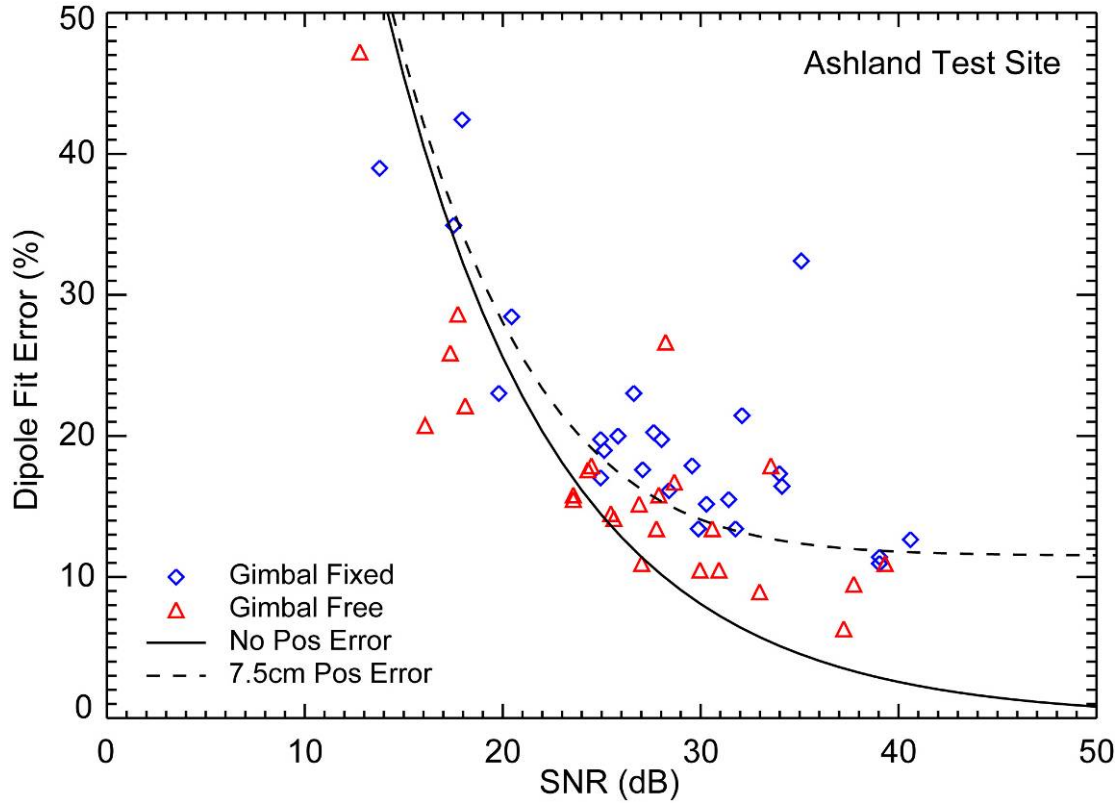
Figure 47. Fit error vs. Signal to Noise Ratio.

In that case, since $1-R^2$ is the portion of the signal variance that is not accounted for by the mode, SNR and fit quality would be related by

$$SNR = -20\log(\varepsilon) + 10\log\left(\frac{\frac{1}{2}S_{max}^2}{\frac{1}{N}\Sigma S_i^2 - \left(\frac{1}{N}\Sigma S_i\right)^2}\right).$$ (10)

The second factor in Equation 10 accounts for the fact that Equation 9 defines SNR in terms of S_{max}, whereas the correlation coefficient is based on the variations about the mean signal level. Empirically, this factor amounts to about 8.2dB.   The dashed curve shows the expected behavior if there are uncorrected position errors in the data.   Since uncorrected sensor location errors are an additional contribution to the noise, the actual signal to noise ratio is less than the apparent SNR from Equation 9. This additional noise can be expressed in terms of the position uncertainty δl and the spatial gradient of the signal ∇S as

$$N_{\delta l}^2 = \overline{(\nabla S)^2 \, \delta \ell^2} \,. \tag{11}$$

The average depth (to top) of the targets in Figure 47 is 44 cm. Using a nominal depth (to target center) of 54 cm, the sensitivity to horizontal sensor location errors is 0.43% of S_{max} per cm of position error. The dashed curve is calculated using this sensitivity and an RMS position error of 7.5 cm. It gives an acceptable representation of the trend in the data at high SNR, falling between the fixed and free gimbal data. With the gimbals fixed, the residual position errors are greater than 7.5 cm RMS, and are less than 7.5 cm RMS when the gimbals are free.

5.2.1. Earth Flux Field Test

In addition to the recorded signal on the EMI sensor caused by the interaction of the EM source and the buried conductive target, the induction data also contain signal components caused by sensor motion through the earth's magnetic field $\mathbf{H}_E$. Maximum flux flows through a loop in a magnetic field when the area of the loop and the direction of the earth's field during deployment will contain a noise term described as:

$$V_N(t) = \mu_0 A H_E \sin(\theta) \frac{d\theta}{dt} \,, \tag{12}$$

where $\theta(t)$ is the angle between the direction of the geomagnetic field and the receive coil axis, and $\mathbf{A}$ is the area of the receive coil. As flux changes with time due to changes in $\theta(t)$, an additional signal is induced in the coil supplemental to the EMI response of the buried target.

Mathematically modeling the response of the EM61-MKII is difficult because the internal gains applied to the readings by the EM61 MkII electronics are unknown. Therefore, Sky Research conducted an empirical test to measure the effect of the ambient field on EM61 readings by mounting an EM61 MkII coil to wooden swing arms (Figure 48). The Crossbow IMU, mounted more than 0.5 m away on one of the swing arms, collected the angular data throughout the arc of the swing (Figure 49).
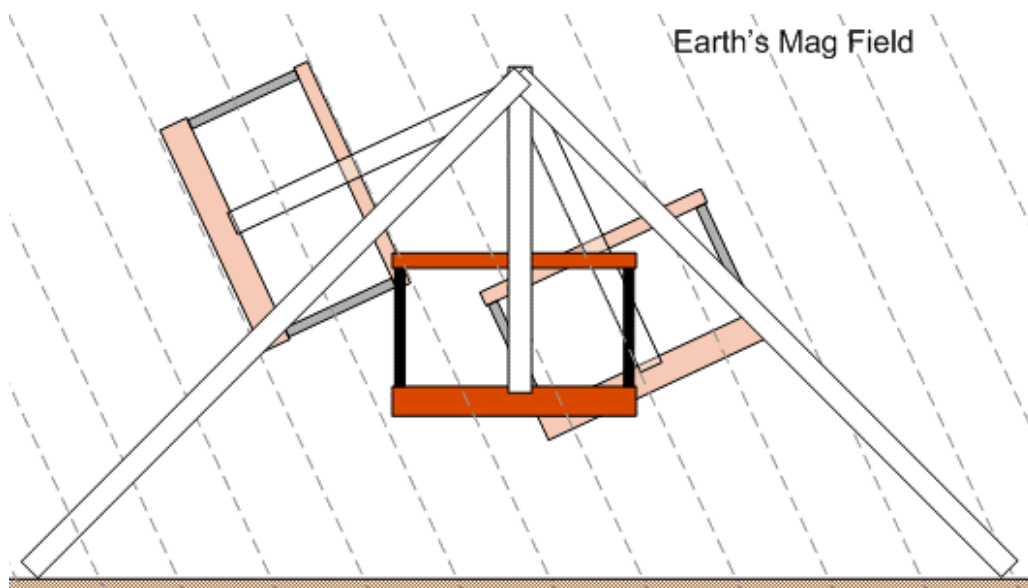
Figure 48.   The swing test was designed to measure the effect of the earth's magnetic field on EM61 readings.
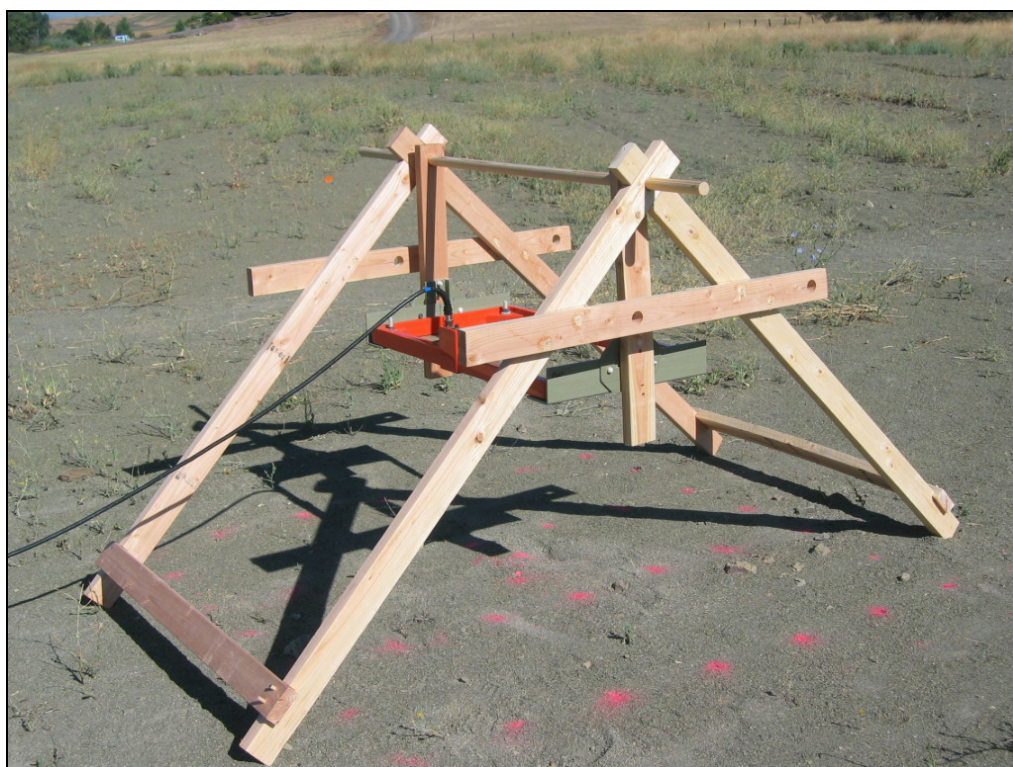
Figure 49.   Swing test platform as constructed and outfitted with the EM61 sensor and Crossbow IMU.

The sensor swung through the field at a period of 1 oscillation per 8-10 seconds and reached an angle of ±60° per oscillation. The IMU collected data at 5 Hz and the EM recorded data at 10 Hz. The EM61-MKII was powered up for 30 minutes prior to data collection to allow the instrument to warm up and stabilize. Sky Research's DAS collected the data streams and time stamped the data.

To analyze the effect of the earth's magnetic field on the EM61 readings, a power spectra analysis was conducted on the EM61 and IMU data collected during the swing test. As shown in Figure 50, the EM61 data do not exhibit significant differences between the static and swinging states of the EM sensor, except for a slightly greater variability that can be accounted for by the sensor motion and the proximity of the operator. The IMU data exhibits greater energy in the frequencies between 0.1 and 0.2 Hz during the swinging test, which relates to the period of the swing's oscillation. In addition, the IMU data exhibits greater energy levels at 0.5, 1.5 and 1.9 Hz during the swing test, which relates to the harmonics of the dominate frequency associated with the swinging motion. From this analysis, it was concluded that the EM61 is not sensitive enough to measure the contribution of the Earth's magnetic field during data collection.
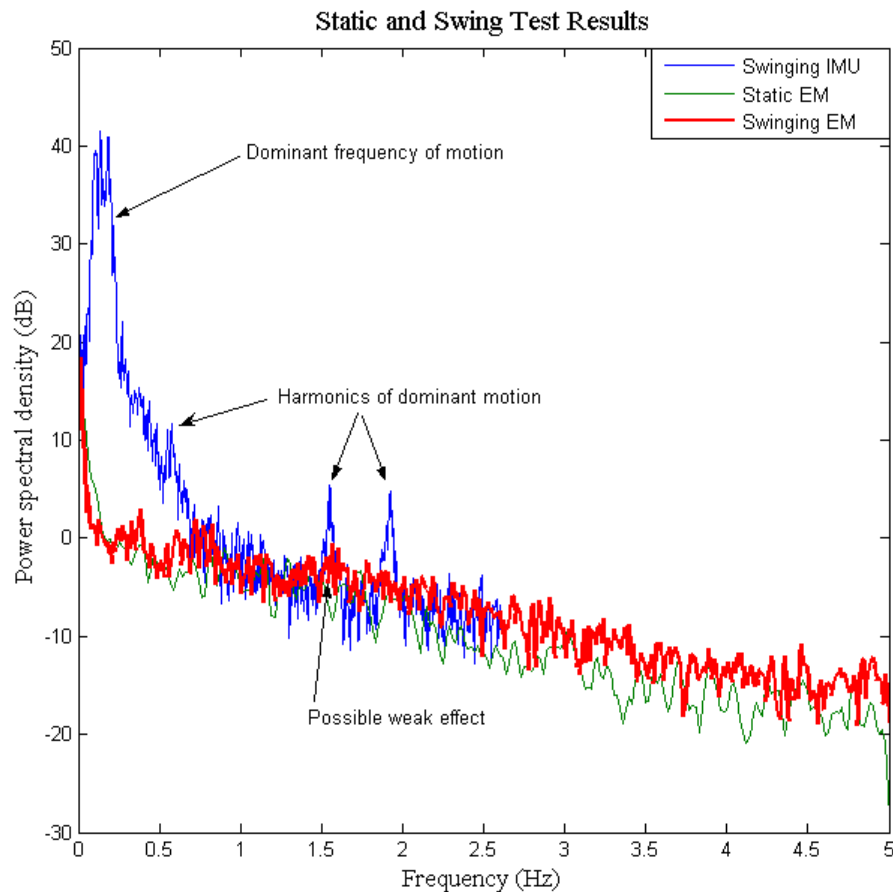
Figure 50. Power spectral analysis results showing the static and swing test results conducted to determine effect of the earth's magnetic field on the EM61 sensor and IMU.

5.3. 2006 Test at Blossom Point, Maryland

The Blossom Point test was conducted to further test and evaluate improvements in the data collection platform developed by this project and sensor positioning information and analysis methods. A significant amount of geophysical data has been collected with other platforms at the Blossom Point Test Facility. The data collected under this plan was analyzed and compared to other relevant data sets for evaluation of the system. In addition, the topography of the test area was modified to simulate realistic survey terrain.

The site was established under ESTCP sponsorship by the NRL at the Army Research Laboratory's Blossom Point research facility in Southern Maryland (Nelson et al., 2000). Targets buried in the test field include inert ordnance, ordnance simulants, test shapes, and various clutter items at a variety of

depths and orientations. The field is aligned North-South and measures 40 m wide by 100 m long. The targets are deployed in a 6 m spacing grid with 61 of the 75 grid positions occupied. The field is level and relatively smooth. On average over the site the RMS pitching and rolling motions of the survey cart were 2.62° and 1.68° respectively.

5.3.1. Data Collection

Data at the Blossom Point test site were collected by Sky Research in June 2006 using the gimbaled EM61 cart (Figure 51). For the Blossom Point test, the RTS positioning system was replaced by either a GPS antenna or a tetrad receiver array for the ArcSecond laser positioning system. The gimbal arrangement reduces sway of the GPS antenna. With the gimbals operating (free), the RMS pitch and roll dropped from 2.62° and 1.68° to 1.32° and 0.95° respectively. With the GPS antenna 1 m above the coil, sway due to this pitching and rolling motion will produce RMS position errors of 4.6 cm and 2.9 cm, respectively when the gimbals are locked. With the gimbals free, the corresponding values are 2.3 cm and 1.7 cm.

Figure 51. ArcSecond positioning system replaced the RTS for the gimbal cart data collection surveys conducted at Blossom Point.

The ArcSecond laser positioning system was originally developed by ArcSecond (now Metris) as "Indoor GPS" capable of achieving 0.1 mm and better precision to perform large-scale measuring and alignment

tasks in aerospace, automotive, and other heavy industrial manufacturing. The system consists of four rotating eye-safe lasers with a range of 50-100 m combined with photo diode laser/infrared detectors capable of producing up to 20 position updates per second with sub-centimeter precision. The component parts of the system are shown in Figure 52a. The laser transmitters rotate at about 40 revolutions per second. Each laser has a unique and constant rotation speed. The photo diode laser detector can therefore identify the source of laser pulses by frequency analysis. Real time processing of pulse series received by the laser detector determines the spatial vector between laser and detector. The horizontal vector angle is derived from the time difference between the rotating laser beam and the zero angle strobe pulse emitted by an array of infrared diodes at the base of the laser head. To measure vertical angle the rotating laser beam is split into 2 symmetrical fans arranged in a vertically oriented "V" shape, as shown in Figure 52b. The time difference between the two consecutive laser pulses received from each leg of the V shape laser fan is a direct measure of vertical angle. By intersecting the vectors measured from at least 2 independent lasers, detector coordinates are computed with sub-centimeter precision at 20 updates per second.

An ArcSecond system for UXO survey applications was developed and demonstrated under ESTCP project MM-0129 (Innovative Navigation Systems to Support Digital Geophysical Mapping). The UXO system uses four rigidly attached light sensors in a tetrahedral configuration (shown in Figure 52a) to measure both the receiver array's position and orientation. In post-processing software, the displacements from the ArcSecond receivers to the EMI sensor are used to calculate the 3D position and orientation of the EMI sensor.

(a)　　　　　　　　　　　　　　　　　(b)
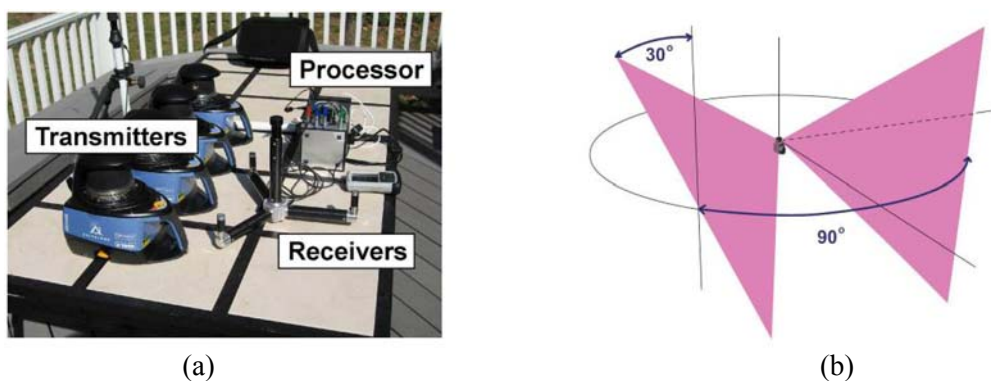
Figure 52.   (a) Component parts of ArcSecond laser positioning system. (b) Transmitter fan beam.

The ArcSecond positioning system was tested as part of SERDP project MM-1381 (Handheld UXO Sensor Improvements to Facilitate UXO/Clutter Discrimination). When stationary, the RMS noise in the receiver positions is on the order of 0.2 mm. The position accuracy of the ArcSecond system when

moving was tested by comparing the reported trajectory of the sensor with the trajectory as determined from video recordings of the motion in a horizontal plane at speeds of about 30-60 cm/sec. Across the central region of the video data, the standard deviations in the differences between positions determined by the ArcSecond system and video recording were between 2 and 4 mm. The standard deviation in Z was 2.6 mm. Analysis of dipole model fits to data collected over various targets using an EM61-HH with ArcSecond positioning confirmed that the positioning accuracy of the system was of order 3 mm (Barrow et al, 2006).

Four survey modes were employed in collecting data at the site: (a) gimbals fixed with Differential GPS (DGPS)/RTK positioning ("Standard" survey), (b) gimbals free with DGPS/RTK positioning, (c) gimbals fixed with ArcSecond positioning, and (d) gimbals free with ArcSecond positioning. With the gimbals fixed, the cart behaves more or less like a standard EM61 survey.

5.3.2.   Processing and Analysis of Blossom Point Survey Data

Figure 53 is an EM61 survey map of the Blossom Point test site. The map shows data for the first time gate collected with the gimbaled push-cart system using GPS positioning. Anomalies corresponding to 60
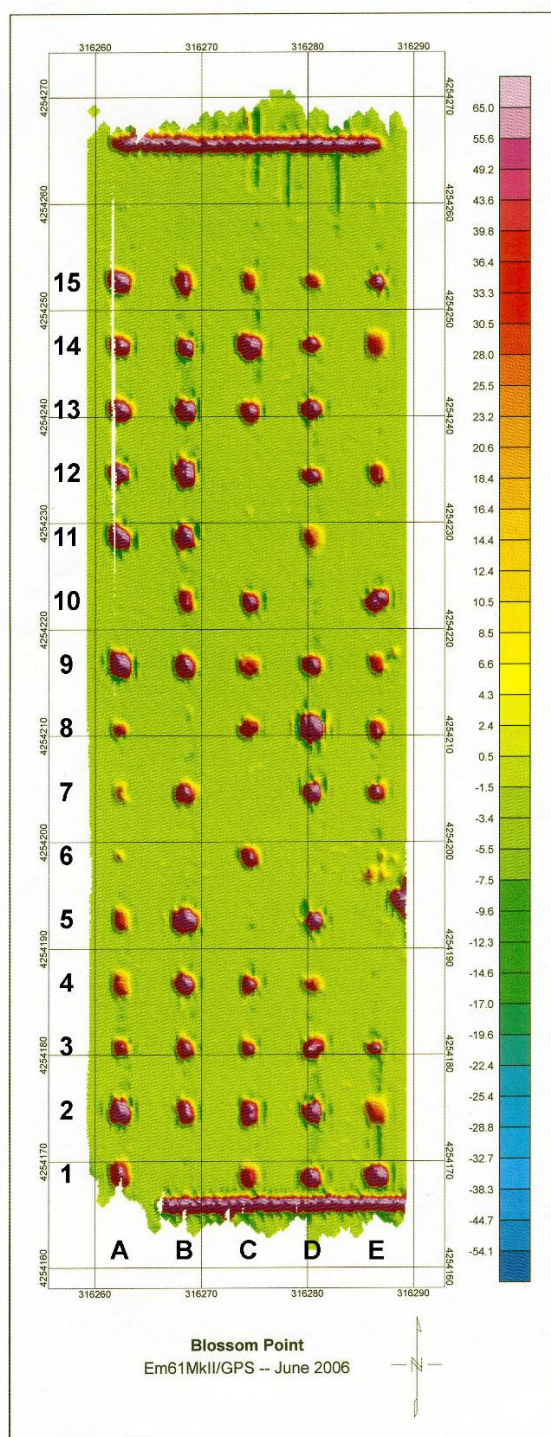
Figure 53.   EM61 survey map of the Blossom Point test site showing target grid identification system.

of the 61 targets buried can be seen. The lines at either end of the site are pipes used provide a signal for temporally aligning the data. The 5x15 position grid system is shown on the plot, with grid point locations identified by a letter (A through E) denoting East-West position and a number (1 through 15) denoting North-South locations. The surveys were conducted along North-South lines. The nominal line spacing was 0.5 m. The data have been analyzed using the standard dipole response model (Bell et al, 2001). To a very good approximation, the target response can be represented in terms of the magnetic polarizability along each of its principal axes.

A magnetic polarizability matrix **B** describes the induced dipole response of the target. The EM61 approximates an ideal time-domain sensor (current maintained at a constant level I_0 and then instantaneously returned to zero), for which the EMI signal S is represented in terms of **B** as

$$S(t) = \mu_0 A I_0 C_R \cdot C_T \mathbf{B}(t). \tag{1}$$

The signal is recorded over four time gates following the primary field cutoff, centered at 0.1, 0.37, 0.66 and 1.27 msec. We use only data from the first time gate, corresponding to the strongest signals, in the analysis reported here. In equation (1), C_T and C_R are coil sensitivity functions for the transmit and receive coil, μ_0 is the magnetic permeability of free space ($4\pi \times 10^{-7}$ volt-sec/amp-m), and A is a scaling factor that depends on the number of turns in the transmit and receive coils, the receiver gain, etc. C_T and C_R depend only on coil geometry and location relative to the target, while **B** depends only on what the target is, not where it is. The coil sensitivity functions are vectors that specify (a) the strength and orientation of the primary field at the target (C_T) and (b) the sensitivity of the receive coil to the vector components of a magnetic dipole source at the target location (C_R). The vector $C_T\mathbf{B}$ describes the strength of the induced target response in the X, Y and Z coordinate directions. Taking the dot product with C_R accounts for the relative sensitivity of the receive coil to each of these response components.

The strength and orientation of C_T and C_R are sensitive functions of the location of the EMI sensor relative to the target. C_T and C_R are defined in terms of integrals around the coil involving the vector from the target to the coil:

$$C_{T,R}(\mathbf{r}_0) = \frac{1}{4\pi} \oint_{T,R} \frac{d\mathbf{l} \times (\mathbf{r}_0 - \mathbf{r})}{|\mathbf{r}_0 - \mathbf{r}|^3} \tag{2}$$

where $\mathbf{r}_0$ is the location of the target and $\mathbf{r}$ is the location of a point on the coil.

As a consequence of EM reciprocity, the matrix **B** is symmetric. By a suitable rotation it can be transformed to diagonal form, so we can write

$$\mathbf{B} = \mathbf{U}\mathbf{B_0}\mathbf{U}^{\mathsf{T}} \tag{3}$$

with

$$\mathbf{B_0} = \begin{bmatrix} \beta_1 & 0 & 0 \\ 0 & \beta_2 & 0 \\ 0 & 0 & \beta_3 \end{bmatrix}. \tag{4}$$

In terms of yaw, pitch, and roll Euler angles θ, ϕ, and ψ, the rotation matrix **U** is given by

$$\mathbf{U} = \begin{bmatrix} \cos\theta\cos\phi & \cos\theta\sin\phi & -\sin\theta \\ \sin\psi\sin\theta\cos\phi - \cos\psi\sin\phi & \sin\psi\sin\theta\sin\phi + \cos\psi\cos\phi & \cos\theta\sin\psi \\ \cos\psi\sin\theta\cos\phi + \sin\psi\sin\phi & \cos\psi\sin\theta\sin\phi - \sin\psi\cos\phi & \cos\theta\cos\psi \end{bmatrix}. \tag{5}$$

The eigenvalues β_1, β_2, and β_3 correspond to responses induced by field components aligned with each of the target object's principal axes. θ, ϕ, and ψ together define the orientations of these principal axes. In general, the aggregate magnitude of the βs is determined by the size of the object, while differences among the βs are related to the object's shape.

Determining the βs from EMI data collected over a buried object is fairly straightforward. As the sensor moves over a target, the object is excited from different directions, while the sensitivity of the receiver to the different response components also varies – data from different locations above the target combine the elements of the polarizability matrix **B** in different ways. As it turns out, if enough data are collected over an area whose dimensions are somewhat larger than the depth of the object, then all of the elements in **B** contribute enough, and in enough different ways to the overall response that the data can be inverted to determine the βs.

With data collected at N locations ($\mathbf{r}_i$, i=1,2,…,N) over an unknown object, we have an over-determined set of N simultaneous equations with nine unknown quantities (three βs, three Euler angles that define the object's orientation, and the xyz coordinates of the unknown target location $\mathbf{r}_0$):

$$S_i = \mu_0 A I_0 C_R(\mathbf{r}_0 - \mathbf{r}_i) \cdot C_T(\mathbf{r}_0 - \mathbf{r}_i)\mathbf{U}\mathbf{B_0}\mathbf{U}^\mathsf{T}, \qquad i=1,2,\dots,N. \tag{6}$$

We solve these equations in a least-squares sense using a set of processing procedures originally developed for the NRL's MTADS system under ESTCP project MM-9526.

5.3.3. Inversion Error Sources

The Blossom Point tests were intended to demonstrate how improving sensor positioning and orientation can improve the fidelity of target parameters estimated by inverting EM61 data collected in field surveys. If the locations $\mathbf{r}_i$ of the sensor readings S_i used to estimate the target parameters are in error, then the model (1) cannot rightly reproduce the data. And to the extent that it actually does, it will do so using target parameters that are incorrect. We can use the dipole fit error to evaluate performance. The fit error is calculated from the squared correlation coefficient (R^2) between the best model fit and the data. Statistically speaking, the quantity $1-R^2$ is the portion of the signal variance that is not accounted for by the model, so we define the dipole fit error as

$$\varepsilon = \sqrt{1 - R^2} \; . \tag{7}$$

The major factors limiting performance in the field are positioning errors and background noise. Both of these factors affect the inversion process. Since the simultaneous equations (6) are linear in the polarizability elements, errors in estimates of the polarizability matrix will be proportional to the errors in the S_i, (and hence ε) with the constant of proportionality determined by details of the coil sensitivity functions $\mathbf{C}_R$ and $\mathbf{C}_T$. Figure 54 shows the relationship between errors in target parameter estimates (βs) and the dipole fit error based on Monte-Carlo simulations (Bell, 2005). The beta error is defined as

$$\beta_{ERR} = \sqrt{\frac{1}{3}\sum_{i=1}^{3}\left(\frac{\beta_i - \beta_{0,i}}{\beta_{0,i}}\right)^2} \tag{8}$$

where the β_i are βs calculated using noisy data and $\beta_{0,i}$ are the true βs. In order to get target parameters with sufficient accuracy ($< 30\text{-}50\%$) to support target classification, we need dipole fit errors of 5% or less.
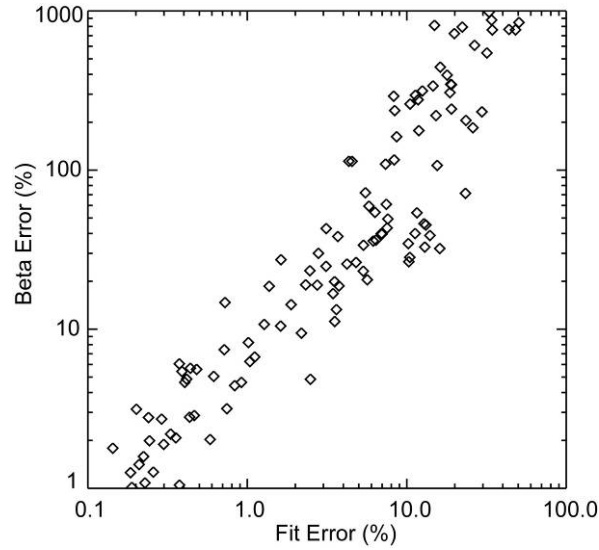
Figure 54.   Beta error vs. Dipole Fit Error from Monte Carlo simulations.

In what follows, we use the dipole fit error expressed as a percentage of the net signal strength as a figure of merit for comparing performance among different collection modes. The fit error depends on target Signal to Noise Ratio (SNR) and geolocation error. SNR (in dB) is defined as

$$\text{SNR} = 10\log\left(\frac{\frac{1}{2}S_{\text{max}}^2}{\text{var}(N)}\right). \tag{9}$$

where S_{max} is the maximum signal and var(N) is the background noise variance. For the Blossom Point surveys, the noise variance averaged about ($\sim$1.5 mV^2). Since 1-R^2 is the portion of the signal variance that is not accounted for by the model, in the absence of geolocation errors SNR and fit quality are related by

$$\text{SNR} = -20\log(\varepsilon) + 10\log\left(\frac{\frac{1}{2}S_{\text{max}}^2}{\frac{1}{N}\Sigma S_i^2 - \left(\frac{1}{N}\Sigma S_i\right)^2}\right). \tag{10}$$

The second factor in equation on the right hand side of (10) accounts for the fact in equation (9) we define SNR in terms of S_{max}, whereas the correlation coefficient is based on the variations about the mean signal level. Empirically, for the Blossom Point data this factor amounts to about 8.9dB.

Uncorrected sensor position (geolocation) errors represent an additional contribution to the noise, so the effective signal to noise ratio is less than the actual SNR from equation (9). This additional noise can be expressed in terms of the position uncertainty δl and the spatial gradient of the signal ∇S as

$$N_{\delta l}^2 = \overline{(\nabla S)^2 \delta \ell^2} \ . \tag{11}$$

∇S depends on target depth and varies over the anomaly. We calculate a nominal RMS value for ∇S using the forward model for EM61 signals as follows. For simplicity we assume a spherical target (equal βs). For each target depth at the test site, calculate the mean value of $(\nabla S)^2$ over that part of the anomaly where $S > 0.05\ S_{max}$, then average over the target depths. The nominal value of $\sqrt{(\nabla S)^2}$ calculated in this way is about 0.8% of S_{max} per cm of position error. Over the range of target depths, the spread is 0.4% to 1.1% of S_{max} per cm of position error.

5.3.4. Comparative Performance of Survey Modes

The performance of the various survey modes is summarized in Figure 55. The results are presented as plots of the dipole fit error (7) as a function of signal to noise ratio (9) for the fitted targets for each survey mode. The solid line in each plot shows the expected dependence of dipole fit error on SNR with perfect geo-location of the data. It is calculated from equation (10) using the correction factor of 8.9dB determined from the average anomaly shape. The dashed lines show the expected behavior with various levels of geolocation error, calculated by including the effective noise factor (11) using the nominal value $\sqrt{(\nabla S)^2} \sim 0.8\%$ of S_{max} per cm of position error. There is considerable scatter in the data, but generally speaking the residual geolocation error appears to be smaller when the gimbals are free than when they are fixed, and smaller with ArcSecond positioning than with GPS positioning.

On average the RMS pitch and roll of the system with the gimbals fixed were found to be 2.62° and 1.68° respectively. The corresponding values dropped to 1.32° and 0.95° respectively when the gimbals were free. With the GPS antenna 1 m above the coil, sway due to this pitching and rolling motion will produce RMS position errors of 4.6 cm and 2.9 cm, respectively, when the gimbals are fixed. With the gimbals free, the corresponding values are 2.3 cm and 1.7 cm. The dipole fit results shown in Figures 55a and 55b seem consistent with the expected GPS geolocation errors. The best fit (least absolute deviation) to the gimbals fixed GPS data occurs for $\delta l \sim 3.4$ cm. With the gimbals free, the fit errors are reduced, and the corresponding best fit value the geolocation error δl is 2.6 cm. Given the scatter in calculated $\sqrt{(\nabla S)^2}$ values, the agreement seems not unreasonable. The gimbaled configuration was also run over ramps set

up at a small number of targets to simulate a more inhospitable environment. The results for GPS and ArcSecond positioning as the system was pushed over the ramps were comparable to the corresponding results without the ramps.

With ArcSecond positioning, the geolocation error should be nil, yet the data in Figures 55c and 55ddo not follow the solid curves. An additional source of error in dipole inversion of survey data arises due to the temporal response characteristics of the EM61. When theEM61 coil is swept over a small spherical object, it is noted that the peak response is delayed relative to the time of closest approach to the object, and is somewhat distorted. These effects are due to the averaging circuitry in the EM61. In our standard EM61 processing, we use a static forward model and account for the delay by aligning successive back and forth survey passes over a wire or pipe. This ignores the slight signal distortion due to the dynamic response of the instrument. This residual effect is usually overwhelmed by the effects of the geolocation errors that arise with standard EM61 surveys, but can become the limiting factor for high signal to noise targets with sub-cm scale geolocation accuracy.
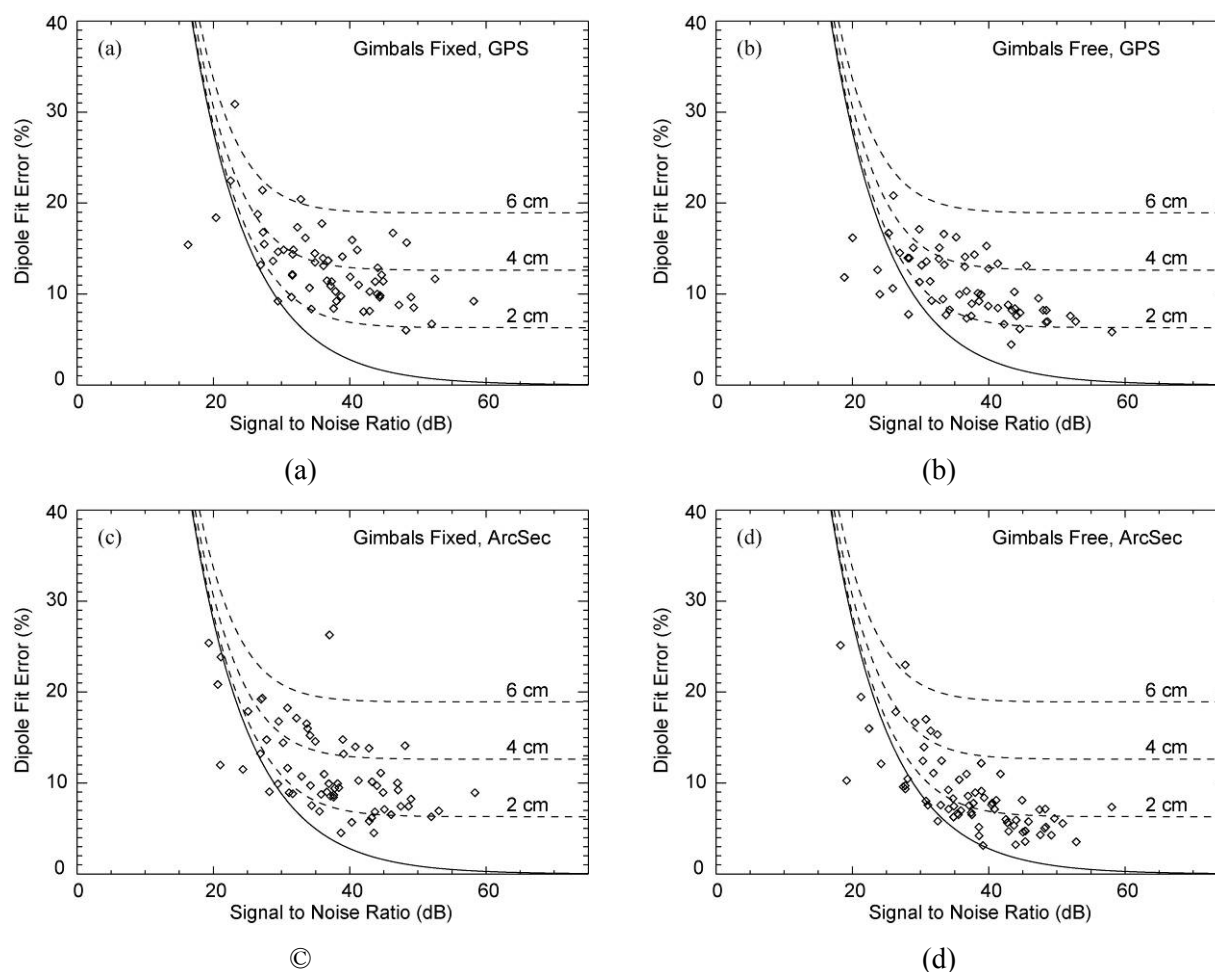
Figure 55.   Dipole fit error *vs.* target SNR for survey modes with (a) gimbals fixed and GPS positioning, (b) gimbals free and GPS positioning, (c) gimbals fixed and ArcSecond positioning, and (d) gimbals free and ArcSecond positioning. Solid line shows expected behavior with perfect geolocation, dashed lines show expected behavior with various levels of geolocation error.

5.3.5.   **Comparative Performance of Survey Modes**

Depth estimates from the dipole fits are compared with actual target depths for each of the survey modes in Figure 56. Although there is a bit less scatter for the ArcSecond surveys than the GPS surveys, there is really very little difference in the accuracy of the depth estimates for the various survey modes. The statistics are summarized in Table 2. On average, estimated depths are within a couple of centimeters of the actual target depths, but the RMS error is ~25 cm, which amounts to just over 1/3 of the average target/coil separation (67 cm). For these data, fit quality does not seem to have much of an effect on the fit depth errors. The mean and RMS depth error for all of the survey data are plotted as functions of dipole fit quality (squared correlation coefficient between data and dipole model fit, R^2) in Figure 57. For

each plotted value of R^2, the mean and RMS error are calculated over the band $R^2 \pm 0.0015$, which typically includes about 20 samples. The depth estimates are not very accurate even for the relatively high quality fits ($R^2 > 0.9975$ corresponds to dipole fit error < 5%). We suspect that the data density may not be adequate to support reliable inversion for many of the targets, even if the fit quality is high. In such case the dipole model can reproduce the data, but there is not enough data to constrain the fit to the correct target parameters. We will return to this point when we discuss the fits obtained using the dynamic response model later in the next section.
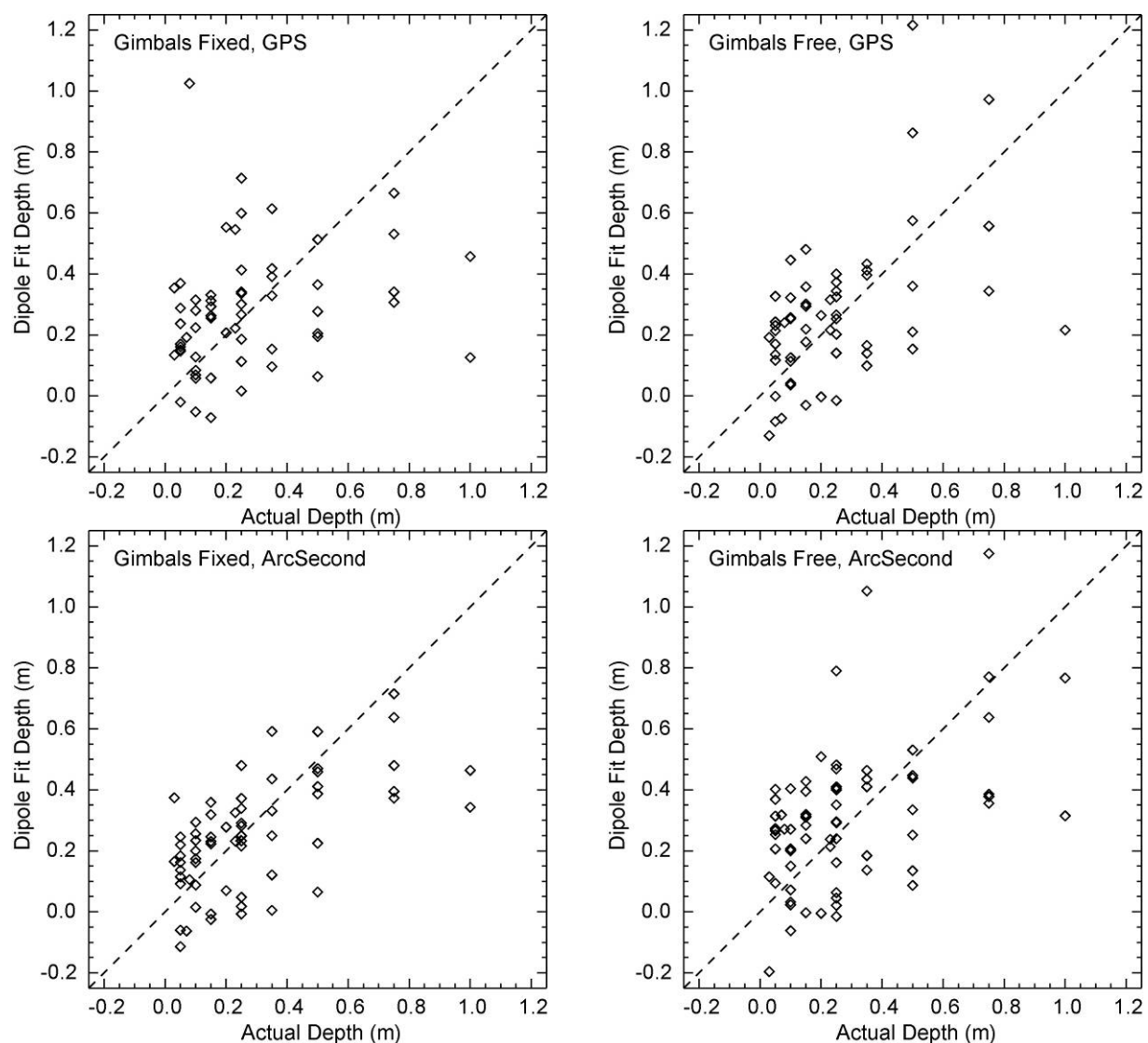
Figure 56.   Dipole fit depths compared to ground truth.

Table 2.   Summary statistics for dipole fit depth errors.

Survey Mode	Mean Depth Error (cm)	Std Dev (cm)
Gimbals Fixed, GPS	1.4	27.1
Gimbals Free, GPS	5.1	28.2
Gimbals Fixed, ArcSecond	-3.1	19.5
Gimbals Free, ArcSecond	2.9	23.9
All Data	1.6	24.8
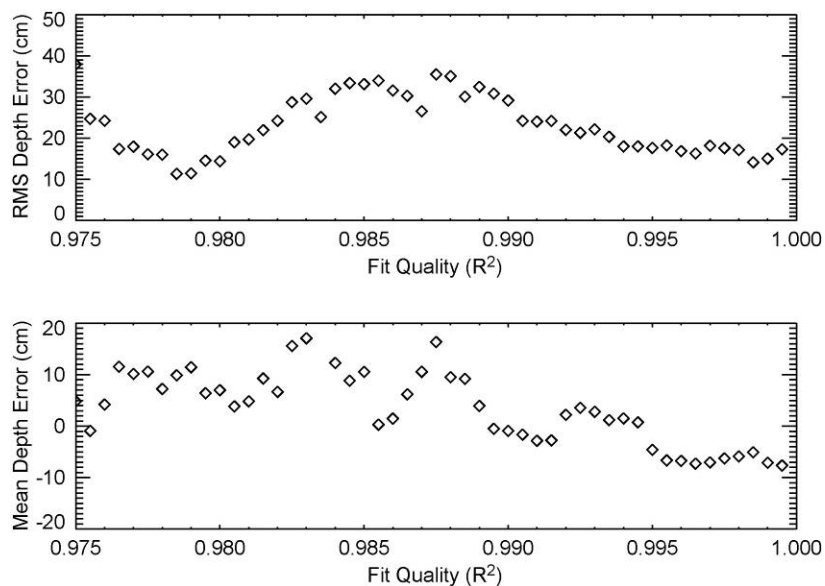
Figure 57.   Depth error *vs.* dipole fit quality.

Size estimates from these data are surprisingly robust. Roughly speaking, the trace of the polarizability tensor (sum of betas) should scale with the volume of the target. Since we are dealing with a single time gate, the proportionality is be exact because the shape of the decay curves varies with target size (Bell et al, 2001) (Bell et al., 2001). Figure 58 is a plot of $(\Sigma\beta)^{1/3}$ *vs.* target diameter for the UXO and UXO-like targets at the site (4:1 aspect ratio steel cylinders, Mk 23 practice bombs, 81 mm mortars, and BDU-33 practice bombs). All of the survey data are included. The +'s represent individual dipole fits, while the symbols listed in the key correspond to median values for each target type. The RMS spread in the values of $(\Sigma\beta)^{1/3}$ does not vary much among the targets, ranging from 22.6% to 28.9%. There appears to be a slight downward trend with size relative to a simple linear relationship as shown by the dashed line fit through the median values, consistent with a slight variation in the shape of the decay curve with size.
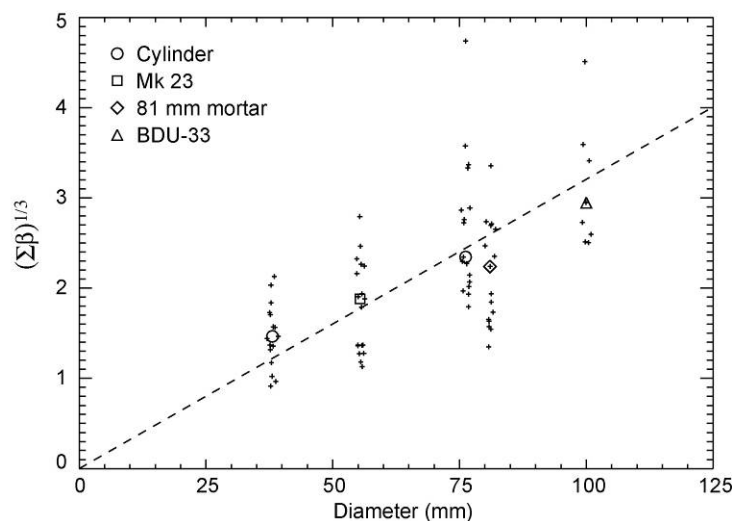
Figure 58.   Dependence of $(\Sigma\beta)^{1/3}$ on target size for UXO and 4:1 aspect ratio cylinders,

Target shape classification based on the dipole fits is an entirely different matter. The relationship among the betas is determined by the shape of the target. We normally order the betas from largest to smallest. Only fits with all three βs > 0 are physically realistic. Spherical targets should have all three betas equal, cylinders $\beta_1 > \beta_2 = \beta_3$, discs $\beta_1 = \beta_2 > \beta_3$ and irregularly shaped objects $\beta_1 > \beta_2 > \beta_3$ (Bell et al., in press). Figure 59 shows scatter plots of the beta ratios β_1/β_2 and β_2/β_3 for each of the survey modes. Different types of targets are identified by different symbols. Only 73% of the dipole fits actually had all three βs > 0. For those that did, there is no clear clustering of different types of targets in different regions of β_1/β_2 *vs.* β_2/β_3 space. We can only conclude that the quality of the dipole fits for these data is inadequate to support reliable target shape classification and discrimination.

Figure 59. Scatter plots of the beta ratios β_1/β_2 and β_2/β_3 for each of the survey modes.

Table 3.   Ground truth and estimated target parameters from dynamic model inversions.

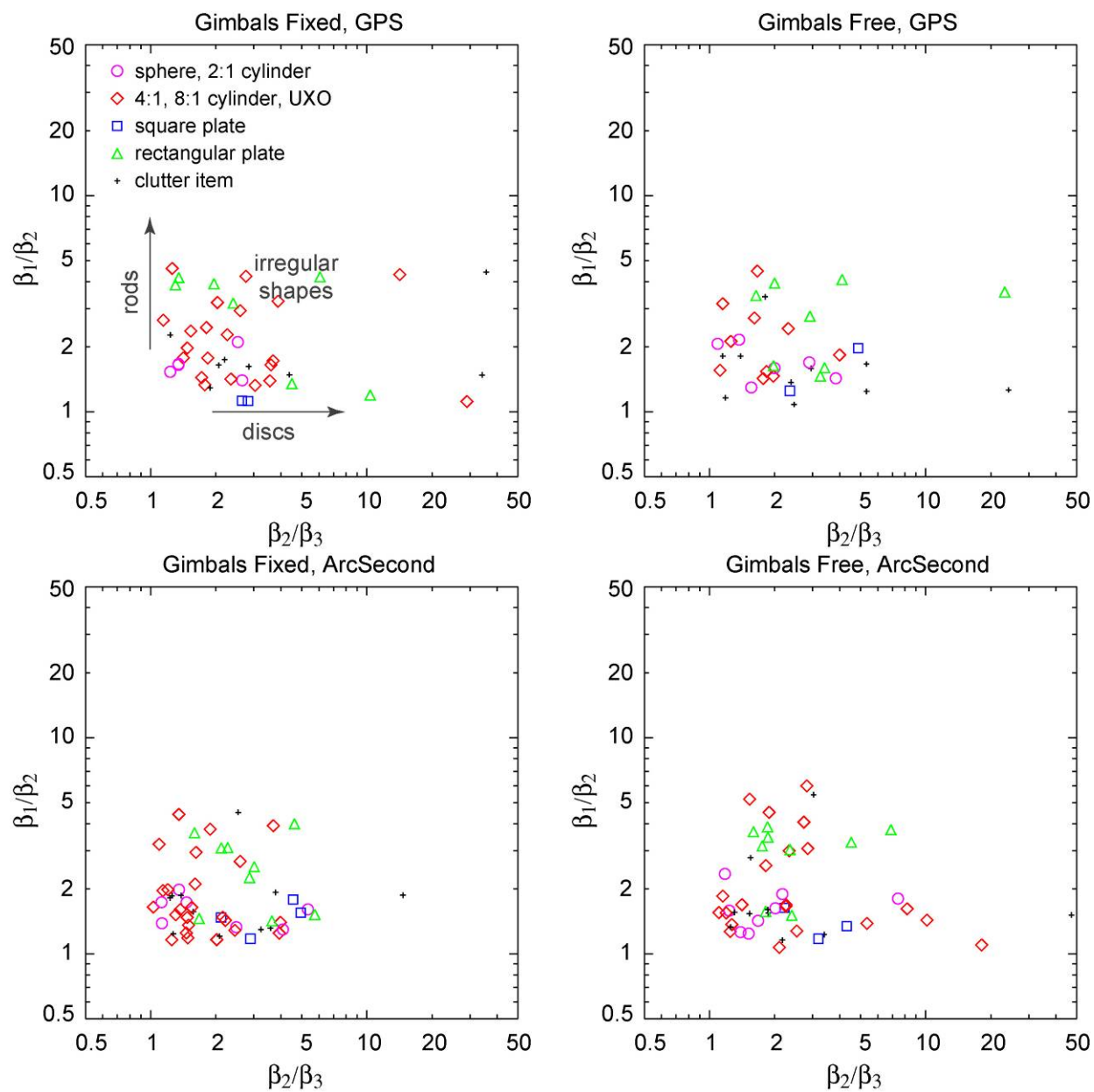| Target	Object	Depth (m)	Dip Angle (deg)	SNR (dB)	Fit Error (%)	Fit Depth (m)	Beta1	Beta2	Beta3
1	3x24 cyl	0.75	0	26.9	14.9	1.125	50.96	42.85	-13.74
2	1.5x3 cyl	0.05	0	28.3	9.5	0.000	0.405	0.100	0.087
3	1.5x6 cyl	0.20	0	30.1	9.9	0.300	3.308	0.964	-0.465
4	3x12 plate	0.25	0	32.9	4.6	0.250	5.414	1.803	0.562
5	4x4 plate	0.05	0	34.7	5.7	0.025	1.241	0.866	0.210
6	1.5x12 cyl	0.35	90	36.9	4.5	0.050	0.899	0.583	-0.112
7	8x8 plate	0.25	0	41.0	5.1	0.275	12.40	9.88	3.25
8	1.5x6 plate	0.08	90	41.3	4.7	0.075	1.862	0.170	-0.162
9	Shotput	0.25	0	43.4	2.9	0.175	3.610	2.925	2.445
10	Mk23	0.25	90	45.3	2.2	0.075	4.593	0.710	-0.131

Table 3 summarizes the ground truth information and target parameters from the dipole model fits using the dynamic response model. With the exception of targets 1, 6 and 10, the dipole fit depths are within 10 cm of the actual target depth. Target 1 has a relatively low SNR and the largest dipole fit error. Targets 6 and 10 are oriented vertically. Our experience has been that data collected over vertical targets are usually the hardest to invert, requiring a relatively high data density above the target as well has high SNR and accurate positioning. Indeed, all of the vertical targets have $\beta_3 < 0$, and we suspect that this aphysical result is due to inadequate data density over the targets. A map of the data for target 10 is shown in Figure 60a. Each colored dot represents one sensor reading. Colors range from blue through light blue, green, yellow, and orange to red, corresponding to signal levels ranging from the background level to the maximum signal over the target. The target location is indicated by the diamond and cross symbol, and the ½ m by 1 m rectangle shows the location of the EM61 coil at its point of closest approach to the target. Significant signal levels are seen on only two of the survey lines over this target – the data density is simply not adequate to support reliable inversion. The dipole model can reproduce the data, but there are not enough data to constrain the fit to the correct target parameters. The data map for target 7 is shown in Figure 60b. This is a flat steel plate at the same depth as target 10, which is a vertical Mk 23. At 8.25" long by 2.18" in diameter, the Mk 23 is more or less the same size as the steel plate. Signal from the plate shows up on four of the survey lines, and the dipole inversion appears to yield accurate values for the target parameters. The dipole depth is correct to 2.5 cm and the beta ratios ($\beta_1/\beta_2 = 1.26$, $\beta_2/\beta_3 = 3.04$) are as expected for a square plate. Like target 10, target 6 has appreciable signal on only two survey lines. Target 8 has signal on three lines and gets a better depth estimate, but the data density is still not good enough to get betas that are good enough for shape classification. The other high SNR targets (4, 5, 9) seem to have dipole fits that are good enough to support shape classification. The βs should be equal

for the shotput (target 9), and the values from the dipole model fit are within 20% of each other. Referring back to Figure 55, this is the sort of accuracy we would expect with a dipole model fit error of about 3%. Similarly, target 5 comes out looking like a square plate (two large, equal and one small beta), while the βs for target 4 (rectangular plate) are consistent with a target with three distinct length scales.
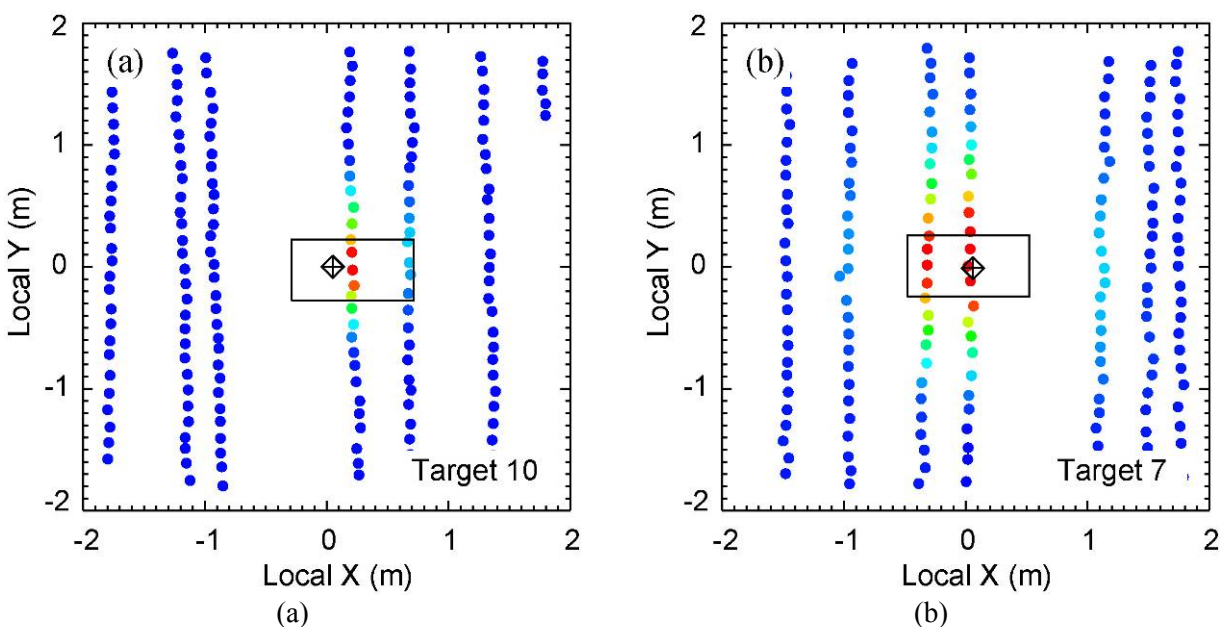
Figure 60.   Data maps for (a) target 10 and (b) target 7.

5.3.6.   Blossom Point Summary

The Blossom Point tests were intended to demonstrate how improving sensor positioning and orientation can improve the fidelity of target parameters estimated by inverting EM61 data collected in field surveys. Four survey modes were employed in collecting data at the site: (a) gimbals fixed with DGPS/RTK positioning ("Standard" survey), (b) gimbals free with DGPS/RTK positioning, (c) gimbals fixed with ArcSecond positioning, and (d) gimbals free with ArcSecond positioning. With the gimbals fixed, the cart behaves more or less like a standard EM61 survey.

We found that the dipole fit quality is generally better when the gimbals are operating freely than when they are locked, and is generally better with ArcSecond positioning than with GPS positioning. Apparent residual geolocation errors with GPS positioning are consistent with uncompensated antenna sway caused by the pitching and rolling of the system. Fit errors are not reduced to the theoretical SNR limit with standard processing of the ArcSecond survey data. A small number of the gimbaled ArcSecond targets were re-processed using a dynamic response model that accounts for signal distortion introduced by the

EM61 receiver circuitry. Dipole fit quality using dynamic model inversion was found to agree with the theoretical SNR limit.

Target depth estimates for the four survey data sets were not very accurate. Although on average estimated depths were within a few centimeters of actual target depths, the scatter in the estimated depths (RMS depth error) amounted to about 1/3 of the average target/coil separation. The scatter was slightly less for the ArcSecond fits (21.7 cm) than for the GPS fits (27.7 cm). Even for relatively high quality fits the depth estimates were not very accurate, and we suspect that the data density may not have been adequate to support reliable inversion for many of the targets. Given the lackluster performance for target depth estimates, target size estimates were surprisingly robust. On average, the size metric $(\Sigma\beta)^{1/3}$ was found to vary in direct proportion with the size of UXO and UXO-like targets. The scatter in the estimates amounted to about 25% of the mean values. As with depth estimates, substantial differences in the accuracy of the size estimates for the various survey modes were not observed.

Target shape classification based on the dipole fits using standard processing was a failure. One should be able to determine whether a target is rod-like (UXO-like), disc-like, or irregularly shaped from the ratios β_1/β_2 and β_2/β_3. However, we found no clear clustering of different target types in different regions of β_1/β_2 *vs.* β_2/β_3 space for any of the surveys with standard processing. However, the results for dynamic model inversions were encouraging – we seem to get reasonable shape estimates for those targets where SNR and data density do not appear to be limiting performance. Our analysis of the results suggests that a higher data density (closer survey line spacing) than that used here would be required to secure significant performance improvements.

6. MODELING THE EFFECTS OF SENSOR ORIENTATION

Sensor orientation information is utilized during the forward and inverse modeling process to account for signature variations caused by non-horizontal sensor orientation during data collection. As part of this project, the EM modeling process for sensor orientation information was developed that included full simulation of 3D orientation of EMI sensors; multi-time gate EMI response; and a beta classification technique.

6.1. EMI Dipole Response Model

Because EMI sensors can excite an object from different directions, they can be used to obtain information relating to the shape of the object as well as its size and composition (electrical conductivity and magnetic permeability). These intrinsic properties of the target can be used with statistical decision rules to discriminate between UXO and clutter. Target shape is especially significant because most UXO are long and slender, having been designed to be shot from guns or dropped from aircraft and to maintain a steady trajectory. Clutter items come in an endless variety of shapes.

The basic operation of the EM61 sensor is illustrated schematically in Figure 61. The sensor consists of a transmit coil and a pair receive coils, one co-located with the transmit coil and one offset vertically 40 cm above the transmit coil. The coils are rectangular, 0.5 m long, and 1 m wide. Current flowing in the transmit coil produces the primary field $\mathbf{H}_0$ shown by the solid lines. Changes in the primary field $\mathbf{H}_0$ induce eddy currents in the target, which in turn produce the induced field $\mathbf{H}_I$ shown by the dashed lines. The signal S(t) is proportional to the receiver voltage V(t) created by a changing magnetic flux through the receive coil due to $\mathbf{H}_I$. The target response to the primary field can be represented in terms of an induced dipole moment that depends on the strength and orientation of the primary field at the target and on the size, shape, composition, and orientation of the target.
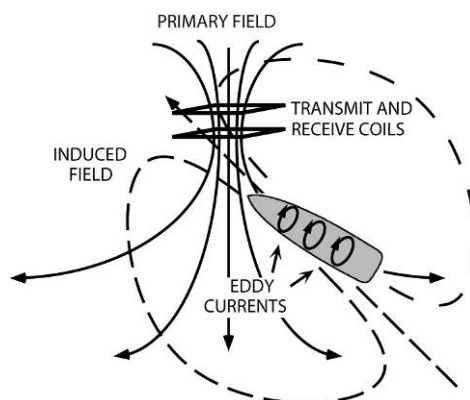
Figure 61.   Basic elements of the EM61 sensor.

To a very good approximation, the target response can be represented in terms of the magnetic polarizability along each of its principal axes. A magnetic polarizability matrix **B** describes the induced dipole response of the target. The EM61 approximates an ideal time-domain sensor (current maintained at a constant level I_0 and then instantaneously returned to zero), for which the EMI signal S is represented in terms of **B** as

$$S(t) = \mu_0 A I_0 C_R \cdot C_T \mathbf{B}(t).$$ (12)

The signal is recorded during over time gates following the primary field cutoff, centered at 0.1, 0.37, 0.66 and 1.27 msec. In Equation 12, $\mathbf{C}_T$ and $\mathbf{C}_R$ are coil sensitivity functions for the transmit and receive coil, μ_0 is the magnetic permeability of free space ($4\pi \times 10^{-7}$ volt-sec/amp-m) and A is a scaling factor that depends on the number of turns in the transmit and receive coils, the receiver gain, etc. $\mathbf{C}_T$ and $\mathbf{C}_R$ depend only on coil geometry and location relative to the target, while **B** depends only on what the target is, not where it is. The coil sensitivity functions are vectors that specify (a) the strength and orientation of the primary field at the target ($\mathbf{C}_T$) and (b) the sensitivity of the receive coil to the vector components of a magnetic dipole source at the target location ($\mathbf{C}_R$). The vector $\mathbf{C}_T\mathbf{B}$ describes the strength of the induced target response in the X, Y, and Z coordinate directions. Taking the dot product with $\mathbf{C}_R$ accounts for the relative sensitivity of the receive coil to each of these response components.

The strength and orientation of $\mathbf{C}_T$ and $\mathbf{C}_R$ are sensitive functions of the location of the EMI sensor relative to the target. $\mathbf{C}_T$ and $\mathbf{C}_R$ are defined in terms of integrals around the coil involving the vector from the target to the coil:

$$C_{T,R}(r_0) = \frac{1}{4\pi} \oint_{T,R} \frac{dl \times (r_0 - r)}{|r_0 - r|^3} \tag{13}$$

where $\mathbf{r}_0$ is the location of the target and $\mathbf{r}$ is the location of a point on the coil.

As a consequence of EM reciprocity, the matrix $\mathbf{B}$ is symmetric. By a suitable rotation it can be transformed to diagonal form, so we can write

$$\mathbf{B} = \mathbf{U}\mathbf{B_0}\mathbf{U}^\mathsf{T} \tag{14}$$

with

$$\mathbf{B_0} = \begin{bmatrix} \beta_1 & 0 & 0 \\ 0 & \beta_2 & 0 \\ 0 & 0 & \beta_3 \end{bmatrix}. \tag{15}$$

In terms of yaw, pitch, and roll Euler angles θ, ϕ, and ψ, the rotation matrix $\mathbf{U}$ is given by

$$\mathbf{U} = \begin{bmatrix} \cos\theta\cos\phi & \cos\theta\sin\phi & -\sin\theta \\ \sin\psi\sin\theta\cos\phi - \cos\psi\sin\phi & \sin\psi\sin\theta\sin\phi + \cos\psi\cos\phi & \cos\theta\sin\psi \\ \cos\psi\sin\theta\cos\phi + \sin\psi\sin\phi & \cos\psi\sin\theta\sin\phi - \sin\psi\cos\phi & \cos\theta\cos\psi \end{bmatrix}. \tag{16}$$

The eigenvalues β_1, β_2, and β_3 correspond to responses induced by field components aligned with each of the target object's principal axes. θ, ϕ, and ψ together define the orientations of these principal axes. In general, the aggregate magnitude of the βs is determined by the size of the object, while differences among the βs are related to the object's shape. Target classification and discrimination exploit both these dependencies. Many different objects can have more or less the same response, depending on their orientation and location relative to the sensor. However, they will not respond the same for all orientations. The interrelationship of the βs is what distinguishes different objects of more or less the same size.

6.2. Inversion of Survey Data Using the Dipole Response Model

Determining the βs from EMI data collected over a buried object is fairly straightforward. As the sensor is moved around, the object is excited from different directions, while the sensitivity of the receiver to the different response components also varies – data from different locations above the target combine the elements of the polarizability matrix B in different ways. As it turns out, if data are collected over an area whose dimensions are somewhat larger than the depth of the object, then all of the elements in B contribute enough, and in enough different ways to the overall response that the data may be inverted to determine the βs.

If data are collected at N locations (ri, i=1,2,…,N) over an unknown object, then we have an over-determined set of N simultaneous equations with nine unknown quantities (three βs, three Euler angles that define the object's orientation, and the xyz coordinates of the unknown target location r0):

$$S_i = \mu_0 A I_0 C_R (r_0 - r_i) \cdot C_T (r_0 - r_i) \mathbf{U}\mathbf{B_0}\mathbf{U}^{\mathrm{T}}, \quad \mathrm{I} = 1,2,…,\mathrm{N}. \qquad (17)$$

We solve these equations in a least-squares sense using a set of processing procedures written in IDL (Research Systems Inc.). The core routines were originally developed with funding from the NRL under ESTCP project MM-9526. The current two-stage approach with monitoring of the fit trajectory was developed under ESTCP project MM-0108. The forward model was used in the inversion modified to account for sensor orientation for this project.

The least squares solution of Equation 17 is accomplished in a two-stage process. First, the target location was searched using a gradient-expansion algorithm to minimize the mean squared error (chi-square) between the dipole response model and the measured data. At each test location, the best fit **B** is calculated using a linear least squares fit, which simply involves solving a set of simultaneous linear equations for the six unique elements of **B**. Sensor orientation variations during data collection are accommodated by transforming the target location $\mathbf{r}_0$ and polarizability matrix $\mathbf{B} = \mathbf{U}\mathbf{B}_0\mathbf{U}^{\mathrm{T}}$ into appropriately aligned coordinates at each measurement point. (Sensor pitch and roll were measured and recorded, while yaw was estimated from the sensor track.) Second, the Biot-Savart integrals are calculated for the rectangular EM61 coils directly by combining algebraic expressions for each of the four line segments which make up the rectangle. In the analysis reported here attention was restricted to the first time gate and the lower receive coil, which produce the strongest signals.

When inverting EM61 data, the anomaly data to be processed is interactively selected. This is done by displaying a contour map of the data in the vicinity of a target and creating a polygon around the anomaly by clicking on cursor. The data within the polygon is extracted from the data file and sent to the inversion routines. Figure 62 shows the display with a selection polygon. The inversion processing is monitored by plotting various diagnostics as functions of the test depth. The monitoring display is shown in Figure 63. The target is an 81mm mortar at 0° dip angle, aligned 30° from the X axis. The depth from the ground surface to the top of the target is 28 cm. The plot in the upper left corner is a scatter plot of model fit vs. data. For a good quality fit the points cluster along the diagonal. The center plot on the top line shows chi-square vs. test depth. The minimum chi-square point represents the best fit. The upper right plot shows target dip and azimuth along the fit trajectory. The lower left plot compares contours of data (solid blue) and dipole model fit (dashed red). The center bottom plot shows the best fit betas as functions of test depth. Note that the two minor betas neck together near the minimum chi-square depth. This is characteristic of a UXO item for which we expect one larger β (long axis response) and two smaller, equal βs (transverse responses). The lower right plot shows β_1 vs. β_2 and β_3 along the fit trajectory. The center and right plots are color coded, green near the minimum chi-square through red as chi-square increases and the fit quality degrades.
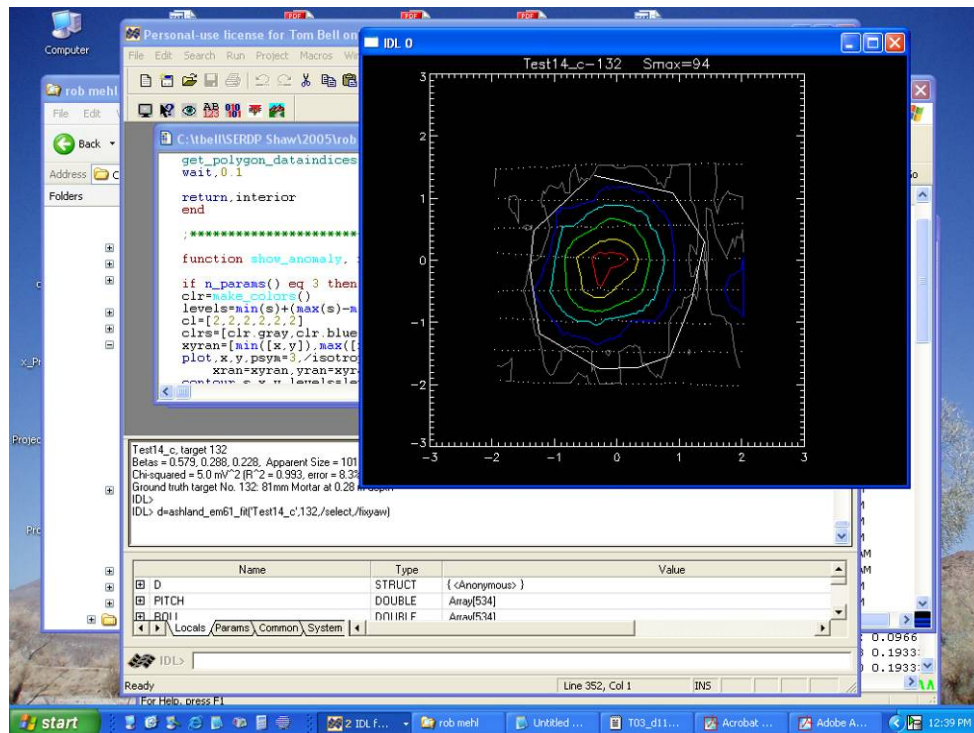

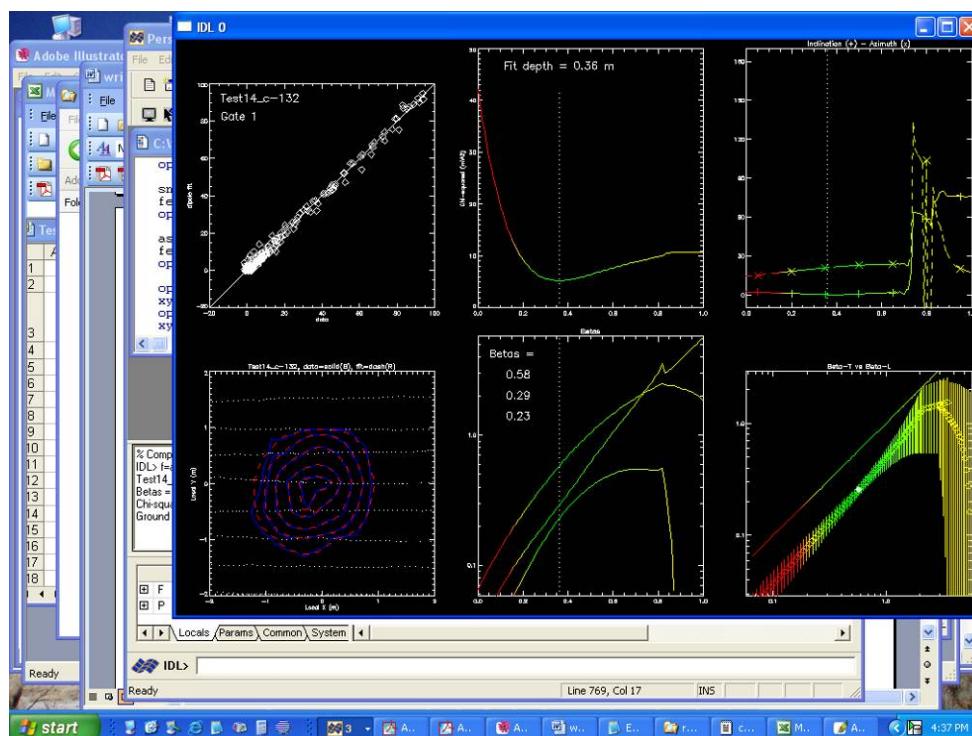Figure 62.   Anomaly selection example.

Figure 63.   Example of data inversion display.

6.3.   Modeling Conclusions

The EM data modeling techniques developed by this project are an important component for mitigating the effects of sensor orientation for advancing UXO discrimination capabilities. Sensor orientation information is utilized during the forward and inverse modeling process to account for signature variations caused by non-horizontal sensor orientation during data collection. The EM modeling process developed includes full simulation of 3D orientation of EMI sensors; multi-time gate EMI response; and a beta classification technique.

An EMI dipole response model was tested to facilitate modeling of EM data in conjunction with concurrently collection orientation information and incorporated into the beta inversion model used for target parameter estimation. Data analysis performed on Ashland Test plot data collected in 2005 showed inversions performed using gimbaled and corrected data produced significant improvements, in terms of reduced fit error, when compared to standard survey methods.

In 2006 testing, data analysis using the developed models again found that the dipole fit quality is generally better when the gimbals are operating freely than when they are locked, and is generally better with ArcSecond positioning than with GPS positioning. Fit errors were not reduced to the theoretical

SNR limit with standard processing of the ArcSecond survey data. A small number of the gimbaled ArcSecond targets were re-processed using a dynamic response model that accounts for signal distortion introduced by the EM61 receiver circuitry. Dipole fit quality using dynamic model inversion was found to agree with the theoretical SNR limit.

7.   REFERENCES

Asch, T. and E. Staes, "An Ordnance Detection and Discrimination Study at Former Fort Ord, CA," presented at the UXO / Countermine Forum, April 2001, New Orleans, LA.

Barrow, B.J., and Nelson, H., "Effect Of Positioning Measurements On Inverting Electromagnetic Induction Data From Unexploded Ordnance", UXO Forum, April 2001, New Orleans.

Bruce Barrow, Ngai Khadr and Thomas Bell, "Evaluation of Laser Based Positioning for Characterization of EMI Signals from UXO," Symposium on the Application of Geophysics to Environmental and Engineering Problems, Seattle, April 2006.

Thomas Bell, "Geo-location Requirements for UXO Discrimination," SERDP/ESTCP Geolocation Workshop, Annapolis, June 2005.

Thomas Bell, Bruce Barrow, Jonathan Miller and Dean Keiswetter, "Time and Frequency Domain Electromagnetic Induction Signatures of Unexploded Ordnance," Subsurface Sensing Technologies and Applications 2(3), July 2001, pp. 153-175.

Thomas H. Bell, Bruce J. Barrow and Jonathan T. Miller, "Subsurface Discrimination Using Electromagnetic Induction Sensors," IEEE Trans. Geoscience and Remote Sensing 39(6), June 2001, pp. 1286-1293.

Thomas H. Bell, Jonathan T. Miller, Bruce J. Barrow and Herbert H. Nelson, "Measured Dipole Response Characteristics of Compact Metal Objects," Chapter 8 in Identification of Mines and Unexploded Ordnance, C. E. Baum (Ed.), Harvard University Press, to appear.

Foley, J., "Sensor Orientation Effects on UXO Geophysical Target Discrimination," 2003 Annual Report to SERDP, December, 2003.

Foley, J., "Sensor Orientation Effects on UXO Geophysical Target Discrimination," 2004 Annual Report to SERDP, December, 2004.

Foley, J. "Sensor Orientation Effects on UXO Geophysical Target Discrimination," 2005 Annual Report to SERDP, January, 2006.

Mason, M., Blair, M, and C. Jozaitis, "Coordinate Accuracy and Precision of the USDADS Ultrasonic Method as Applied to Digital Geophysical Mapping", presented at the UXO / Countermine Forum, April 2001, New Orleans, LA.

Nelson, H.H., McDonald, J. R. and R. Robertson, "Design and construction of the NRL baseline ordnance classification test site at Blossom Point," Tech. Rep. NRL/MR/6110– –00-8437, Washington, DC, Mar. 2000.